

ABSTRACT

Robert C. Gilliam: Influence of Surface Heterogeneities on the Boundary Layer Structure and Diffusion of Pollutants. (Under the direction of Dr. Sethu Raman)

Boundary layer processes are the dominating factors in the diffusion and transport of pollutants. Air pollution dispersion is known to be controlled by several boundary layer factors. Eddy diffusion, described by the amount of turbulent kinetic energy, is the main influence on how quickly a parcel of polluted air expands and boundary layer depth determines the extent of vertical mixing potential.

This thesis explores the influence that mesoscale surface related features have on the boundary layer meteorology and air pollution dispersion through a combination of numerical model simulations and observations. Mesoscale processes including sea breeze and land breeze circulations, vegetation and soil type gradient induced circulations, urban heat island and terrain modified flows are addressed in this research through the use of various numerical simulations. Surface based observations from a meso-network and ground based remote sensing observations using two SODARs are examined. These observations are also utilized for model validation.

An observational analysis of 10 m micrometeorological tower measurements and collocated SODAR measurements is conducted for two different boundary layer events, which correspond to near neutral and convective conditions. SODAR data analysis of reflectivity and wind speed profiles is presented along with tower measurements of wind speed/direction (at 2 m, 5 m and 10 m levels) and the temperature difference between 10

m and 2 m. The analysis indicated dramatically different boundary layer structures during these events.

The near-neutral case shows that the boundary layer properties remained relatively constant during the 24-hour period, as indicated by the SODAR reflectivity that consisted of homogeneous echoes up to a height of about 100 m. The static stability, implied by the observed 10 m - 2 m temperature difference (ΔT_{10m-2m}), supports a neutral, well-mixed boundary layer. The wind speed profile indicated time dependent fluctuations in magnitude associated with shear induced boundary layer eddies..

The convective case shows a rapidly increasing boundary layer during the early morning, just after sunrise. Strong fluctuating periods of high reflectivity during the day allude to convective boundary layer thermals. At the same time, near surface temperature gradient (ΔT_{10m-2m}) shows strong buoyant instability. The overall convective pattern and associated boundary layer momentum is much different than that of the neutral case.

Numerical simulations, using the Advance Regional Prediction System (ARPS) includes an idealized tropical seabreeze simulation over India, a regional scale simulation over eastern North Carolina and a city scale simulation over Raleigh, North Carolina. Using both the seabreeze and city scale meteorological simulations, coupled ARPS-CALPUFF dispersion simulations are conducted to investigate the influence of the boundary layer meteorology on dispersion patterns.

The 5 km resolution seabreeze simulation shows that the boundary layer properties are distinctly different across a region that is affected by seabreeze circulations. The dispersion experiment from a point source near the coastline indicated that the seabreeze has a very noticeable effect on atmospheric dispersion overland.

Higher surface concentrations are modeled during the seabreeze episode and the post seabreeze period later in the evening..

The regional numerical simulation (6 km grid spacing) over eastern North Carolina combined several interesting boundary layer scenarios. The typically warmer Sandhills region and some of the larger urban centers are simulated as warmer surfaces. Turbulence is also higher over these warmer locations. Landuse is shown to have a definite impact on the degree of simulated turbulence as well as the boundary layer height.

The high-resolution atmospheric simulation conducted over Raleigh, North Carolina is for the same case presented by the regional simulation. The 1 km model forecast shows large distinctions within the microscale boundary layer structure over the city scale domain. The boundary layer variations are directly related to the landuse parameterization. During the night, the model is sensitive to terrain variations. Over the more elevated areas the wind speed was overall higher, while noticeably weaker over low-lying areas. A simulated down slope flow at night is detected and associated temperatures are less in the low-lying areas. The data from both SODARs compares well with the simulated profiles.

Dispersion patterns utilizing the high-resolution meteorology are influenced by the landuse in several respects. The 1 km ARPS simulation showed microscale convergence zones develop along strong surface temperature and sensible heat flux gradients, which are mostly a result of vegetation differences between the urban areas in/around Raleigh and surrounding rural areas. In the dispersion simulation, these convergence zones are directly related to higher surface concentrations.

The elevation is shown to influence the wind field at night, therefore modifying the concentrations field. More elevated areas, specifically the higher north-south ridge in the western part of the domain is associated with slightly stronger wind at night and therefore lower concentrations. The lower lying areas are more stable as a cooler slope flow is established at night. This drainage flow allows pollutants to collect over some of the highly populated suburbs around Raleigh.

**INFLUENCE OF SURFACE HETEROGENEITIES ON THE BOUNDARY LAYER
STRUCTURE AND DIFFUSION OF POLLUTANTS**

By
Robert C. Gilliam

A Masters thesis submitted to the Graduate Faculty of
North Carolina State University
In partial fulfillment of the
Requirements for the Degree of
Masters of Science

MARINE, EARTH AND ATMOSPHERIC SCIENCES
Raleigh
2001

Approved by:

Dr. S. Pal Arya

Dr. Devdutta S. Niyogi

Dr. Alan H. Huber

Dr. Sethu Raman, Chair

BIOGRAPHY

Robert C. Gilliam was born in Daytona Beach, Florida on May 25, 1972 to parents McLaurin Briggs II and Carol Jean Gilliam. He spent most of his young years growing up in and around McDowell County, North Carolina where he graduated in 1990 from McDowell High School. Robert spent his first few years of college attending Western Piedmont Community College in order to complete the required general education courses. His main ambition at the time was to acquire a degree in electrical engineering, so off he went to the University of North Carolina at Charlotte. In order to support him financially and to gain real world experience, he enrolled in the University Co-op program. For the next few years he worked every other semester with Bechtel Engineering Inc. at the Savannah River Site near Aiken, South Carolina. After this term, Robert decided that engineering was not his “cup of tea”. His ever-present interest in the atmosphere, which was mostly a product of his passion for surfing, lead him to the decision to transfer to North Carolina State University for a B.S. degree in Atmospheric Sciences. In the spring of 1999, Robert graduated with a B.S. degree in Meteorology from N.C. State with Magna Cum Laude recognition. This was not enough, more was to be learned, so Robert enrolled in the Graduate Program at N.C State the following fall semester for his M.S. degree in Atmospheric Sciences. His interest in mesoscale meteorological modeling grew and with support from the State Climate Office of North Carolina and United States Environmental Protection Agency, he finished his Masters Degree requirements in the Fall of 2001.

ACKNOWLEDGEMENTS

I would like to thank sincerely and recognize two main contributors for the completion of my Masters of Science Degree in Atmospheric Sciences. First I would like to thank Dr. Alan Huber and the Environmental Protection Agency for providing the financial means, computer resources and professional expertise. Secondly, I want to express appreciation to Dr. Sethu Raman, Dr. Dev Niyogi and the State Climate Office of North Carolina for their multi-faceted support, which is the main reason for the accomplishment of my M.S. Degree. On the same line, I would like to thank Ryan Boyles, the backbone of the State Climate Offices operation. I would also like to express thanks to Dr. S. Pal Arya for his approval of my research work and for accepting my request that he be on my committee.

Other mentions need to be made, especially the North Carolina Supercomputing Center, which has provided countless computer support and training. I need to recognize the Center for Analysis and Prediction of Storms (CAPS) for the years of work on the Advanced Regional Prediction System (ARPS). Also, Earthtech Inc. and Joe Scire's group for developing the CALPUFF modeling system. I would also like to say thank you to Brian Doty and his group for the best all around visualization software, GrADS.

On a personal level, I would like to express gratitude to my parents for the admirable structure in which I have been raised. Finally I want to thank my wife, Cecilia L. Gilliam, for her support both financially and spiritually; without this support a M.S. degree would have not been an option.

TABLE OF CONTENTS

LIST OF TABLES	vii
LIST OF FIGURES	ix
LIST OF SYMBOLS	xvii
1. INTRODUCTION	1
1.1 ATMOSPHERIC BOUNDARY LAYER AND AIR POLLUTION DISPERSION.....	1
1.2 RESEARCH OVERVIEW AND OBJECTIVES.....	5
1.3 WHY COUPLE ARPS AND CALPUFF?.....	8
1.4 RESEARCH LAYOUT.....	10
2. SODAR AND TOWER OBSERVATIONS	12
2.1 OVERVIEW.....	12
2.2 INSTRUMENTATION AND DATA.....	14
2.3 OBSERVATION ANALYSIS.....	16
2.3.1 NEAR-NEUTRAL CASE (SEPTEMBER 06, 2000).....	17
2.3.2 CONVECTIVE CASE (SEPTEMBER 08, 2000).....	21
2.4 SUMMARY.....	26
3. ADVANCE REGIONAL PREDICTION SYSTEM (ARPS)	27
3.1 OVERVIEW OF THE ARPS MODELING SYSTEM.....	27
3.2 NUMERICAL DETAILS.....	28
3.2.1 INTEGRATION, SMOOTHING, TKE CLOSURE AND RADIATION.....	28
3.2.2 SURFACE FLUXES AND LAND-SURFACE MODEL.....	29
3.3 INITIALIZATION AND BOUNDARY CONDITIONS.....	34
3.4 COUPLING ARPS WITH CALPUFF.....	35

3.5 SURFACE OBSERVATIONS.....	37
4. CALPUFF MODELING SYSTEM.....	40
4.1 BACKGROUND.....	40
4.2 DISPERSION FORMULATION.....	41
5. TROPICAL SEABREEZE CIRCULATION: INFLUENCE ON POLLUTION DISPERSION.....	45
5.1 INTRODUCTION.....	45
5.2 EXPERIMENT DESIGN.....	46
5.3 NUMERICAL MODEL RESULTS.....	48
5.3.1 ARPS METEOROLOGICAL SIMULATION.....	48
5.3.2 CALPUFF DISPERSION SIMULATIONS.....	58
5.4 SUMMARY.....	62
6. EASTERN NORTH CAROLINA REGIONAL SIMULATION.....	64
6.1 REGIONAL 6-KM MODEL DOMAIN.....	64
6.2 SYNOPTIC OVERVIEW.....	67
6.3 SPATIAL VARIATIONS OF THE SIMULATED BOUNDARY LAYER.....	69
6.4 COMPARISON OF SIMULATED AND OBSERVED METEROLOGY.....	85
6.5 SUMMARY OF REGIONAL SIMULATION.....	94

7. RALEIGH AREA HIGH-RESOLUTION METEOROLOGICAL AND AIR DISPERSION SIMULATION	97
7.1 RALEIGH AREA 1KM ARPS DOMAIN.....	97
7.2 SIMULATED 1 KM METEOROLOGY.....	101
7.3 COMPARING SIMULATED METEOROLOGY WITH OBSERVATIONS.....	113
7.4 COUPLED ARPS-CALPUFF DISPERSION SIMULATION.....	124
7.4.1 EXPERIMENT BACKGROUND AND DESIGN.....	124
7.4.2 SIMULATED PM2.5 CONCENTRATIONS FROM ARPS.....	127
7.4.3 SUMMARY.....	137
8. CONCLUSIONS.....	140
LIST OF REFERENCES.....	150

LIST OF TABLES

Table		Page
5.1	Soil properties and initializations values for seabreeze simulation over Mumbai, India.	48
6.1	Performance statistics of the 6 km simulated and observed 2 m temperature including Mean Bias Error (MBE), Variance (VAR), Root Mean Square Error (RMSE), Mean Absolute Error (MAE) and Index of Agreement (IOA). <i>All</i> indicate over the entire time series, <i>Day</i> indicates statistics between 0800 LT and 1900 LT, <i>Night</i> indicates between 2000 LT and 0700 LT. <i>Avg. All</i> is the average statistic of all stations.	87
6.2	Performance statistics of the 6 km simulated and observed 10 m wind speed including Mean Bias Error (MBE), Variance (VAR), Root Mean Square Error (RMSE), Mean Absolute Error (MAE) and Index of Agreement (IOA). <i>All</i> indicate over the entire time series, <i>Day</i> indicates statistics between 0800 LT and 1900 LT, <i>Night</i> indicates between 2000 LT and 0700 LT. <i>Avg. All</i> is the average statistic of all stations.	87
7.1	Performance statistics of the high resolution 1 km simulated and observed 10 m wind speed including Mean Bias Error (MBE), Variance (VAR), Root Mean Square Error (RMSE), Mean Absolute Error (MAE) and Index of Agreement (IOA). <i>All</i> indicate over the entire time series, <i>Day</i> indicates statistics between 0800 LT and 1900 LT, <i>Night</i> indicates between 2000 LT and 0700 LT. <i>Avg. All</i> is the average statistic of all stations.	122

- 7.2 Performance statistics of the 6 km simulated and observed 10 m wind speed including Mean Bias Error (MBE), Variance (VAR), Root Mean Square Error (RMSE), Mean Absolute Error (MAE) and Index of Agreement (IOA). *All* indicate over the entire time series, *Day* indicates statistics between 0800 LT and 1900 LT, *Night* indicates between 2000 LT and 0700 LT. *Avg. All* is the average statistic of all stations. 122
- 7.3 Performance statistics of the high resolution 1 km simulated and observed 2 m temperature including Mean Bias Error (MBE), Variance (VAR), Root Mean Square Error (RMSE), Mean Absolute Error (MAE) and Index of Agreement (IOA). *All* indicate over the entire time series, *Day* indicates statistics between 0800 LT and 1900 LT, *Night* indicates between 2000 LT and 0700 LT. *Avg. All* is the average statistic of all stations. 123
- 7.4 Performance statistics of the 6 km simulated and observed 2 m temperature including Mean Bias Error (MBE), Variance (VAR), Root Mean Square Error (RMSE), Mean Absolute Error (MAE) and Index of Agreement (IOA). *All* indicate over the entire time series, *Day* indicates statistics between 0800 LT and 1900 LT, *Night* indicates between 2000 LT and 0700 LT. *Avg. All* is the average statistic of all stations. 123

LIST OF FIGURES

Figure		Page
2.1	Environmental Protection Agency instrumentation cluster of three trailers. In the foreground is the Model-2000 SODAR, further back is the Model 4000 miniSODAR and in the background is the 10-meter tower.	13
2.2	Eta Data Assimilation System (EDAS) analysis of sea-level pressure and surface wind (10 m), at 2000 LT (00 Z) on September 06, 2000 (Case 1).	17
2.3	GOES-8 satellite image over the region showing deep cloud cover at 2000 LT (00Z) on September 06, 2000 (Case 1).	17
2.4	(Panel a) SODAR reflectivity from Model 2000 and tower measured 10-2 meter temperature difference (K) on September 6, 2001. SR indicates sunrise and SS indicates sunset. (Panel b) Five minute averaged wind speed ($\text{m}\cdot\text{s}^{-1}$) at 2 m (red), 5 m (blue), and 10 m (green). (Panel c) Temperature ($^{\circ}\text{C}$) at 2 meters (blue) and wind direction (red).	18
2.5	Velocity profile data from the Model 4000 miniSODAR on September 06, 2000. (Panel a) Horizontal wind speed ($\text{m}\cdot\text{s}^{-1}$), colors correspond to color bar to the right of the panel. (Panel b) Vertical velocity ($\text{m}\cdot\text{s}^{-1}$) for the same time period.	20
2.6	Eta Data Assimilation System analysis of sea-level pressure and surface wind (10 m) at 0800 LT (12 Z) on September 08, 2000 (Case 2).	21

2.7	GOES-8 satellite image over the region showing very little cloud cover at 1400 LT (18Z) on September 08, 2000 (Case 1)	22
2.8	(Panel a) SODAR reflectivity from Model 2000 and tower measured 10-2 meter temperature difference (K) on September 8, 2001. <i>SR</i> indicates sunrise and <i>SS</i> indicates sunset. (Panel b) Five minute averaged wind speed ($\text{m}\cdot\text{s}^{-1}$) at 2 (red), 5 (blue), and 10 (green) meters. (Panel c) Temperature ($^{\circ}\text{C}$) at 2 meters (blue) and wind direction (red).	23
2.9	Velocity profile data from the Model 4000 miniSODAR on September 08, 2000. (Panel a) Horizontal wind speed ($\text{m}\cdot\text{s}^{-1}$), colors correspond to color bar to the right of the panel. (Panel b) Vertical velocity ($\text{m}\cdot\text{s}^{-1}$) for the same time period.	25
3.1	Plan view of the regional 6 km ARPS domain over central North Carolina. The location of the NC ECO Net surface observing stations are shown.	38
5.1	Figure 5.1 Plan view of the model domain with respect to India and the Arabian Sea.	46
5.2	ARPS vertical coordinate distribution for the tropical seabreeze case.	47
5.3	(a) X-Z cross-section of potential temperature and horizontal wind vectors at 500 LT, 24-hours from the model initialization. The x-axis is in kilometers with 0 km indicating the coastline (CL), negative distance is over the ocean. (b) Same cross-section as (a), but centered and magnified in on the land-sea interface.	49

5.4	(a) X-Z cross-section of potential temperature and horizontal wind vectors at 1000 LT, 29-hours from the model initialization. The x-axis is in kilometers with 0 km indicating the coastline (CL), negative distance is over the ocean. (b) Same cross-section as (a), but centered and magnified in on the land-sea interface.	51
5.5	(a) X-Z cross-section of potential temperature and horizontal wind vectors at 1400 LT, 33-hours from the model initialization. The x-axis is in kilometers with 0 km indicating the coastline (CL), negative distance is over the ocean. (b) Same cross-section as (a), but centered and magnified in on the land-sea interface.	53
5.6	(a) X-Z cross-section of potential temperature and horizontal wind vectors at 1900 LT, 38-hours from the model initialization. The x-axis is in 9ilometers with 0 km indicating the coastline (CL), negative distance is over the ocean. (b) Same cross-section as (a), but centered and magnified in on the land-sea interface.	55
5.7	Time series profile of turbulent kinetic energy (TKE) and potential temperature at a location 5 km inland. Potential temperature is contoured each 1 degree and TKE (m^2/s^2) is shaded with legend shown.	56
5.8	Time series profile of turbulent kinetic energy (TKE) and potential temperature at a location 100 km inland. Potential temperature is contoured each 1 degree and TKE (m^2/s^2) is shaded with legend shown.	58
5.9	Plan view of the point source locations (a,b,c,d).	60

5.10	Concentration pattern of NO _x from the various point sources. Blue shading represents the nighttime concentrations and red shading indicates the simulated daytime concentrations.	60
6.1	Regional view of North Carolina and the location of the 6 km ARPS model domain. Surface station (NC ECO Net) locations are depicted.	65
6.2	(a) Terrain height in meters and (b) soil type for the 6 km ARPS domain.	66
6.3	(a) Vegetation type and (b) surface roughness in meters for the 6 km ARPS model domain.	67
6.4	Eta Data Assimilation System (EDAS) analysis of sea level pressure gradient (mb) and 10 m wind (kt).	69
6.5	GOES-8 visible 1-km satellite image for the region on July 10, 2001 at 1500 LT.	70
6.6	(a) Simulated 10 cm surface temperature (C) and 10 m wind vectors. (b) Simulated 100 m TKE (m ² /s ²) and 10 m wind vectors. Both panels are 8 hr forecast for July 10, 2001 at 1500 LT.	71
6.7	Advanced Very High Resolution (AVHRR) Satellite image showing surface skin temperature (C). (a) July 10, 2001 at approximately 1500 LT (b) July 11, 2001 near 1800 LT.	73
6.8	(a) Simulated vertical cross-section of potential temperature (contoured each 1 degree), TKE (m ² /s ²) and horizontal wind vectors for July 10, 2001 at 1500 LT for the upper cross-section. (b)	76

Same but for lower west-east cross section depicted in Figure 6.8b.

6.9	(a) Simulated 10 cm surface temperature (C) and 10 m wind vectors. (b) Simulated 100 m TKE (m^2/s^2) and 10 m wind vectors. Both panels are 33 hr forecast for July 11, 2001 at 1800 LT.	79
6.10	(a) Simulated vertical cross-section of potential temperature (contoured each 1 degree), TKE (m^2/s^2) and horizontal wind vectors for July 11, 2001 at 1800 LT for the upper cross-section. (b) Same but for lower west-east cross section depicted in Figure 6.8b.	80
6.11	(a) Simulated 10 cm surface temperature (C) and 10 m wind vectors. (b) Simulated 100 m TKE (m^2/s^2) and 10 m wind vectors. Both panels are 43 hr forecast for July 12, 2001 at 0400 LT.	82
6.12	(a) Simulated vertical cross-section of potential temperature (contoured each 1 degree), TKE (m^2/s^2) and horizontal wind vectors for July 12, 2001 at 0400 LT for the upper cross-section. (b) Same but for lower west-east cross section depicted in Figure 6.8b.	84
6.13	Observed and simulated 2 m temperature, 48 hr time series for all NC ECO Net stations.	86
6.14	Observed and simulated 10 m wind speed, 48 hr time series for all NC ECO Net stations.	90
6.15	Observed and simulated wind vectors, 48 hr time series for all NC ECO Net stations.	93
7.1	Plan view of high-resolution 1 km model domain over Raleigh, North Carolina. Major roadways, towns and the NC ECO Net station	98

locations are indicated.

7.2	Terrain and landuse properties over the Raleigh, North Carolina region as parameterized by ARPS.	100
7.3	(a) Simulated 10 cm surface temperature (C) and 10 m wind vectors. (b) Simulated 100 m TKE (m^2/s^2) and 10 m wind vectors. Both panels are for July 10, 2001 at 1500 LT.	102
7.4	Simulated vertical cross-section of potential temperature (contoured each 1 degree), TKE (m^2/s^2) and horizontal wind vectors for July 10, 2001 at 1500 LT for the upper cross-section.	104
7.5	(a) Simulated 10 cm surface temperature (C) and 10 m wind vectors. (b) Terrain height (m) and 10 m wind vectors. Both panels are for July 11, 2001 at 0500 LT.	106
7.5	(c) TKE (m^2s^{-2}) and potential temperature (each 1 K) vertical cross-section through the center of the 1 km model domain at 0500 LT on July 11 th , 2001.	107
7.6	(a) Simulated 10 cm surface temperature (C) and 10 m wind vectors. (b) Simulated 100 m TKE (m^2/s^2) and 10 m wind vectors. Both panels are for July 11, 2001 at 1400 LT.	109
7.7	Simulated vertical cross-section of potential temperature (contoured each 1 degree), TKE (m^2/s^2) and horizontal wind vectors for July 11, 2001 at 1400 LT for the upper cross-section.	110
7.8	(a) Simulated 10 cm surface temperature (C) and 10 m wind vectors. (b) Terrain height (m) and 10 m wind vectors. Both panels are for July 12, 2001 at 0500 LT.	112

7.9	Aerovironment Model 2000 SODAR observed reflectivity (dB) for July 10, 2001 (0800 LT) to July 12, 2001 (0800 LT). Simulated potential temperature is contoured (K) each 1 degree for the corresponding period.	114
7.10	Aerovironment Model 4000 miniSODAR observed reflectivity for July 10, 2001 (0800 LT) to July 12, 2001 (0800 LT).	116
7.11	Simulated potential temperature (contoured 1 degree), TKE (shaded) and wind (kt) profile (upper). Aerovironment Model 2000 observed wind profile (kt) for July 10, 2001 (0800 LT) to July 11, 2001 (0800 LT).	118
7.12	Simulated potential temperature (contoured 1 degree), TKE (shaded) and wind (kt) profile (upper). Aerovironment Model 2000 observed wind profile (kt) for July 11, 2001 (0800 LT) to July 12, 2001 (0800 LT).	120
7.13	MicroFacPM simulated, diurnal PM _{2.5} concentration (g/km/hr) along Capital Blvd.	126
7.14	Simulated 1 hr average PM _{2.5} concentration (ug/m ³) and 10 m wind vectors at July 10 th at 1000 LT.	128
7.15	Simulated 1 hr average PM _{2.5} concentration (ug/m ³) and 10 m wind vectors at July 10 th at 1500 LT.	129
7.16	Simulated 1 hr average PM _{2.5} concentration (ug/m ³) and 10 m wind vectors at July 10 th at 1800 LT.	131
7.17	Simulated 1 hr average PM _{2.5} concentration (ug/m ³) and 10 m wind	132

vectors at July 10th at 2100 LT.

7.18	Simulated 1 hr average PM _{2.5} concentration (ug/m ³) and 10 m wind vectors at July 11 th at 0200 LT.	133
7.19	Simulated 1 hr average PM _{2.5} concentration (ug/m ³) and 10 m wind vectors at July 11 th at 0800 LT.	134
7.20	Simulated 1 hr average PM _{2.5} concentration (ug/m ³) and 10 m wind vectors at July 11 th at 1800 LT.	135
7.21	Simulated 1 hr average PM _{2.5} concentration (ug/m ³) and 10 m wind vectors at July 12 th at 0200 LT.	136
7.22	Simulated 1 hr average PM _{2.5} concentration (ug/m ³) and 10 m wind vectors at July 12 th at 0700 LT.	137

LIST OF SYMBOLS

b	Slope of the moisture retention curve of soil
C_1	Coefficient of the net precipitation
C_2	Coefficient of the perturbed near surface moisture content
C_d	Surface exchange (drag) coefficient for momentum
C_g	Thermal coefficient for bare soil
C_{gsat}	Thermal coefficient for bare soil at saturation
C_h	Surface exchange (drag) coefficient for heat
C_q	Surface exchange (drag) coefficient of moisture
C_t	Thermal coefficient for the surface
C_v	Thermal coefficient for vegetation
E_g	Evaporation from the ground
E_r	Evaporation from the plant canopy
E_{tr}	Transpiration
F_1	Fractional conductance of photosynthetically active radiation
F_2	Fractional conductance of water stress
F_3	Fractional conductance of atmospheric vapor pressure
F_4	Fractional conductance of air temperature
f_y	Dimensionless time function in the horizontal

f_z	Dimensionless time function in the vertical
F_w	Wet fraction of the canopy
g	Gravitational acceleration
h_u	Relative humidity at the ground surface
H	Sensible heat flux
k	von Karman constant
L	Monin-Obukhov length
L_e	Latent heat of evaporation
LE	Latent heat flux
h	Length scale
h_0	Length scale, scaled by the roughness length
r_a	Air density
P	Precipitation rate
P_g	Residual of the precipitation rate at the ground
p	3.1415186
Pr_0	Prandtl number
r_w	Density of water
q	Specific humidity
q_s	Specific humidity at the surface
q_{va}	Specific humidity at the first model level above the surface
q_{vsat}	Saturated specific humidity near the surface

R_a	Aerodynamic resistance
R_g	Short wave radiation at the surface
Ri_b	Bulk Richardson number
R_n	Net radiation at the surface
R_s	Surface resistance to evapotranspiration
$R_{s\min}$	Minimum of surface resistance
s_v	Horizontal fluctuation in velocity
s_w	Vertical fluctuation in velocity
s_{yt}	Time dependent dispersion coefficient in the crosswind direction
s_{zt}	Time dependent dispersion coefficient in the vertical direction
t	Length of day
q	Potential temperature
q_0	Potential temperature near the surface
q_s	Potential temperature at the surface
\overline{q}_v	Mean virtual potential temperature in the surface layer
t	Time
t_{ty}	Time scale in the horizontal
t_{tz}	Time scale in the vertical
T_2	10 to 100 cm soil temperature
T_s	Surface to 10 cm soil temperature
$\overline{u'w'}$	Momentum flux in the x-direction

u	Velocity component in x-direction
u^*	Friction velocity
U	Horizontal wind speed
V	Velocity component in y-direction
\bar{V}	Mean wind speed at 10 m
veg	Vegetation percentage
w_*	Convective velocity scale
w	Velocity component in z-direction
W_2	10-100 cm soil moisture
W_g	Surface to 10 cm soil moisture
W_{geq}	Surface moisture when gravity and the capillary forces are balanced
W_r	Canopy moisture
W_{sat}	Soil saturation moisture
$\overline{w'q'}$	Kinematic heat flux
$\overline{w'q'}$	Kinematic moisture flux
c	Similarity function
c_0	Similarity function scaled by the surface roughness
z	Height above the surface
z_i	Boundary layer height
z_0	Surface roughness
y_m	Stability correction term for momentum

y_h Stability correction term for heat

CHAPTER 1

INTRODUCTION

1.1 ATMOSPHERIC BOUNDARY LAYER AND AIR POLLUTION DISPERSION

Boundary layer meteorological processes are among the most important, fundamental aspects of atmospheric flow in relation to air pollution. The exchange and diffusion of heat, moisture, momentum, gases and particulates principally take place within the lowest kilometer of the troposphere. It is mainly the interaction between the atmosphere and earth's surface that drives circulations from micro-scale up to global-scale.

Micro-scale interactions, on the order of 10^{-3} to 10^3 meters and seconds, are where this complex scale interaction begins. Air motion is slowed near the surface because of friction or shear stress. The resulting wind shears in the vertical produce turbulent motions or turbulent kinetic energy (TKE) within the boundary layer. Solar radiation causes surface heating, which is another main contributor to turbulence in the atmospheric boundary layer. The air above the surface warms through conduction and convection and becomes buoyantly unstable; transferring this heat upwards in the form of growing eddies. This mechanism of turbulent heat transfer (eddy diffusivity) is much more efficient than molecular diffusion or thermal conduction (Arya, 2001). Evaporated moisture is transported from the surface to greater heights because of this same vertical turbulent transport. By the time the surface heating is maximized, this coalesce of TKE has generated an efficient mixing mechanism from the surface to, in many cases, more than 10% the height of the entire troposphere or approximately 1000 m.

Pollution sources, both man-made and natural, are in most cases near the earth's surface within the atmospheric boundary layer. For this reason, boundary layer processes are essential in transporting, diffusing and diluting pollutants. Air pollution diffusion is controlled by several factors. Following a polluted parcel in the mean flow, turbulent fluctuations of the velocity will effectively cause the plume to expand in all directions as it is transported by the mean wind. These kinematic factors are the principal mechanisms that influence how pollutants emitted from a source are transported by the mean flow and diffused by turbulence.

An additional major factor that influences dispersion is the height of the boundary layer, sometimes referred to as the mixing height. This depth limits the vertical diffusion and therefore has a significant impact on boundary layer pollution concentrations. Lower boundary layer heights correspond to higher concentrations. The diffusion process becomes even more complicated in non-homogeneous boundary layers. Not considering synoptic scale systems, variations in the boundary layer can be directly related to changes in the surface characteristics. Hence, non-uniform surface features will result in complex variations of all the factors that affect pollution dispersion, ultimately leading to complex dispersion patterns.

How does the boundary layer vary over a sub-region and how do these small-scale variations influence the sub-regional to regional meteorological conditions and associated air quality? Can smaller scale boundary layer variations noticeably influence dispersion patterns?

Certain notable variations have been investigated including urban heat island effect (Oke, 1987), inland circulations caused by vegetation gradients (Bechtold, 1991),

topographically induce flows and others. It is known that small-scale heterogeneities related to the surface can create variations in the boundary layer structure. The surface variations examined in this thesis are those of topography, soil texture (type), soil moisture, surface roughness and vegetation cover.

Different soil types possess different physical properties and therefore heat and cool differently. Arya (2001) indicates that the thermal properties of soils depend on the solid particles, size distribution, porosity and moisture content. Gradients in soil types alone can cause gradients in surface heat and moisture fluxes, thus gradients in the boundary layer properties. A study by Li and Avissar (1994) concluded that the influence of soil properties dominant the surface fluxes when vegetation cover is low.

Surface roughness is a function of the landuse. Forest areas with tall trees stimulate more resistance or friction to the flow when compared to an open field, lake or ocean. This in turn influences the amount of turbulent shear energy as well as the mean wind speed near the surface. Internal boundary layers can form due to sudden changes in roughness, wherein the vertical distribution of momentum and heat as well as surface fluxes will vary. Surface roughness has been noted in studies to influence the boundary layer structure most during neutral to stable stability regimes (Li and Avissar, 1994)

Vegetation cover can have a conspicuous effect on the boundary layer. Locations of high vegetation such as a thick forested area, shades the surface from solar radiation and therefore do not allow the surface to heat as much as an open field. In addition, elevated transpiration results in a cooling effect on the encased canopy air, keeping these microenvironments relatively cooler than surrounding open areas. Additionally, boundaries between highly vegetated and less vegetated open areas can induce small-

scale circulation, clouds and even precipitation in some cases. Bougeault et al. (1991) and Lyons et al. (1993) support this through both numerical modeling and observational studies.

Topography is another surface feature that can distinctly influence the boundary layer flow and turbulence. During stable, light wind conditions, a cooling surface in addition to the slope of a hill will cause the heavier cooler air to flow down the slope into the valley. Also, during strong statically stable conditions, hills can cause the flow to diverge around, rather than cross over the slope. Within a highly variable topographic locale, the boundary layer meteorology can be similarly as complicated.

Synoptic scale weather patterns present additional complexity in terms of the boundary layer properties affecting pollution dispersion. Active weather is more conducive to quick, efficient pollution dispersion and removal. Stronger wind leads to greater instability, turbulence and thus effective dilution. Stronger wind swiftly transports local pollutants away from the source region. Rainfall typically accompanies synoptic low-pressure systems, and can within hours remove a majority of pollutants through wet deposition.

On the contrary, stagnant high-pressure systems usually bring light wind, clear skies and subsidence aloft. Light wind reduces the transport of pollutants away from source regions. Pollutants are therefore allowed to load the atmosphere over the typically seen high-pressure residence period of a few days. Absence of cloud-cover allows for effective radiational cooling at night, causing a more stable nocturnal boundary layer to form. This increase in static stability reduces the wind speed near the surface as well as the boundary layer height; both factors may lead to an increase in surface concentration

from near-surface sources. Warm, statically stable air aloft limits the growth of the convective boundary layer and can therefore cause boundary layer concentrations to be higher. This coupled with clear skies during the day is a recipe for enhanced ozone production.

With all these factors considered, air pollution dispersion is strongly dependent on the spatially variable and non-stationary boundary layer meteorology. For this reason, dispersion models need comprehensive meteorology, which takes into account complex surface features that effect the boundary layer.

1.2 RESEARCH OVERVIEW AND OBJECTIVES

The main objective of this investigation is to couple a mesoscale atmospheric model, Advanced Regional Prediction System (ARPS) with an air pollution dispersion model (CALPUFF) in order to study how small-scale boundary layer variability influences pollution transport and diffusion. To initiate the study, detailed observations from several SOund Detection And Ranging (SODAR) units as well as a 10 m micrometeorological tower are examined during several stability conditions. Then, simulations are conducted to explore the relationship between pollution dispersion and boundary layer variability. The first numerical investigation examines the effect of the seabreeze and land breeze system on pollution dispersion patterns over a tropical region (Mumbai, India). The second set of simulations is over the central North Carolina region. The courser simulation is at the regional scale while the second examines the local scale meteorology. In support of the primary goal, the local scale simulation is used to investigate how landuse variations may affect roadway emission dispersion patterns.

Additionally, the ARPS model simulations are statistically evaluated using surface observations from the North Carolina Environmental Climate Observing Network (NC ECO Net).

The U.S. Environmental Protection Agency, National Exposure Research Laboratory (EPA/NERL) has an instrumentation cluster that facilitates high-resolution temporal measurements near the surface. This ensemble consists of three portable trailers supporting an Aerovironment Model 4000 miniSODAR, Aerovironment Model 2000 SODAR and three-level 10 m micrometeorological tower. The emphasis here is on the diurnal structure of the surface layer using this observing system. Two 24 hr cases are inspected in which the meteorological conditions are dissimilar. The first observational period occurs during a high wind and deep cloud cover scenario; it is considered near neutral during both the daytime and nighttime hours. Conversely, little cloud cover and light wind govern the meteorology of the second case. For this case, the boundary layer is dominated by free convection during the day and strong thermal stability at night. An attempt is made to distinguish differences in the surface layer structure between two cases by examining the wind profiles, surface stability and SODAR observations.

The seabreeze-land breeze case centers on the area around Mumbai, India. Mumbai is a large urban area on the Arabia Sea coast. Because of this location, the city regularly experiences both sea and land breezes. The seabreeze has the capability of drastically changing boundary layer properties, and thus the dispersion of pollutants within the boundary layer (Lyons, 1975; Kitada and Ueda, 1989; Rhome et. al., 2001). A case study is presented to investigate the diurnal boundary layer structure of an area affected by the seabreeze. Specific relations are investigated including how the stability,

turbulence and wind field is modified by this mesoscale circulation. Using simulated meteorological fields from the ARPS model, dispersion pattern from the CALPUFF model is examined along with boundary layer variations directly caused by air-sea interactions.

A coupled model utilizing the Advanced Regional Prediction System (ARPS) mesoscale model and CALPUFF dispersion model is used to examine a case which the meteorological conditions represent typical conditions in the region. The ARPS mesoscale model is setup over the region with a base grid spacing of 6 km and nested grid spacing of 1 km. These domains employ 1 km USGS surface characteristics and 30 second terrain information to define the lower boundary (earth surface). A 48-hr case for the 6 km domain is presented in which the model is initialized and boundary conditions are forced by assimilated data from the 32-km ARPS Data Assimilation System (ADAS). The meteorology is examined for variations that may be attributed to surface heterogeneity. In order to acquire some confidence that the model is performing reasonably, meteorological observations are compared to simulated fields. These observations include surface data from the North Carolina Environmental Observing Network (NC ECO Net) (Niyogi et. al., 1998). In addition, the high-resolution 1 km simulation is examined in a similar manner. This includes an investigation on the reaction of the boundary layer to surface variations as well as a comparison with NC ECO Net surface data and the EPA's meteorological instrumentation cluster of trailers (MIC-3). This cluster includes the two Sound Detection And Ranging systems (SODAR's) and a 10 m meteorological tower. The SODARs are used to examine the vertical structure of the lower boundary layer and for comparison to the simulations. Finishing the analysis,

dispersion patterns from the ARPS-CALPUFF coupled simulation are evaluated for responses to variations in the boundary layer meteorology resulting from surface heterogeneities.

1.3 WHY COUPLE ARPS AND CALPUFF?

The CALPUFF modeling system is one of the more advanced dispersion models available and will soon be certified as a regulatory model of the United States Environmental Protection Agency (US EPA). CALPUFF has a micrometeorological module that takes in hourly surface observations, standard twice-daily upper-air observations and USGS land use land-cover information. From this data, using several boundary layer parameterization schemes, the structure of the atmospheric boundary layer is estimated. Variables such as boundary layer height, Monin-Obukhov length, friction velocity and convective velocity scale are approximated from the surface and upper air data. As mentioned previously, a goal of this research is to bypass the diagnostic model (CALMET) used with CALPUFF and employ a more robust, physically sound, mesoscale model (ARPS) to obtain the required boundary layer variables.

The reasons for using ARPS in place of CALMET are as follows. First, ARPS is based on the primitive equations of motion, includes explicit cloud physics, TKE closure scheme based boundary layer physics and includes a sophisticated scheme for the surface processes. Thus, ARPS can provide a better simulation of the atmosphere. CALMET is more of an objective analysis, pure parameterization model. In short, the governing equations and physics used in ARPS are more realistic than those used in CALMET.

Secondly, CALMET uses twice-daily upper-air soundings at 00 and 12 Z to calculate the vertical structure of the boundary layer. In the eastern United States, these soundings are taken in the morning and evening. Both are the times when the boundary layer is in a transitional state. Between the soundings, an equation is used to describe the heating and cooling within the boundary layer using the hourly-observed surface temperature. In many cases this cannot accurately describe the actual evolution of the boundary layer. In addition, upper-air observations are sparsely spaced across the continental United States. If one is interested in smaller-scale dispersion, for example a city scale domain, it will be difficult to have a rawinsonde station within or even near the domain. For example, a CALMET domain set up over Raleigh, North Carolina would use the upper-air observations from Greensboro (~150 km) and Morehead City (250 km) to quantify the boundary layer. ARPS on the other hand uses the assimilated data, which includes these upper-air observations, radar, satellite, surface as well as model data.

CALMET uses wind observations to objectively derive the spatial and temporally varying wind field within the model domain. In many cases, especially when smaller scale simulations are of interest, few surface observations are available. For this reason, it is not possible to simulate smaller scale circulations such as seabreeze systems, landuse induced circulations and topographically influenced flows. ARPS has the physical equations that more realistically simulate these smaller scale features.

On a similar theme, ARPS can better simulate the surface-atmosphere interactions. This modeling system uses a soil/vegetation model after Noilian and Planton (1989) to physically describe the influence that soil texture, vegetation cover, leaf-area index, surface roughness and soil moisture have on the boundary layer. CALMET uses

similar information along with an equation for the surface energy balance to derive the surface heat flux. Cloud-cover is used from the surface observations to estimate the incoming solar radiation, which in many cases is not available. The net radiation at the surface in combination with a specified Bowen ratio and a ground heat flux parameter is used for this heat flux estimation. Soil moisture is indirectly included as a constant Bowen ratio term for each landuse category. In ARPS the soil moisture is explicitly forecasted, which allows for changes during the simulation. Also, initial values of soil moisture from the ARPS Data Assimilation System (ADAS) analysis takes into account precipitation history. In short, the ARPS model is more physically advanced.

1.4 RESEARCH LAYOUT

Background information on this research has been presented. The following is a brief description of how this thesis is structured. Chapter 2 provides particulars on the instrumentation cluster, and then presents several sets of data for the various cases discussed earlier in this chapter. Chapter 3 furnishes details on the mesoscale model ARPS and how the model was configured for this investigation. Chapter 4 outlines the CALPUFF dispersion model and gives specifics of how the model estimates atmospheric dispersion. Chapter 5 reports the results of a tropical seabreeze simulation over Mumbai, India. Following, results of a regional simulation over the eastern North Carolina are provided in Chapter 6. To conclude the investigation, Chapter 7 will provide details of a high-resolution meteorological simulation centered over Raleigh, North Carolina. In addition to the meteorological simulation, a dispersion simulation of roadway emissions

is presented utilizing the CALPUFF model. Chapter 8 wraps up the investigation by summarizing each experiment and provide future plans and expectations.

CHAPTER 2

SODAR AND TOWER OBSERVATIONS

2.1 OVERVIEW

Instruments including SOUNd Detection And Ranging (SODAR), Light Detection and Ranging (LIDAR), towers, tetrons, and others allow probing of the lower atmosphere, the planetary boundary layer (PBL). The U.S. Environmental Protection Agency, National Exposure Research Laboratory (EPA/NERL) has an instrumentation cluster that facilitates high-resolution temporal and spatial measurements close to the surface. This consists of three portable trailers (Figure 2.1) supporting an Aerovironment Model 4000 miniSODAR (SOUNd Detection and Ranging), Aerovironment Model 2000 SODAR and three-level micrometeorological tower.

It is well known that when the boundary layer is stable, typically at night, wind speed increases with height to the top of the nocturnal boundary layer. The height of the nocturnal boundary layer is often associated with a core of high winds, a nocturnal jet (Stull, 1988). During near-neutral conditions the wind profile has a logarithmic distribution with height in the lower part of the planetary boundary layer, called the surface layer. Unstable conditions (convective), with light wind and high insolation situations yield a rapidly increasing wind speed in the shallow surface layer and near constant wind speed profile in the mixed layer.

Local meteorology is a key factor in both diurnal and day-to-day changes in the ambient pollution concentration levels affecting human exposure. Typically, air quality problems arise most often when large scale forcing is weak. It is this situation when local



Figure 2.1 Environmental Protection Agency instrumentation cluster of three trailers. In the foreground is the Model-2000 SODAR, further back is the Model 4000 miniSODAR and in the background is the 10-meter tower.

meteorology dominates. Routine National Center for Environmental Prediction (NCEP) models provide gridded meteorological data for the entire United States, but the resolution of this data is not sufficient for determining local meteorology for the support of small scale pollution modeling. Similarly, routine meteorology measured at airports or other stations is only representative of the surrounding area. The EPA/NERL cluster of instruments is being used to support site-specific field studies of human exposure to pollutants. These measurements of local meteorology near the surface are used to develop and evaluate a local scale meteorological modeling system for general application in

support of human exposure modeling. Air quality and consequently exposure of humans will be affected by the local meteorology.

This section of the thesis presents observation from a field site near EPA's facilities in Research Triangle Park, North Carolina. The focus at this point is on the diurnal structure of the surface layer using the observing systems. An attempt is made to distinguish differences in the surface layer structure between three stability regimes and make qualitative comparisons with various boundary layer theories.

Observations are analyzed where the meteorological conditions are extremely unstable or convective during the day (Pasquill's stability class A) and weakly to moderately stable at night (Class E/F). These stability classes are defined and widely used in air quality models (Arya, 1999). In addition, a case is examined where the day and night stability is near neutral (Class D), i.e. a cloudy-windy scenario (Stull, 1988). The observational analysis includes SODAR velocity profiles, 10-2 m temperature differential (ΔT_{10m-2m}), 2 m temperature, 10 m wind speed and direction and SODAR reflectivity (digital facsimile).

A description of the two SODARs, 10 m tower, and site layout is given in the following section. Observations for two 24-hr periods will be analyzed and discussed with one near-neutral case and another with convective boundary layer during the day and stable boundary layer at night.

2.2 INSTRUMENTATION AND DATA DESCRIPTION

The miniSODAR is a high-resolution surface layer (15 to 200 m range at 5 m intervals, 5 minute averaged) wind sampler. It transmits sound at a frequency of 4500

Hz, which mitigates environmental noise interference (Crescenti, 1998), leading to a better representation of the surface layer wind distribution and variance. A previous study evaluating the performance of ground based meteorological instruments including the same miniSODAR found a high correlation with tower measurements (Crescenti, 1999).

SODAR systems use sound to sample the boundary layer, emitting a pulse and receiving reflections from small gradients of temperature and moisture. Turbulent mixing is the main cause for these gradients. Frequency shifts (Doppler effect) from the transmitted to returned signal are translated as moving parcels of air, where the velocity is directly related to the frequency shift. Algorithms extract other related parameters such as standard deviations of the wind components, vertical velocity, and return signal intensity (reflectivity). The standard deviations provide useful information on the turbulence intensities while the return signal intensity may be used to distinguish mixing layers, both of which are important factors in air pollution dispersion.

An additional SODAR unit, Aerovironment Model 2000 SODAR, measures these same wind properties from 60 to 600 m at 30 m intervals, and averaged over a 10 minute period. This unit provides important data from the convective mixed layer, verifies the performance of the miniSODAR, and gives boundary layer heights when below 600 m. Additionally, the boundary layer height evolution after sunrise and before sunset can typically be assessed with this unit.

The 10 m micrometeorological tower has instruments that measure wind (Young Model 05701 anemometer) at 2, 5, and 10 m along with temperature and relative humidity (Gill aspirated Model 43408) at 2 and 10 m. This “ground truth” instrumentation is valuable for evaluating the accuracy of the SODAR observations and

providing the lower level observations not sampled by either SODAR. The temperature observations, especially the difference between 2 and 10 m, provide valuable information on the static stability of the surface layer. All tower data are sampled each second then averaged and stored at 5 min intervals.

The observation site is located in Research Triangle Park, NC at a site called Jenkins Road. SODAR instrumentation was positioned in the center of an open field surrounded by 10 to 15 meter trees, at least 100 m away in all directions. The surrounding forest dampens the ambient noise level; this allows less interference and therefore more reliable SODAR data (Crescenti, 1998). The micrometeorological tower was located 3 km to the east with very similar surroundings.

2.3 OBSERVATION ANALYSIS

Two case analyses are offered below. For the first case (near-neutral case on September 06, 2000), diurnal 10 m wind speed remained strong (averaged 3 to 4 m s^{-1}) and constant through most of the period. The diurnal temperature range was small, less than 5° C, while the difference in temperature between 2-10 m was near zero.

The second case (Convective Case on September 08, 2000) had light daytime 10 m winds (less than 3 m s^{-1}) with a diurnal 2 m temperature range greater than 10° C. At night the 10 m wind speed averaged 1 m s^{-1} and the mean temperature difference between 10 m and 2 m was positive. This combination indicates a stable nocturnal boundary layer at night.

2.3.1 NEAR-NEUTRAL CASE (SEPTEMBER 06, 2000)

The near-neutral case occurred during a cold air-damming event. These occurrences are characterized by strong surface high pressure developing over New England resulting in brisk north-northeast wind over the Mid-Atlantic States. As a result, cool Maritime polar air from the North Atlantic is transported into the region. Figure 2.2 provides the ETA analysis (EDAS) for 2000 LT (0000 UTC), which includes sea-level pressure (shaded) and 10 m wind. Typically, a warm-moist southwesterly flow overrides the cooler air at the surface. The result is cool, breezy, and cloudy weather. Figure 2.3 shows a visible satellite image at 1800 LT on this day, in which deep cloud cover envelops the region.

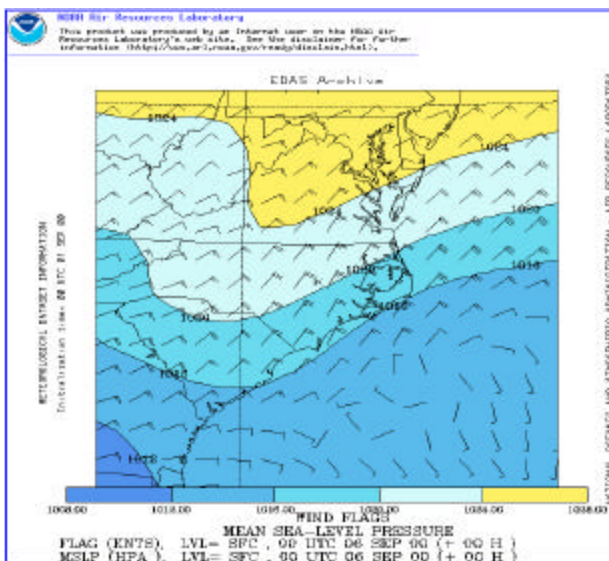


Figure 2.2 Analysis of sea-level pressure and surface wind (10 m) at 2000 LT (00 Z) on September 06, 2000 (Case 1:neutral).

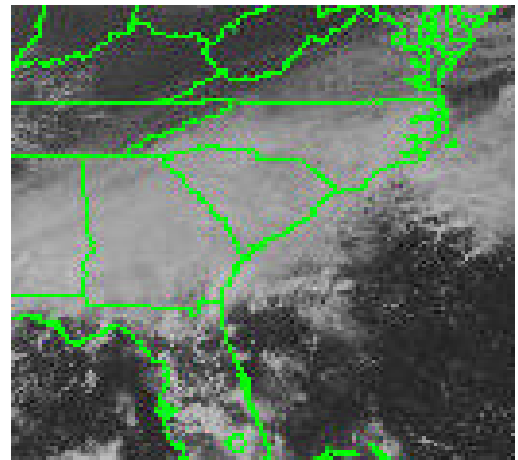


Figure 2.3 GOES-8 satellite image over the region showing deep cloud cover at 2000 LT (00Z) on September 06, 2000 (Case 1: neutral).

Figure 2.4(a) presents the digital facsimile analysis (DFS) for this case as seen by the Model 2000 SODAR. The surface layer (SBL) remains at a constant depth of 100 m for the 24-hour period. At night strong shear production overcomes negative buoyancy,

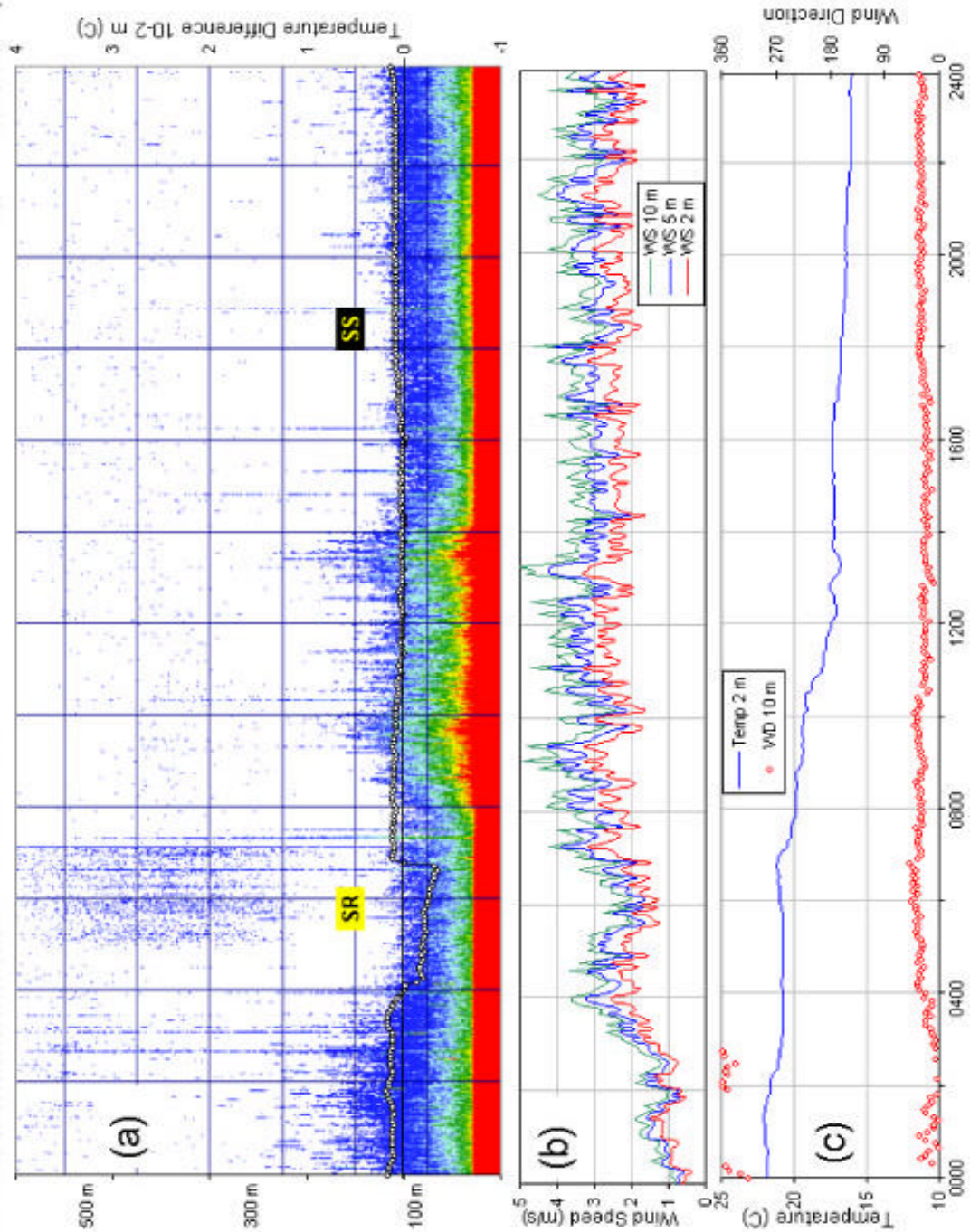


Figure 2.4 (a) SODAR reflectivity from Model 2000 and tower measured 10-2 meter temperature difference (K) on September 6, 2001. **SR** indicates sunrise and **SS** indicates sunset. (b) Five minuet averaged wind speed ($\text{m}\cdot\text{s}^{-1}$) at 2 (red), 5 (blue), and 10 (green) meters. (c) Temperature ($^{\circ}\text{C}$) at 2 meters (blue) and wind direction (red).

resulting in a near neutral flow. During the daytime little change takes place because heavy cloud cover and limited solar insolation does not allow the surface to heat. In

addition, brisk winds kept the surface layer well mixed. These types of cloudy, windy conditions typically cause the surface layer to remain near neutral (Stull, 1988).

The SODAR reflectivity (Figure 2.4a) is consistent with near-neutral conditions. Evenly distributed echoes are a result of uniform small-scale temperature and specific humidity gradients that reflect sound wave signals back to the SODAR receiver. It is possible that humidity gradients may be a key source of the sound reflections. On this day, the soil moisture was high ($0.33 \text{ m}^3 \cdot \text{m}^{-3}$) and it appears that cold/dry air advection took place. This sets up a stronger than normal moisture gradient near the surface.

Temperature gradient between 2 m and 10 m ($\Delta T_{10\text{m}-2\text{m}}$) is plotted on the digital facsimile plot (Figure 2.4a). This vertical temperature gradient provides a measure of static stability. Temperature difference between the two levels remains close to zero for the 24-hr period, further suggesting a near-neutral surface layer.

Tower wind speed measurements in Figure 2.4b, indicate an increase in wind speed at 0300 LT from 1.5 to 4 ms^{-1} . At the same time, the near surface temperature difference (Figure 2.4a) transitions from slightly stable to slightly unstable. It is believed that the cold air advection is initiated at this time as a cool front passed through the region. Figure 2.4c gives the 2 m temperature time series along with the wind direction. The air temperature variation supports cold air advection and cool frontal passage. After the cool front passes (0300 LT) the temperature declines through the remainder of the day. Steady northeasterly wind direction was present for the whole period.

Figure 2.5a presents the vertical profile of horizontal wind speed for the same case. A fairly regular pattern is seen throughout the diurnal period. It is noticed that there are repeating intervals where the wind speed increases and decreases. These periodic

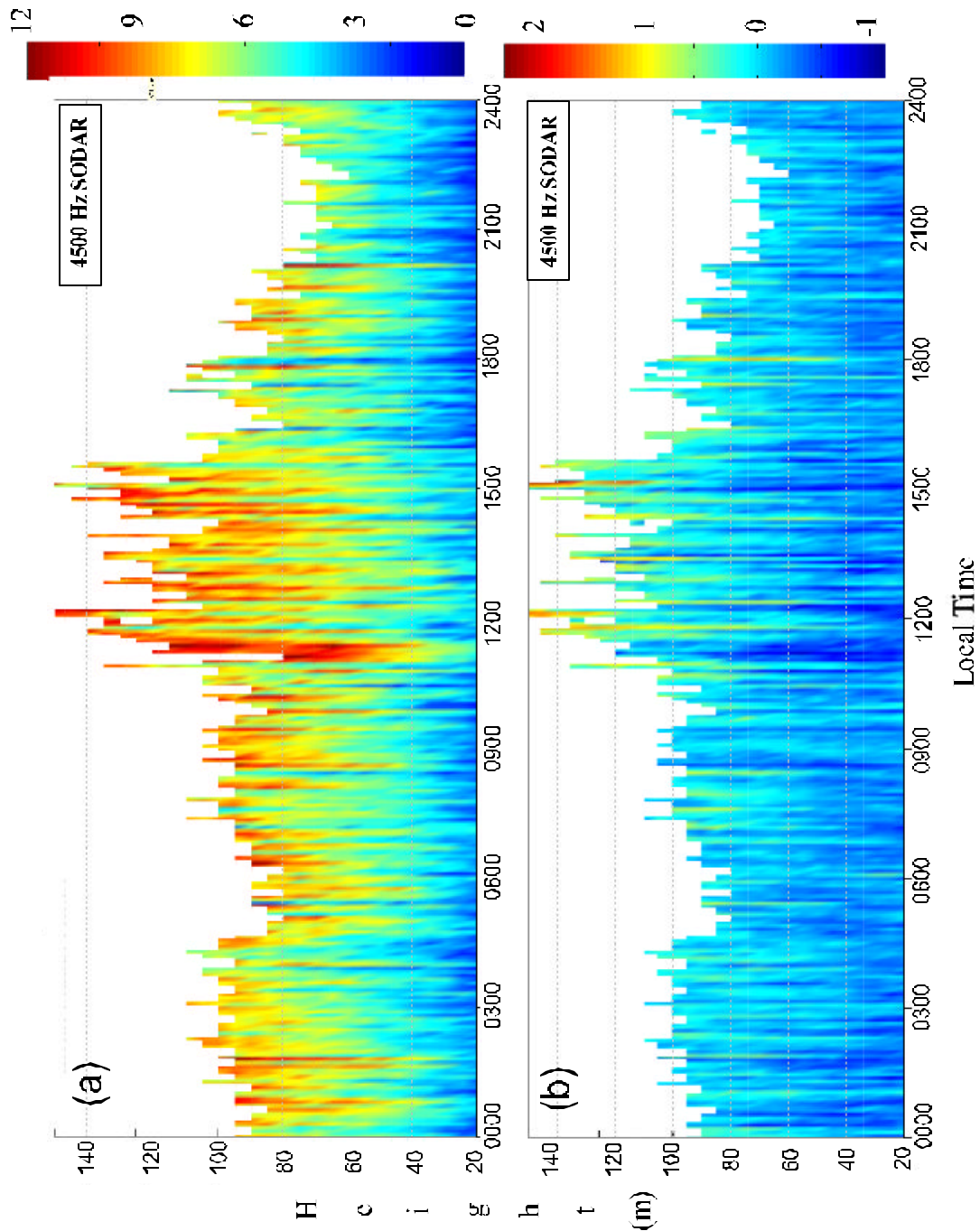


Figure 2.5 Velocity profile data from the Model 4000 miniSODAR on September 06, 2000. (a) Horizontal wind speed ($\text{m}\cdot\text{s}^{-1}$), colors correspond to colorbar to the right of the panel. (b) Vertical velocity ($\text{m}\cdot\text{s}^{-1}$) for the same time period.

bursts of momentum correspond to strong boundary layer eddies formed by shear stress with the surface. In general, the increase in wind speed with height is uniform during the

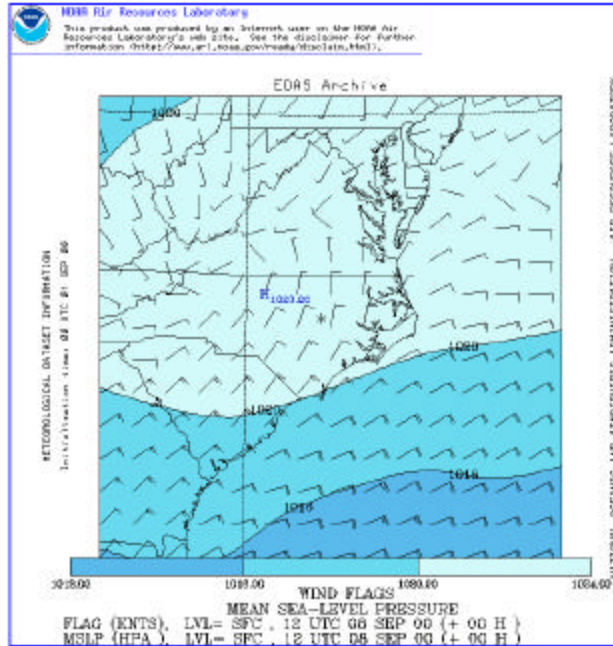


Figure 2.6 Analysis of sea-level pressure and surface wind (10 m) at 0800 LT (12 Z) on September 08, 2000 (Case 2).

period. Figure 2.5b shows the vertical velocity measured from the miniSODAR for the same case. An interesting correlation exists between the horizontal wind speed in Figure 2.5a and the vertical velocity in Figure 2.5b. At the same points in time where the horizontal wind speed increases, the vertical velocity becomes negative. This indicates that the bursts of wind are associated with downward motion or a transfer of momentum downward. Boundary layer momentum flux, from higher to lower (down gradient transfer), is what these observation are explicitly showing.

2.3.2 CONVECTIVE CASE (SEPTEMBER 08, 2000)

Case 2 occurred on a day when the wind speed was light and solar insolation not hampered by cloud cover. Figures 2.6 and 2.7 present the sea level pressure, 10 m wind and a satellite image at 1800 LT. Both figures confirm the description of the meteorology

for this case. These types of conditions are conducive for a convective boundary layer where buoyancy driven turbulence dominates.

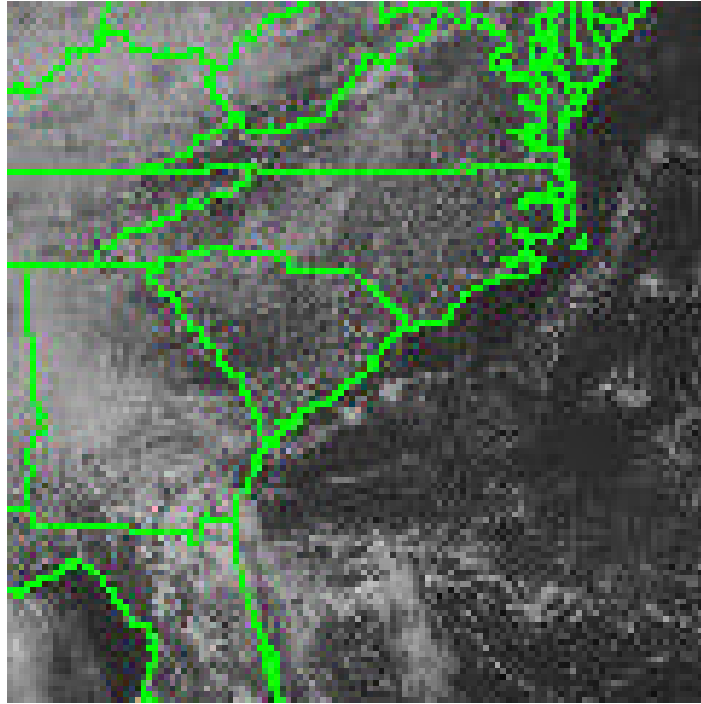


Figure 2.7 GOES-8 satellite image over the region showing very little cover at 1400 LT (18Z) on September 08, 2000 (Case 1).

Figure 2.8a shows the digital facsimile analysis (DFS) from the Model 2000 SODAR. Between midnight and approximately 0615 LT the temperature difference corresponds to a slightly stable surface layer (dotted line overlaid on DFS). The DFS data indicates the stable nocturnal boundary layer height decreasing from 150 m to 120 m. After sunrise (0800 LT) the static stability becomes unstable in response to surface heating. At this point, the boundary layer begins an exponential growth. By 1000 LT the boundary layer height is above SODAR detection and the PBL becomes convective. It is noticed that strong surface layer thermals periodically arise, similar to convective SODAR data presented by Gera and Saxena (1996). The reflectivity, much greater than

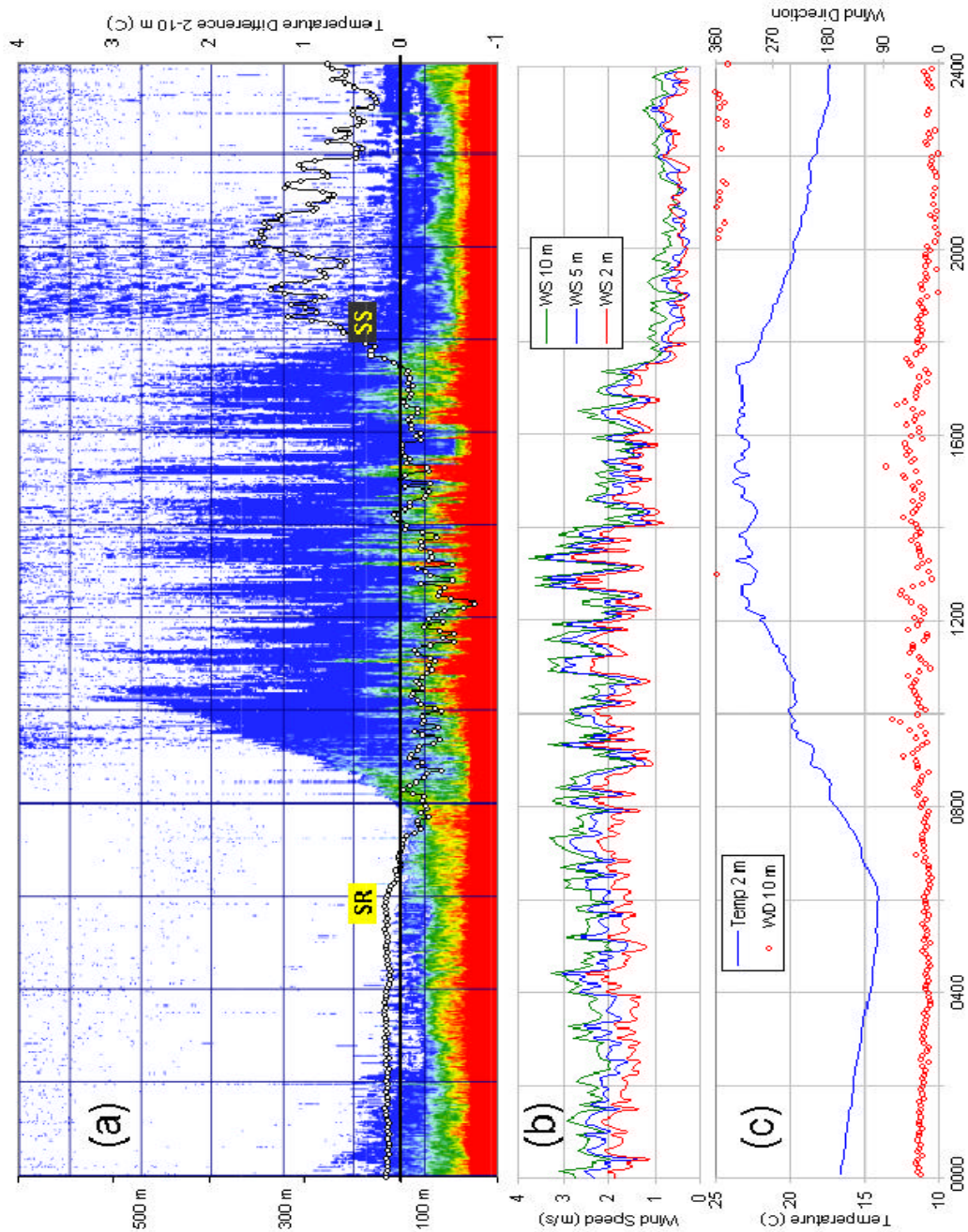


Figure 2.8 (a) SODAR reflectivity from Model 2000 and tower measured 10-2 meter temperature difference (K) on September 8, 2001. **SR** indicates sunrise and **SS** indicates sunset. (b) Five minute averaged wind speed ($\text{m}\cdot\text{s}^{-1}$) at 2 (red), 5 (blue), and 10 (green) meters. (c) Temperature ($^{\circ}\text{C}$) at 2 meters (blue) and wind direction (red).

the previous neutral case, is indicative of intense temperature gradients within these thermals. The periodic decrease in the $\Delta T_{10\text{m}-2\text{m}}$ corresponds well with the intense

SODAR echoes. Around 1800 LT the static stability transitions to stable once again. At this point, the boundary layer quickly collapses to around 130 m. It is worth noting that some echoes remain above the boundary layer after sunset. These are believed to be diminishing turbulence in the residual layer.

Tower wind speed measurements, shown in Figure 2.8b, have periodic variation throughout the day. It appears that the sharp changes in wind speed may be related to the convective thermals. Near sunset, when the boundary layer collapses (1800 LT), wind speed diminishes, as does the variation in wind speed.

The temperature time series (Figure 2.8c) shows a typical diurnal variation where little cloud cover exists. Temperature decreases through the night, reaches a minimum at 0615 LT and then increases in response to surface heating, reaching a maximum in the afternoon and then decreases just before sunset. The wind direction shows more variability during the day compared to the evening and nighttime periods.

The miniSODAR horizontal wind speed profile is shown in Figure 2.9a. During stable conditions, light winds at the surface increase quickly with height to the top of the SBL. It is noticed that a wind speed maximum exists, presumably a nocturnal jet, near where the DFS analysis indicates the SBL height (100 m). During boundary layer growth, in the morning, this momentum is quickly mixed and the wind speed becomes nearly constant with height. When the boundary layer collapses during the late afternoon, the wind speed becomes light near the surface increasing again with height to the top of the SBL where another nocturnal jet is formed at around 130 m. Figure 2.9b shows the vertical velocity for this same convective case. At night the vertical velocity is near zero close to the surface with slightly higher values (~ 0.25 to -0.25 m s^{-1}) and more variation

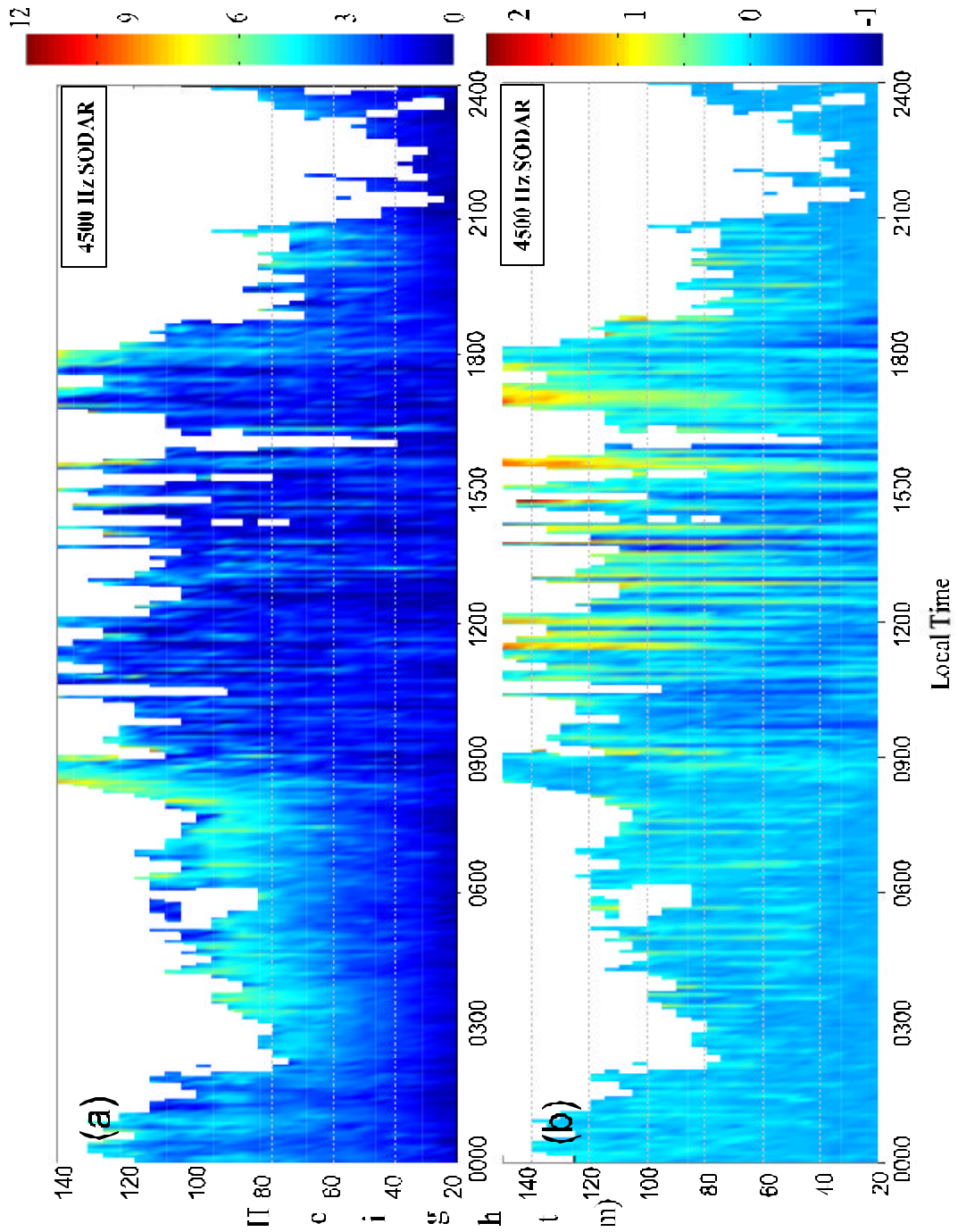


Figure 2.9 Velocity profile data from the Model 4000 miniSODAR on September 08, 2000. (a) Horizontal wind speed ($\text{m}\cdot\text{s}^{-1}$), colors correspond to colorbar to the right of the panel. (b) Vertical velocity ($\text{m}\cdot\text{s}^{-1}$) for the same time period.

above the surface near the top of the stable boundary layer. During the day when the boundary layer is convective, the variation in vertical velocity is high. Strong upward

motion ($0.5-1.5 \text{ m s}^{-1}$) corresponds to the periodic thermals, followed by periods of weak decent (-0.5 m s^{-1}).

2.4 SUMMARY

The main emphasis of this chapter is to compare and contrast boundary layer observations from the instrument cluster during two typical meteorological conditions. The presented observational analysis does show a significant difference between the two cases. The near-neutral case showed that the boundary layer properties remained relatively constant during the 24-hour observational period. The SODAR reflectivity indicated that the surface boundary layer height remained around 100 m in which the echoes were strong and nearly uniform. The stability, implied from the 10-2 m temperature difference, supports a near-neutral boundary layer.

Conversely, the convective case showed a quickly increasing boundary layer in the early morning, just after sunrise. Strong intermittent reflectivity hints towards convective thermals while the temperature gradient showed strong buoyant instability. A well-defined stable nocturnal boundary layer was seen in this same case, while not in the neutral case. The nocturnal boundary layer height is well determined by the SODAR. Overall, the combination of instruments provides good information on the boundary layer structure and detailed information on the wind field. Observations from this system will be used in the following chapters to compare with model-simulated fields.

Chapter 3

ADVANCE REGIONAL PREDICTION SYSTEM (ARPS)

ARPS is the model elected for the mesoscale meteorological simulations and coupling with the CALPUFF dispersion model. In this chapter, information on ARPS, how it was used and configured is discussed. These details include general model characteristics, parameterizations employed and the land-surface as well as the turbulent flux numerical schemes. In addition to the ARPS details, a discussion is included on how the model data was used for CALPUFF. A brief discussion on the surface data used to validate the model performance is also included.

3.1 OVERVIEW OF THE ARPS MODELING SYSTEM

ARPS is a mesoscale meteorological model developed by the Center for Analysis and Prediction of Storms (CAPS); a group formed at the University of Oklahoma in 1989 with funding from the National Science Foundation (NSF). Their objective was to develop a mesoscale meteorological model that will be capable of modeling storm scale weather phenomena for a range of uses including both research and operational interests. A major reason why ARPS was elected for this research is its advanced physical and numerical schemes. The FORTRAN code of ARPS is packaged for most computational platforms and organized so that realistic domains and simulations can be accomplished. It also contains options to simulate idealized cases, most typically used in research applications. Included within this packaged code are preprocessing and post processing programs to create terrain, landuse characterization, external boundary conditions as well

as a number of output formats for various popular environmental visualization software (Grads, Vis-5D, etc). In addition to these features, the ARPS model contains a preprocessing code to assimilate a variety of observations including atypical WSR-88D radar, wind profiler and satellite data.

ARPS is a non-hydrostatic, fully compressible primitive equation model appropriate for scales ranging from meters to kilometers (Xue et. al. 1995). The vertical coordinate system is a generalized terrain following coordinate with options for stretched or equal spacing while the horizontal grid spacing is equal in both the x and y directions. Additional grid options are included for 1-D, 2-D or 3-D simulations. Prognostic variables include 3-D wind components, potential temperature, pressure, sub-grid scale TKE and moisture related variables (specific humidity, cloud water, cloud ice and even hail/graupel).

3.2 NUMERICAL DETAILS

3.2.1 INTEGRATION, SMOOTHING, TKE CLOSURE AND RADIATION

A variety of integration and numerical techniques are available but listed below are the options selected for these experiments. Time integration for the model simulations is split into large and small time steps. The small time step is used to compute acoustically active terms such as pressure and vertical velocity perturbations. A fully implicit scheme is used for this integration, which allows computational stability constraints to limit only the large time step. All other variables are forecasted using a large time step with a fully explicit, three-level, leapfrog method with Asselin time filter

option. Spatial derivatives are estimated using 2nd order accurate finite difference except for advection terms, which are 4th order accurate. Computational smoothing is employed so that numerical noise is dampened. In these simulations a 4th order mixing coefficient is used in both the vertical and horizontal direction.

Turbulence closure was realized through 1.5-order TKE turbulence closure following the non-local scheme of Sun and Chang (1986). In this scheme a budget equation for subgrid scale TKE is solved which includes buoyancy, shear production, advection (diffusion and transport) and viscous dissipation. Moist processes are explicitly considered along with the Kain and Fritsch cumulus parameterization (Kain and Fritsch, 1993). Radiation physics are simulated using atmospheric radiation transfer parameterization developed at NASA/Goddard Space Flight Center and tailored for ARPS. This scheme includes equations for both short wave (Chou, 1990; Chou, 1992) and long wave (Chou and Suarez, 1994) radiation processes. Additional details related to the formulations can be found in Xue et al. (1995), Xue et. al. (2000) and Xue et. al. (2001).

3.2.2 SURFACE FLUXES AND LAND-SURFACE MODEL

The more important properties of ARPS, in regards to the type of small-scale modeling of interest in this study, are the boundary layer parameterization, surface flux determination and surface energy and moisture evaluation. The following will outline how the ARPS model approximates the interaction between the earth's surface and the atmosphere.

ARPS uses surface roughness and a stability dependent surface flux model first developed by Businger et. al. (1971) then modified by Deardorff (1972b), in order to account for extremely stable and unstable situations. The surface fluxes considered are: momentum (Eq. 3.1 and 3.2), heat (Eq. 3.3) and moisture (Eq. 3.4). The stability dependent drag coefficient of momentum (C_d) along with the first level (10 m) wind speed (V) and wind components (u, v) are used to calculate the momentum flux. Similarly, the heat flux is calculated using the stability dependent drag coefficient of heat (C_h), first level wind speed and the temperature difference ($q - q_s$) between the ground and first level (10 m) above the surface. The same method is used for the moisture flux with the difference in specific humidity ($q - q_s$) and a drag coefficient for moisture exchange (C_q).

$$\overline{u'w'} = -C_d \overline{V} u \quad (3.1)$$

$$\overline{v'w'} = -C_d \overline{V} v \quad (3.2)$$

$$\overline{w'q'} = -C_h \overline{V} (q - q_s) \quad (3.3)$$

$$\overline{w'q'} = -C_q \overline{V} (q - q_s) \quad (3.4)$$

The Deardorff scheme first determines the stability near the surface. Stability is determined using the bulk Richardson number (Ri_b), which follows the form of Eq. 3.5. Once the stability is assessed the drag coefficients are then calculated according to whether the surface layer is stable, neutral or unstable. For unstable conditions the stability dependent drag coefficients of momentum and heat take the form outlined in Eq. 3.6 and Eq 3.7, where y_m and y_h are calculated (Eq. 3.8 and 3.9, respectively) according to Byun (1990). The surface roughness (z_o) is derived in accordance with Oke (1978)

from the 14 categorized vegetation type assigned by the world ecosystem class data (Kineman and Ohrenschaal, 1992).

$$Ri_b = \frac{g}{q_0} \frac{\Delta q(z-z_0)}{U^2} \quad (3.5)$$

$$C_d = \frac{k^2}{[\ln(\frac{z}{z_0}) - y_m(\frac{z}{L}, \frac{z_0}{L})]^2} \quad (3.6)$$

$$C_h = \frac{k^2}{[\ln(\frac{z}{z_0}) - y_m(\frac{z}{L}, \frac{z_0}{L})][Pr_0(\ln(\frac{z}{z_0}) - y_h(\frac{z}{L}, \frac{z_0}{L}))]} \quad (3.7)$$

$$y_m = 2\ln[(1+c)(1+c_0)^{-1}] + \ln[(1+c^2)(1+c_0^2)^{-1}] - 2\tan^{-1} c + 2\tan^{-1} c_0 \quad (3.8)$$

$$y_h = 2\ln[(1+h)(1+h_0)^{-1}] \quad (3.9)$$

During neutral stability conditions the exchange coefficients are calculated using the same equations with an extremely small, negative bulk Richardson number. When the stability is exceedingly unstable or free convective, Deardorff's (1972b) method uses the minimum of the unstable calculated value or double the neutral value. Similarly, the exchange coefficient of heat is determined during convective conditions as the minimum of the unstable calculated value or 3.33 times the neutral value. Stable situations are treated different but also take after Deardorff (1972b). The general idea is to scale the neutral values of both the heat and momentum drag coefficient by $\left(1 - \frac{Ri_b}{Ri_c}\right)$. Where Ri_c is the critical bulk Richardson number taken as 3.05.

Important to the stability determination and the heat and moisture fluxes is the soil state. The soil-vegetation model from Noilhan and Planton (1989) is employed by ARPS to predict how the soil temperature, moisture and canopy moisture varies spatially and temporally. The following five equations show how these calculations are executed. Eq. 3.10 relates the change in surface temperature, defined as the upper 10 cm, to ground heat flux ($R_n - H - LE$), thermal properties of the soil (C_t) and the temperature of the soil layer below (T_2). Eq. 3.11 solves the change in deep soil temperature as a function of the soil temperature above. Near surface soil moisture (W_g) changes are defined (Eq. 3.12) as a function of precipitation reaching the ground and dew formation (P_g), direct evaporation (E_g), flow to lower soil levels ($W_g - W_{geq}$) and runoff (R_g). Coefficients C_1 and C_2 are dependent on the soil type, saturation and layer depth.

$$\frac{\partial T_s}{\partial t} = C_t (R_n - H - LE) - \frac{2p}{t} (T_s - T_2) \quad (3.10)$$

$$\frac{\partial T_2}{\partial t} = \frac{1}{t} (T_s - T_2) \quad (3.11)$$

$$\frac{\partial W_g}{\partial t} = \frac{C_1}{r_w d_1} (P_g - E_g) - \frac{C_2}{t} (W_g - W_{geq}) - R_g \quad (3.12)$$

$$\frac{\partial W_2}{\partial t} = \frac{1}{r_w d_2} (P_g - E_g - E_{tr}) \quad (3.13)$$

$$\frac{\partial W_r}{\partial t} = (veg)P - E_r \quad (3.14)$$

Eq. 3.13 is for the time dependent change in deep soil moisture (W_2) is similar in form, influenced by precipitation (P_g), evaporation (E_g), transpiration (E_{tr}) and layer depth

(d_2). Canopy moisture (W_r) is also solved as a function of vegetation percentage (veg), precipitation (P) and canopy evaporation (E_g) as shown by Eq. 3.14.

Important to many of the land-surface calculations is the classification of the surface. ARPS defines the surface by the following parameters: soil type, vegetation type, vegetation fraction (veg), leaf-area index (LAI) and surface roughness (z_o). Soil types are specified with different thermal and moisture retention properties. These directly influence the heating/cooling rate of the surface. The soil type classification includes 13 categories and comes from the State Soil Geographic (STATSGO) archive (NSSC, 1994). Vegetation percentage becomes an important factor in determining the bulk thermal coefficient (C_t) of the surface, which includes the effect of both the soil and vegetation thermal properties. The vegetation percentage is derived from the Normalized Difference Vegetation Index (NDVI) corresponding to satellite observations (Kidwell, 1990). Equations 3.15 and 3.16 outline this approach, where C_v is a constant thermal coefficient of vegetation, C_g is the thermal coefficient for the soil type and C_{gsat} is the same for the soil when saturated.

$$C_t = \frac{1}{\frac{1-veg}{C_g} + \frac{veg}{C_v}} \quad (3.15)$$

$$C_g = C_{gsat} \left(\frac{W_{sat}}{W_2} \right)^{b(2\ln 10)} \quad (3.16)$$

Evaporation from the surface (E_g), vegetation transpiration (E_{tr}) and the plant canopy (E_r) is also dependent on the vegetation fraction. Latent heat flux (LE) is taken as

a sum of these processes (Eq. 3.17). Equations for the various evaporation parameters used in the model are outlined in Eq. 3.18 to 3.20.

$$LE = L_e(E_g + E_{tr} + E_r) \quad (3.17)$$

$$E_g = (1 - veg) \mathbf{r}_a C_q \bar{V} [h_u q_{vsat}(T_s) - q_{va}] \quad (3.18)$$

$$E_{tr} = veg \mathbf{r}_a \frac{1 - F_w}{R_a + R_s} [q_{vsat}(T_s) - q_{va}] \quad (3.19)$$

$$E_r = veg \mathbf{r}_a \frac{F_w}{R_a} [q_{vsat}(T_s) - q_{va}] \quad (3.20)$$

Leaf area index is another important surface characteristic in terms of the influence on evaporative and radiative processes. LAI is involved in calculating the resistance of the surface to evapotranspiration, which is defined by R_s (Eq 3.21). The LAI is derived from the same NDVI database as the vegetation percentage. For further clarification, the ARPS Users Guide gives in depth details on how some of the unexplained coefficients are estimated.

$$R_s = \frac{R_{smin}}{LAI(F_1 F_2 F_3 F_4)} \quad (3.21)$$

3.3 INITIALIZATION AND BOUNDARY CONDITIONS

Initialization and boundary conditions are among the most important aspects of a good numerical simulation. ARPS is a very flexible model in terms of initial conditions and boundary conditions. Options are embedded to define an idealized initial state including: constant static stability, constant potential temperature or even a single

sounding. These options allow for idealized simulations including density currents (Xue et. al., 1998), storm cells, and seabreeze fronts (Gilliam et. al., 2001). Other options allow ARPS to be initialized using more realistic data from many of the available operational models including Aviation Model (AVN), ETA, Rapid Update Cycle (RUC), ARPS and COAMPS data. This research takes advantage of both the idealized single sounding initialization and the realistic initialization using the 32 km ARPS model analysis provided by the CAPS group.

Boundary conditions (BC) are necessary for all limited domain models. In ARPS, five options are available for lateral boundary conditions. These include wall BC, periodic BC, zero gradient BC, open (radiative) BC and external BC from another model. In this study, the zero gradient BC was used for the seabreeze simulation over the Mumbai, India region. This option involves setting the outer grid point values equal to the adjacent inner grid point. For the realistic 6km simulations over Eastern North Carolina, external boundary conditions were provided by and extracted from the ARPS Data Assimilation System (ADAS). For the 1-km simulations over Raleigh, the 6-km simulation provides initialization and boundary conditions. An ARPS preprocessing program *ext2arps* extracts the values of the prognostic variable at specified time intervals for the outer edges of the grid domain. A linear interpolation is performed between the extracted time periods so that boundary condition values are available for each time step. For more details on the specifics of these numerical methods, refer to the ARPS Users Guide.

3.4 COUPLING ARPS WITH CALPUFF

In order to successfully couple ARPS with CALPUFF several boundary layer properties need to be either extracted or calculated from the simulated meteorology. The meteorological fields required by CALPUFF are wind components (u, v, w), potential temperature at all levels, friction velocity, Monin-Obukhov length, convective velocity scale and mixing height. ARPS standard output directly provides some of these meteorological parameters but several were derived. Variables such as the wind, potential temperature and friction velocity were directly extracted; however, the boundary layer height, Monin-Obukhov length and convective velocity scale were either diagnosed or calculated using other available variables. A conversion program in FORTRAN was written to convert the hourly ARPS output and derive unavailable variables, into a format appropriate for CALPUFF.

Mixing height was calculated using the turbulent kinetic energy (TKE) profile. Stull (1988) provides several well-known methods for determining the height of the planetary boundary layer (PBL). By definition, the PBL is the layer affected by the earth's surface and hence, a turbulent layer. Vertical TKE distribution, in theory, describes the extent of the PBL. The PBL height needed by CALPUFF is derived from ARPS as the height where the TKE drops to less than 5% of the maximum value in the boundary layer (Stull, 1988). The diagnostic algorithm looks at the simulated TKE profile, finds the maximum value in the boundary layer for each grid cell and then finds the height where this maximum value decreases to 5%. Using the analyzed mixing height (z_i), surface kinematic heat flux ($\overline{w'q_v'}$) and surface virtual potential temperature (q_v); the convective velocity scale (w_*) is calculated according to Arya (2001) as in Eq. 3.22. Next, the

convective velocity scale, friction velocity (u_*) and potential temperature are used to calculate the Monin-Obukhov length (L) according to Stull (1988) as in Eq. 3.23.

$$w_* = \left[\frac{gz_i}{\mathbf{q}_v} \left(\overline{w' \mathbf{q}_v'} \right)_s \right]^{1/3} \quad (3.22)$$

$$L = - \frac{u_*^3}{k \frac{g}{\mathbf{q}_v} \left(\overline{w' \mathbf{q}_v'} \right)_s} \quad (3.23)$$

3.5 SURFACE OBSERVATIONS

Validation using observations is important to assess the accuracy of any model simulation. In this study, for the regional simulation over eastern North Carolina, a number of observations were available to compare with the ARPS model simulations. Chapter 2 describes in detail the two SODAR's and micrometeorological tower. In addition to these, eleven North Carolina Environmental and Climate Observing Network (NC ECONet) stations are used to compare 2 m temperature, 10 m wind speed and direction with the model simulated values. Model values from the closest grid points to the eleven surface stations are used for the comparison with the observations. Figure 3.1 shows the location of these stations with respect to the 6-km eastern North Carolina model domain. The hourly data from this network of surface stations is archived as the average over the previous hour. It must be stated that there are inherent differences between the simulated and observed data. For one, the simulated meteorology from ARPS is not averaged over an hour but the value at that specific time. Secondly, the model

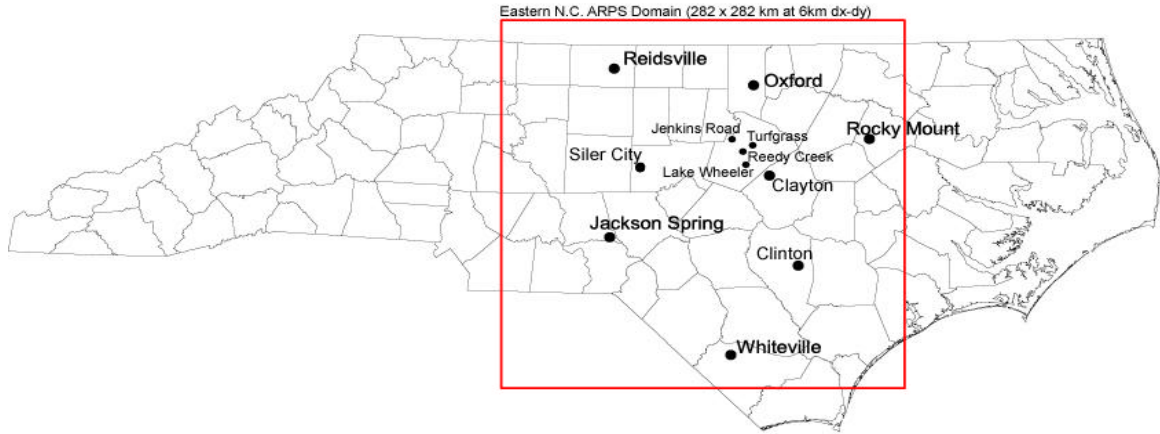


Figure 3.1 Regional view of North Carolina and the location of the 6 km ARPS model domain. Surface station (NC ECO Net) locations are depicted.

prediction for a variable like wind speed at a specific grid point, is a volume average not a point measurement like observations. For this reason, the comparison between observed and predicted variables should not be exact but have differences, which are a function of using finite-difference methods to solve fluid motion equations. However, the comparison should yield similarities in both magnitude and trend. The simulated and observed data will be compared using both time series plots over the simulation period and a more quantitative analysis using typical model performance statistics.

Model performance statistics provide more tangible verification of forecast accuracy. For the two simulations presented in this thesis (Chapter 6 and 7), model bias (MBE), variance (VAR), root mean square error (RMSE), mean average error (MAE) and index of agreement (IOA) are calculated using time series observation from the NC ECO Net and the model prediction. The mean model bias error is simply the average difference between the model prediction (P) and observed value (O) as shown by equation 3.24, where N is the number of data point in the time series. The variance, shown in Eq. 3.25

gives an idea of the distribution of differences between observed and predicted. Eq. 3.26 shows how the root mean square error is calculated. The mean average error is calculated according to Eq. 3.27 and Eq. 3.28 shows the index of agreement.

$$MBE = \frac{1}{N} \sum_{i=1}^N P_i - O_i \quad (3.24)$$

$$VAR = (N-1)^{-1} \sum_{i=1}^N (P_i - O_i - MBE)^2 \quad (3.25)$$

$$RMSE = \left[N^{-1} \sum_{i=1}^N (P_i - O_i)^2 \right]^{0.5} \quad (3.26)$$

$$MAE = N^{-1} \sum_{i=1}^N |P_i - O_i| \quad (3.27)$$

$$IOA = 1 - \left[\frac{\sum_{i=1}^N (P_i - O_i)^2}{\sum_{i=1}^N \left[(|P_i - \bar{O}|) + (|O_i - \bar{O}|) \right]^2} \right] \quad (3.28)$$

CHAPTER 4

CALPUFF MODELING SYSTEM

In this chapter some details of the CALPUFF dispersion modeling system are given. These include information on how the dispersion coefficients are derived from the meteorological fields, various source types used in this study and some other model information.

4.1 BACKGROUND

It is generally recognized that CALPUFF, a non-steady state Gaussian plume model, out-performs many other available dispersion models including Industrial Source Complex 3 (ISC3) and Mesoscale Puff (MESOPUFF) (Allwine, Dabberdt, and Simmons, 1998). Simpler dispersion models only allow spatially constant conditions (steady state) and therefore, perform rather poorly during light wind and non-homogeneous conditions. Many of these models also assume homogeneous and constant surface characteristics. Since most air quality problems occur during variable meteorological conditions, CALPUFF has potential to provide more accurate estimations of human exposure to environmental pollutants for any given representative meteorological conditions.

CALPUFF has many qualities that make it an attractive choice for modeling air pollution dispersion. Among the most important is the treatment of the boundary layer as spatially heterogeneous. Consideration is given for the variations in the stability, mixing height and wind speed and direction as a puff or tracked plume is transported within the domain.

Of most important in terms of dispersion, is the stability of the boundary layer. The stability directly relates to both horizontal and vertical diffusion or how quickly a puff of material grows. Diffusion is explicitly described by the dispersion coefficients (σ_y and σ_z). The CALPUFF system allows the user a variety of methods to determine σ_y and σ_z . Among these techniques are: direct measurements of the horizontal and vertical velocity variances, Pasquill-Gifford (PG) dispersion coefficients (related to stability categories), CTDM dispersion coefficients (neutral/stable) and estimated values derived from observed or computed micrometeorological variables. In this research dispersion coefficients are derived from micrometeorological variables including friction velocity (u_*), convective velocity scale (w_*) and Monin-Obukov length (L). With these variables a set of equations is used to estimate the velocity variances, which are ultimately responsible for lateral and vertical puff diffusion. The following outlines how these parameters are derived from the simulated meteorological fields.

4.2 DISPERSION FORMULATION

Starting with the time dependent dispersion coefficient equation, Hanna et. al., (1977) provided the basic equations (Eq. 4.1 and 4.2) for the puff growth with time due to atmospheric turbulence.

$$\mathbf{s}_{yt} = \mathbf{s}_v f_y \left(\frac{t}{t_{ty}} \right) \quad (4.1)$$

$$\mathbf{s}_{zt} = \mathbf{s}_w f_z \left(\frac{t}{t_{tz}} \right) \quad (4.2)$$

The main independent variables in these equations are the horizontal and vertical velocity standard deviations (σ_v and σ_w). The dimensionless f_y and f_z time functions are taken from Draxler (1976) and shown by equations 4.3, 4.4 and 4.5 where (t) is travel time in seconds.

$$f_y = \left[1 + 0.9 \left(\frac{t}{1000} \right)^5 \right]^{-1} \quad \text{All stability } (-8 < L < 8) \quad (4.3)$$

$$f_z = \left[1 + 0.9 \left(\frac{t}{500} \right)^5 \right]^{-1} \quad \text{Convective } (L < 0) \quad (4.4)$$

$$f_z = \left[1 + 0.945 \left(\frac{t}{100} \right)^{806} \right]^{-1} \quad \text{Stable } (L > 0) \quad (4.5)$$

In order to determine velocity standard deviations under convective conditions, the boundary layer is divided into three main zones: surface layer, mixed layer and entrainment layer. Weil (1985) defines these three zones as a function of the boundary layer height. The surface layer is defined as the layer below $(0.1)z_i$, mixed layer is between the surface layer and $(0.8)z_i$ and the entrainment layer is above the mixed layer to the boundary layer height (z_i). The standard deviations are calculated using different equations for each boundary layer zone and for different stability conditions. Panofsky et. al. (1977) related the surface layer standard deviation of velocity for convective conditions as follows in Eq. 4.6 and 4.7. For the mixed layer, these turbulence variables are calculated (Eq 4.8 and 4.9) using suggestion from Hicks (1985).

$$\sigma_v = u_* \left[4 + 0.6 \left(-z_i / L \right)^{2/3} \right]^{1/2} \quad (4.6)$$

$$\sigma_w = u_* \left[1.6 + 2.9 \left(-z / L \right)^{2/3} \right]^{1/2} \quad (4.7)$$

$$\sigma_v = \left(3.6u_*^2 + 0.35w_*^2 \right)^{1/2} \quad (4.8)$$

$$\mathbf{s}_w = \left(1.2u_*^2 + 0.35w_*^2\right)^{1/2} \quad (4.9)$$

When the boundary layer is in a neutral state, Eq. 4.10 and 4.11 are used to calculate the monotonically decreasing velocity variation in the boundary layer (Arya, 1984).

$$\mathbf{s}_v = 1.8 \exp\left(-0.9 \frac{z}{z_i}\right) \quad (4.10)$$

$$\mathbf{s}_w = 1.3 \exp\left(-0.9 \frac{z}{z_i}\right) \quad (4.11)$$

Stable conditions are treated differently by CALPUFF. When the boundary layer is stable, the similarity scaling proposed by Nieuwstadt (1984) is utilized to determine the velocity variance. This similarity theory states that the vertical and horizontal velocity standard deviations normalized by the local friction velocity (u_{*l}) have constant values. Equations 4.12 through 4.14 outline how these are computed.

$$\frac{\mathbf{s}_v}{u_{*l}} = 1.6 \quad (4.12)$$

$$\frac{\mathbf{s}_w}{u_{*l}} = 1.3 \quad (4.13)$$

$$u_{*l} = u_* \left(1 - \frac{z}{h}\right)^{\frac{3}{4}} \quad (4.14)$$

In the following chapters two separate dispersion simulations are conducted. The first set of simulations (Chapter 5) involves simple point sources placed at different locations within the domain. The main reasons for keeping this simulation simple is two fold. It is the first test case of the coupled ARPS-CALPUFF system with the objective

being to make sure that the coupling program is providing CALPUFF with the correct ARPS simulated meteorological fields and also to see if the concentration distribution is consistent with the simulated meteorology.

This preliminary dispersion simulation will be carried one step further in the next case (Chapter 7). For one, the meteorology and the surface characteristics will more realistic, being initialized with assimilated data, provided realistic external boundary conditions and USGS landuse and terrain data. Further adding to realism, actual roadways are specified as line sources; the source strength of these roadways is derived from an emissions model and the source strength is diurnally variable as a result of traffic patterns for the region. Specific information for these sources is introduced in the following chapters. For information on the detailed numerical equations used by CALPUFF refer to the CALPUFF Users Manual Version 5.0 (Scire et. al., 2000).

CHAPTER 5

TROPICAL SEABREEZE CIRCULATION: INFLUENCE ON POLLUTION DISPERSION.

5.1 INTRODUCTION

The seabreeze circulation is a mesoscale feature that has a clear influence on the both the temporal and spatial dispersion qualities of the coastal boundary layer. As the land heats up during the daytime, the water temperature remains essentially constant. Because of this, strong surface temperature and related heat flux gradients form at the land-sea interface. This strong horizontal flux gradient induces the seabreeze, a thermally direct circulation, consisting of low-level onshore flow (seabreeze) and a return flow aloft directed offshore (Atkins and Wakimoto, 1997). The thermal internal boundary layer is a product of the seabreeze and acts to modify the boundary layer structure over the region that it passes. As a result, the atmospheric dispersion within this layer can be much different than the dispersion inland and offshore (Lyons, 1975; Stunder et. al., 1985; Kitada and Ueda, 1989; Rhome et. al., 2001).

The ARPS (Advanced Regional Prediction System) mesoscale meteorological model, developed by the University of Oklahoma, is used to examine the land-sea induced circulation properties along the west India coastline. Using ARPS meteorology, simple dispersion simulations are carried out by means of the CALPUFF dispersion model. The purpose of these simulations is to examine the diurnal boundary layer structure along the land-sea interface and how it influences dispersion properties of the region. This includes both a spatial and temporal analysis of the potential temperature,

turbulent kinetic energy (TKE), and wind flow structure. These meteorological properties are related to the surface concentration distribution of NO_x as simulated by CALPUFF. The concentration distribution is examined at different locations in the model domain during different times of the day.

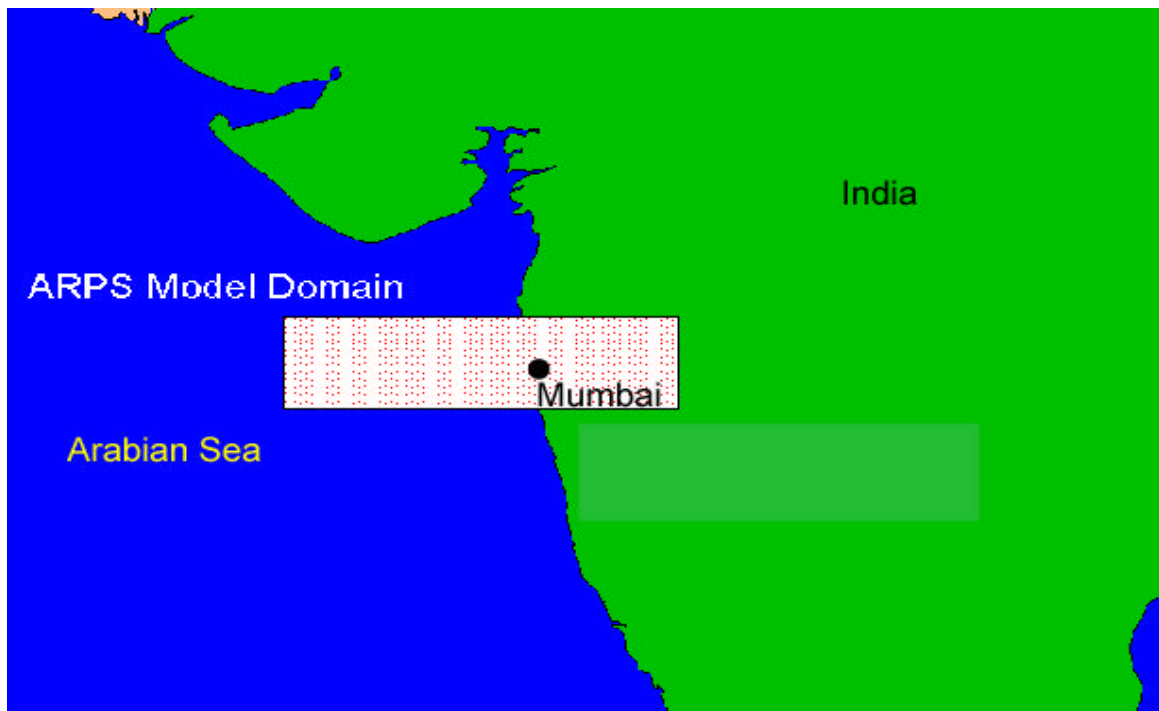


Figure 5.1 Plan view of the model domain with respect to India and the Arabian Sea.

5.2 EXPERIMENT DESIGN

ARPS is a non-hydrostatic, fully compressible primitive equation model (Xue et. al. 1995). The model grid for this simulation consisted of 100 x 25 horizontal grid cells with a horizontal grid spacing of 5 km. In Figure 5.1 a schematic of the model domain location is shown with respect to India, Mumbai and the Arabian Sea. Forty-three vertical layers are stretched from the surface to 13 km. Figure 5.2 shows the vertical grid point distribution. Almost half the grid points are below 2 km, providing good resolution

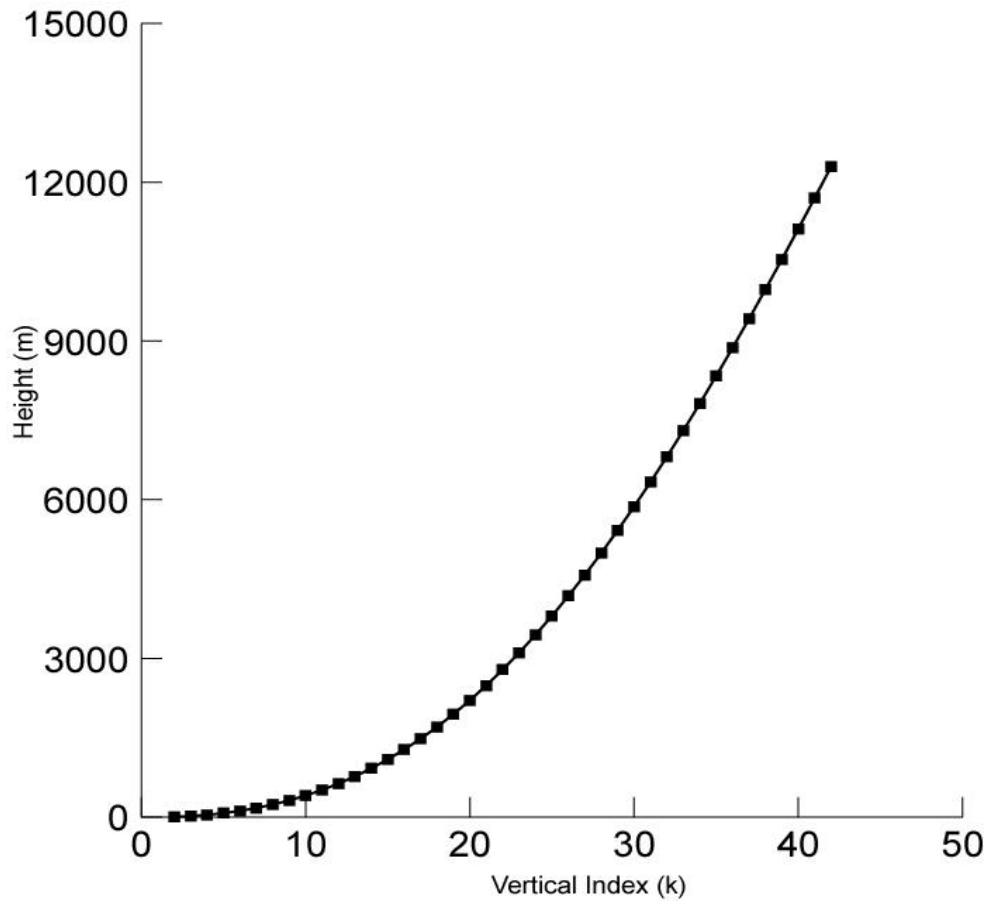


Figure 5.2 ARPS vertical coordinate distribution for the tropical seabreeze case.

in the boundary layer. The model was initialized with a single sounding, taken from the Mumbai Airport on February 24, 1999 at 0500 LT (00 UTC) and carried out for 48 hours. The results shown in this investigation are from the last 24-hour period of the model simulation (0500 LT Feb 25 - 0500 LT Feb 26).

The initial potential temperature and specific humidity profile was taken from Mumbai, India on February 24, 2000. Wind speed/direction was artificially provided to idealize the seabreeze simulation. The wind direction was set to 45° (Northeast). This direction roughly correlates with the mean flow over the region during the winter months,

typically referred to as the northeast monsoon season. The wind speed was set to a constant 5 m/s at all levels.

The soil model was initialized and the surface properties defined according to Table 5.1. All surface properties were characterized as horizontally homogeneous as well as the initial soil/sea-surface temperature and soil moisture.

Table 5.1 Soil properties and initializations values for seabreeze simulation over Mumbai, India.	
<u>Land</u>	
Soil type	Sandy loam
Roughness	0.20 m
Vegetation type	Field w/ Trees
Leaf-area index	2.0
Vegetation fraction	0.30
Initial sfc. temp.	293 K
Initial soil moisture	.20
<u>Ocean</u>	
Soil type	water
Roughness	0.001 m
Vegetation type	water
Leaf-area index	0
Vegetation fraction	0
Initial sfc. temp.	297 K

5.3 NUMERICAL MODEL RESULTS

5.3.1 ARPS METEOROLOGICAL SIMULATION

The ARPS simulation was conducted for a two-day period. The following discussion presents results from the second day of the simulation. Figure 5.3a and Figure 5.3b give the simulated X-Z cross-section of potential temperature and horizontal wind, perpendicular to the coastline at 0500 LT. Panel (a) shows the cross-section over the entire 500 km east-west distance of the model domain and to a height of 3000 m. Panel

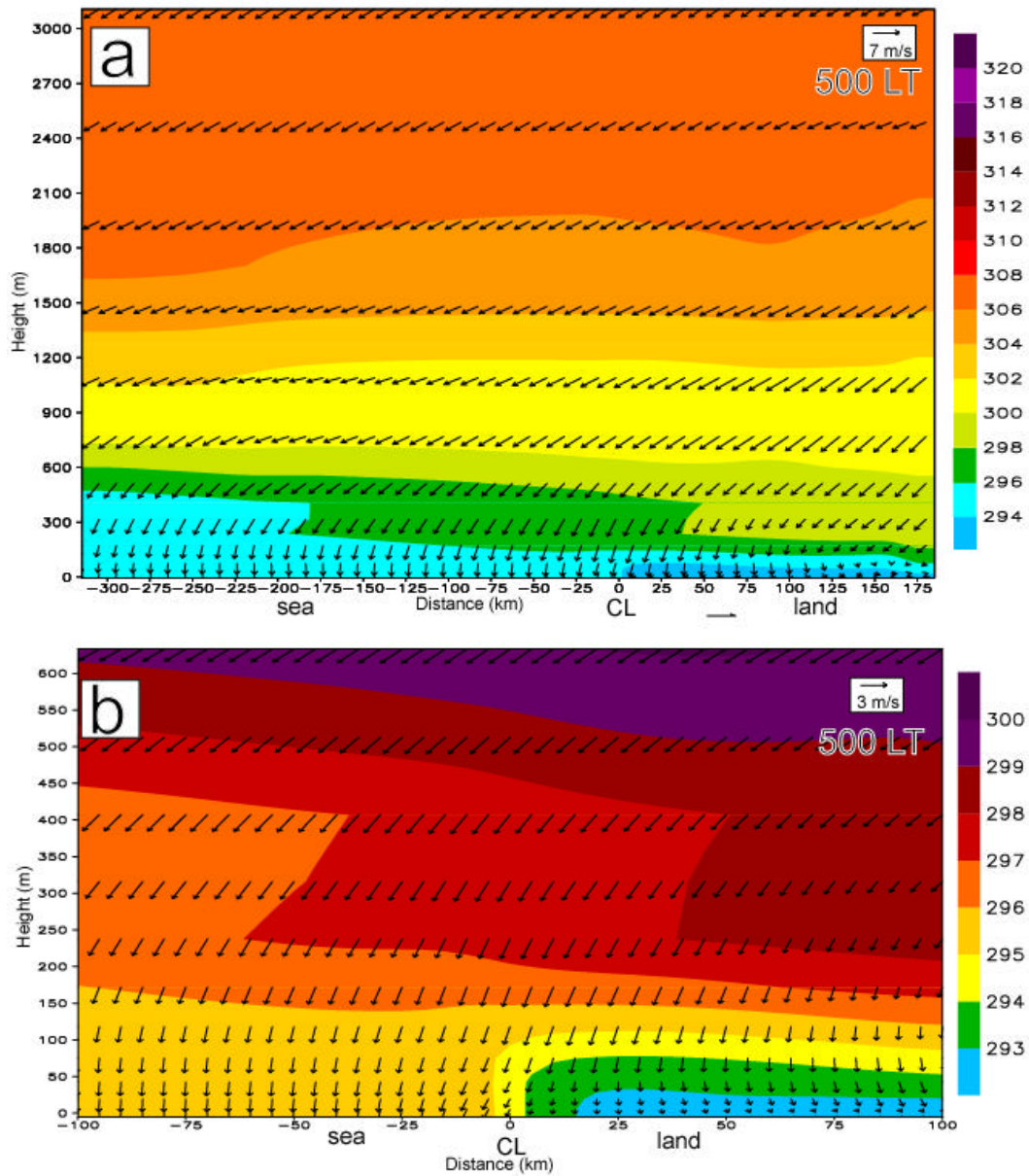


Figure 5.3 (a) X-Z cross-section of potential temperature and horizontal wind vectors at 500 LT, 24-hours from the model initialization. The x-axis is in kilometers with 0 km indicating the coastline (CL), negative distance is over the ocean. (b) Same cross-section as (a), but centered and magnified in on the land-sea interface.

(b) shows a magnified cross-section of Panel (a), for 100 km on either side of the coast and to a height of 600m. The large-scale wind direction, defined as the wind flow above the boundary layer, is from the northeast (Figure 5.3a).

Two distinct boundary layers, separated at the land-sea boundary (Figure 5.3b) are noticed. The marine boundary layer (MBL) is shown as the well-mixed layer extending from the sea surface to 150 m near the coast (Figure 5.3b) and up to 500 m further offshore (Figure 5.3a). Consistent with a well-mixed potential temperature, the wind speed and direction also remains the same with height in the MBL (Stull, 1989). The simulation shows that the MBL slopes upwards offshore of the land-sea interface. Observations taken during the INDOEX project support this MBL slope. The underlying cause is the increasing modification of continental air by the ocean surface as the air travels from land over the ocean.

A distinct stable boundary layer (SBL) over land is seen in the potential temperature profile, as a strong inversion exists 100 m above the surface. The height of the SBL is on the order 50 m away from the coastline (Figure 5.3b) and 100-200 m closer to the coast. A weak offshore acceleration in the wind is noted at the coastline, which slightly increases the boundary layer height. Inland the strong static stability has detached the surface from the synoptic-scale momentum leading to calm winds near the surface.

Figure 5.4a and 5.4b give the simulated potential temperature and horizontal wind profile at 1000 LT. At this time the solar radiation has begun to affect the boundary layer by heating the underlying surface. The MBL changes little while the warming land causes the boundary layer to begin a transition from stable to convective. The quickly growing convective boundary layer is approximately 600 m, shown by the constant potential temperature of 298 K and well mixed momentum. A sharp horizontal potential temperature gradient begins to develop at the land sea interface. It is this developing

temperature gradient that initiates the mesoscale seabreeze circulation (Simpson et. al. 1979).

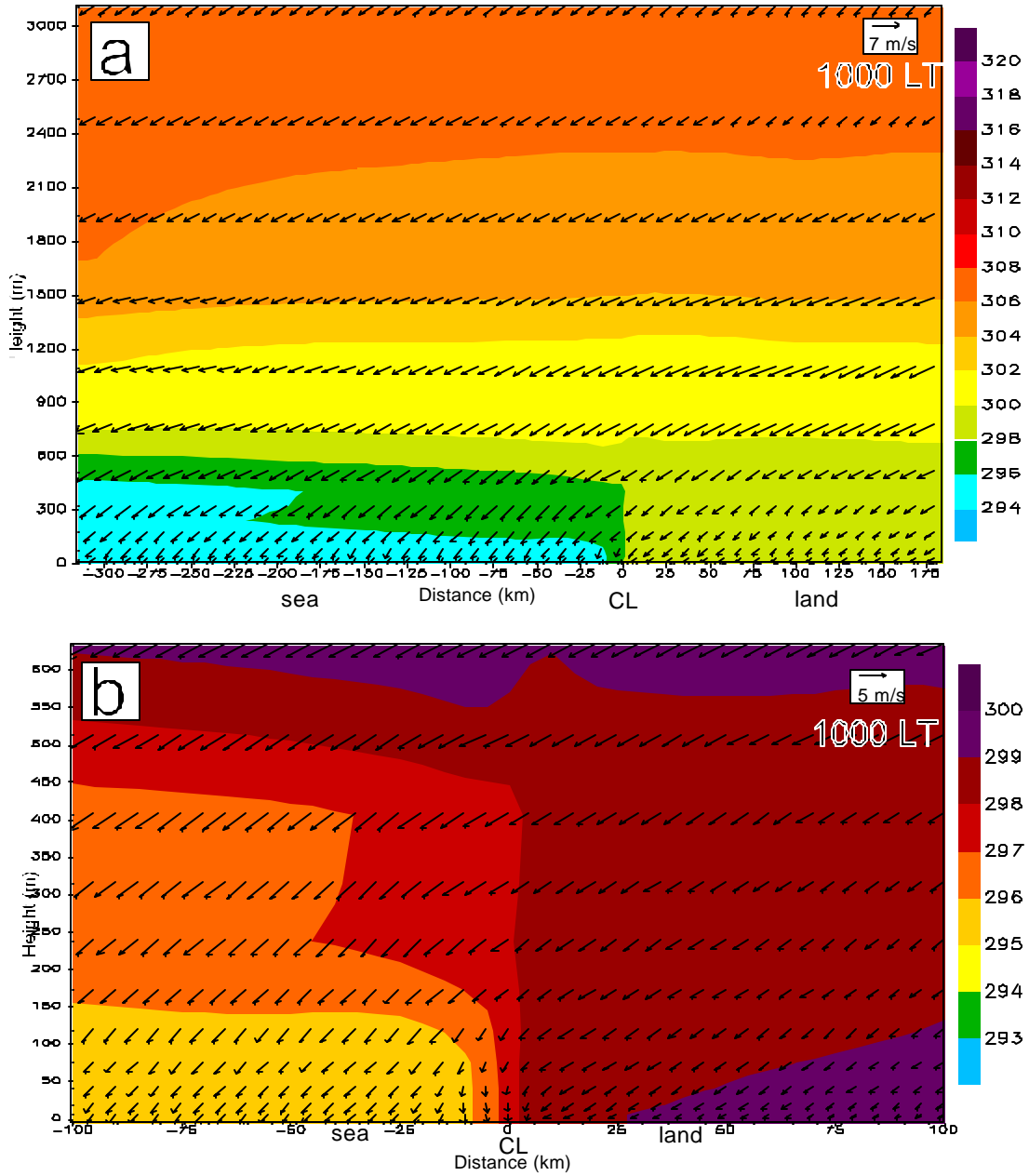


Figure 5.4 (a) X-Z cross-section of potential temperature and horizontal wind vectors at 1000 LT, 29-hours from the model initialization. The x axis is in kilometers with 0 km indicating the coastline (CL), negative distance is over the ocean. (b) Same cross-section as (a), but centered and magnified in on the land-sea interface.

The MBL at this time is well defined as a layer of constant potential temperature bounded by a sharp inversion. Close to the coast this layer is approximately 200 m deep while further offshore the marine layer is around 600 m. Similar as the previous time, the marine boundary layer slopes upward from the coast towards the waters further offshore.

Figure 5.5a and 5.5b show the simulated potential temperature and horizontal wind at 1400 LT. At this time the seabreeze circulation has fully developed. An onshore flow (northwest) exists from the surface to around 250 m, defining the seabreeze flow. Above the seabreeze flow the offshore flow accelerates, signifying the return flow aloft (300-1000 m). The horizontal extent of the seabreeze is also apparent in Figure 5.5b. A sharp boundary exists at about 15 km inland where the flow shifts from northwest to northeast, delineating the seabreeze front. Previous research (Raynor et. 1979; Atkins and Wakimoto 1991; Arritt 1993; Simpson et. al. 1995) suggests that during offshore synoptic events the seabreeze front remains close to shore as shown in this simulation. The seabreeze has progressed 10 km inland at this time. At approximately 75 km offshore the flow shifts from north-northwest to north-northeast; this indicates the offshore extent of the simulated seabreeze circulation.

Another good signature of the seabreeze is the density current structure; distinguished by the potential temperature profile in Figure 5.5a and 5.5b (Simpson 1979). A sharp horizontal temperature gradient has formed along the seabreeze front and is the driving mechanism behind the circulation. Ahead of the seabreeze front the convective boundary layer is seen as a thoroughly mixed layer up to 1800 m, just behind the seabreeze front the thermal internal boundary layer (TIBL) is observed. The TIBL is

marked by an inversion at about 100 m at the coastline, sloping upwards to about 200 m towards the seabreeze front.

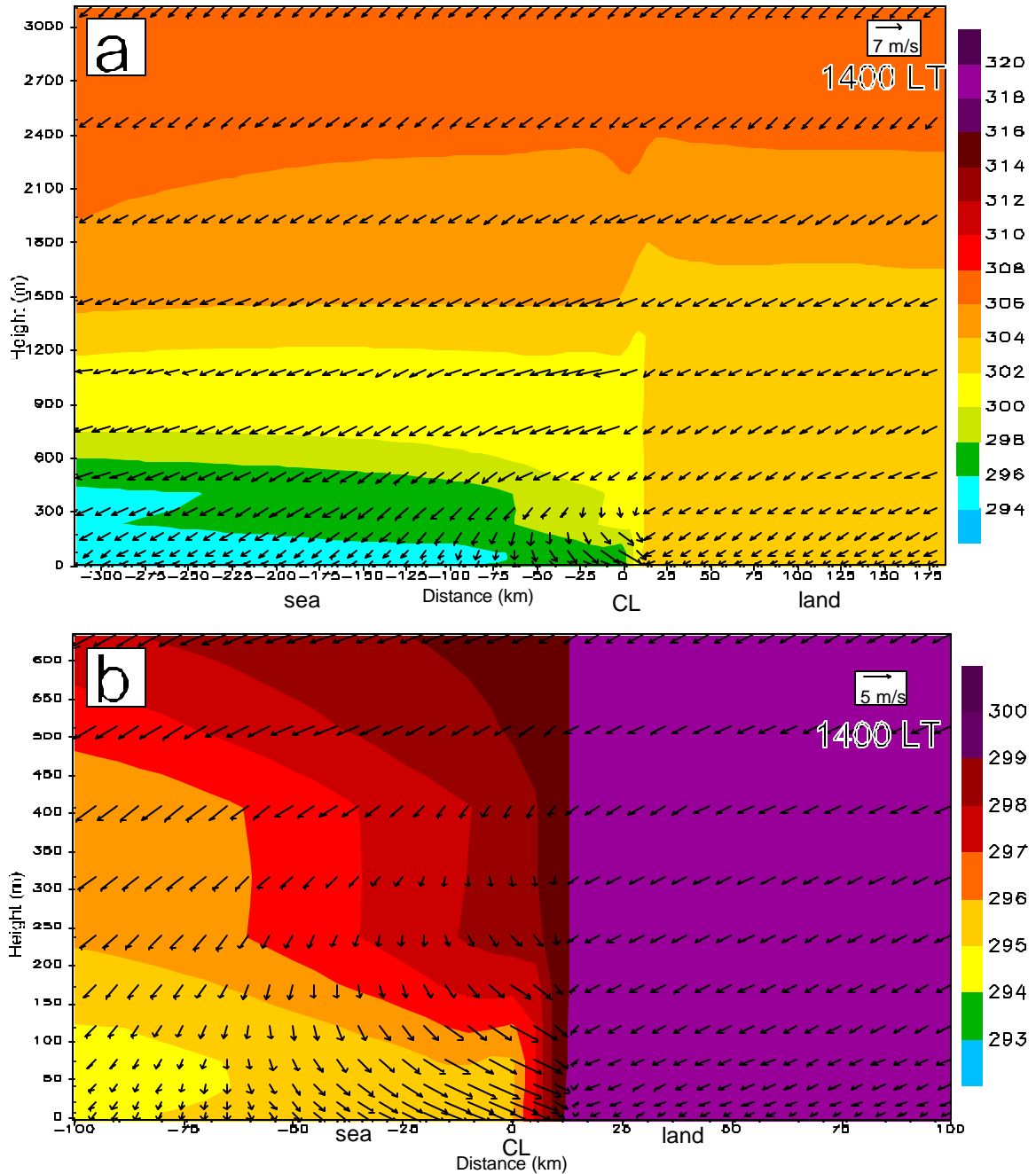


Figure 5.5 (a) X-Z cross-section of potential temperature and horizontal wind vectors at 1400 LT, 33-hours from the model initialization. The x axis is in kilometers with 0 km indicating the coastline (CL), negative distance is over the ocean. (b) Same cross-section as (a), but centered and magnified in on the land-sea interface.

The potential temperature and wind profile at 1900 LT are shown in Figure 5.6a and 5.6b. At this time the solar insolation is diminishing. The boundary layer begins a transition from convective to stable conditions as the surface begins to cool. It is seen that the near surface potential temperature lowers and stabilizes the surface layer. This stable stratification dampens the downward transfer of momentum from aloft to the surface, causing the surface winds to lighten. In addition, the buoyant and mechanical driven turbulence begins to dissipate. It is noticed that just above the surface, a well-mixed residual convective layer is present.

Near the coast, the seabreeze front has advanced 50 km inland as revealed in both the potential temperature and the wind distribution. Studies such as by Arritt (1993) have suggested that seabreeze fronts, during offshore flow regimes, will advance inland most rapidly in the early evening. The density current structure is still intact along and behind the front but it is becoming less defined. The low-level onshore wind is still noticed at the frontal boundary and the return flow aloft is still well established. The MBL adjacent to the coast is rather shallow (100 m), still sloping upwards away from the coast to about 600 m.

Turbulent kinetic energy (TKE) is an important property to examine when investigating how air dispersion is affected by the boundary layer. It provides a quantitative measure of mixing efficiency and, hence, the degree of diffusion of pollutants. In Figures 5.7 and 5.8, time-series profiles of TKE and potential temperature are shown at two locations in the model domain. These locations were chosen to illustrate how the boundary layer evolution is modified by the land-sea interface.

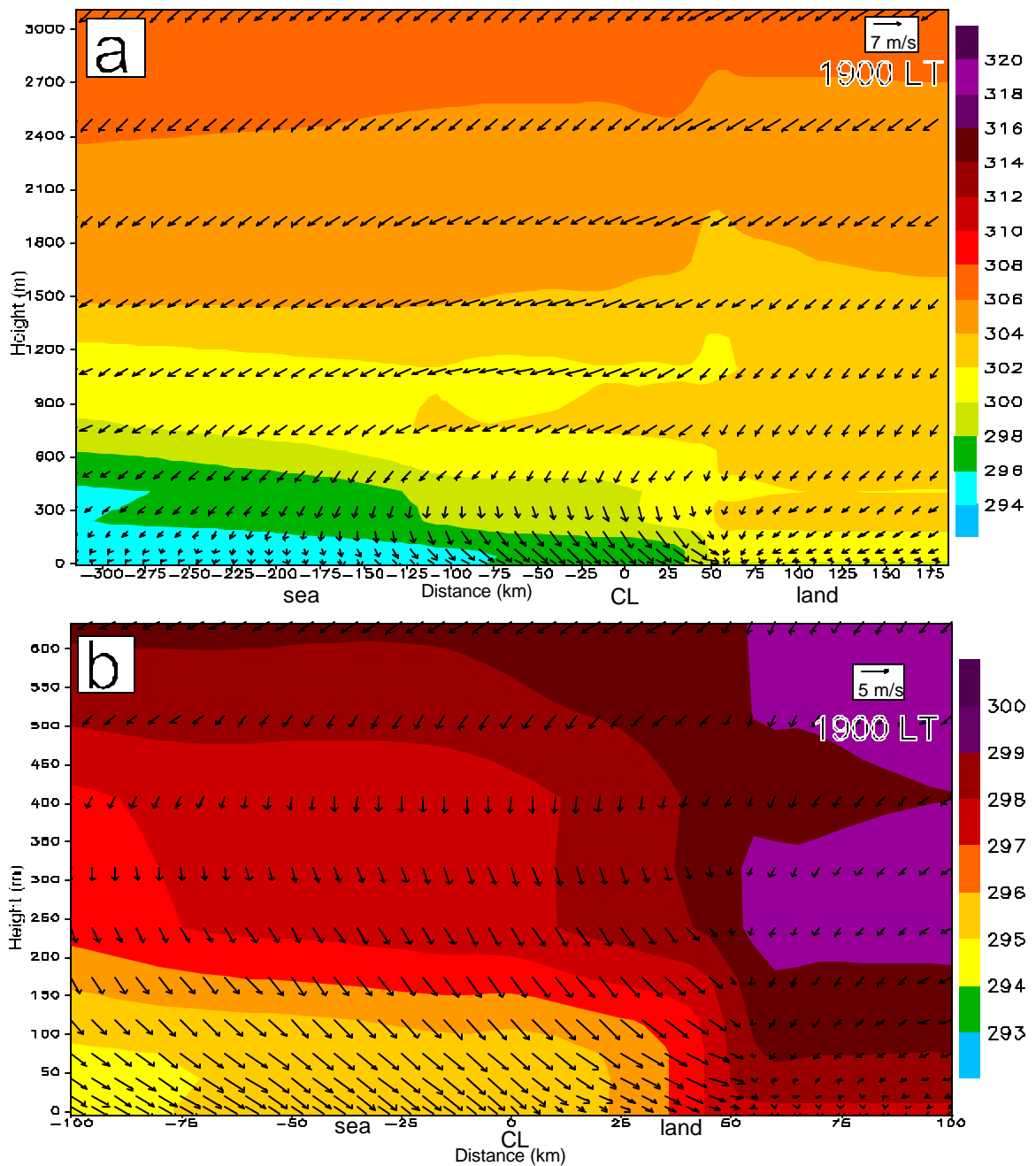


Figure 5.6 (a) X-Z cross-section of potential temperature and horizontal wind vectors at 1900 LT, 38-hours from the model initialization. The x axis is in kilometers with 0 km indicating the coastline (CL), negative distance is over the ocean. (b) Same cross-section as (a), but centered and magnified in on the land-sea interface.

Figure 5.7 represents the time-series profiles at a location 5 km inland. At 0500 LT the stable boundary layer is well represented by an increase in potential temperature

just above the surface (nocturnal inversion). It is estimated that the SBL height at this time is 50-100 m. Between 0700 LT and 0900 LT the boundary layer experiences slow but steady growth from 50 to 200 m. It is just after this time when explosive boundary layer growth occurs, increasing from 200 m to well over 1000 m between 0900 LT and 1200 LT. The TKE distribution during the growth period corresponds with increasing potential temperature and the convective boundary layer height. Maximum TKE occurs at approximately 1/3 rd the height of the boundary layer, which agrees with similarity theory and observations.

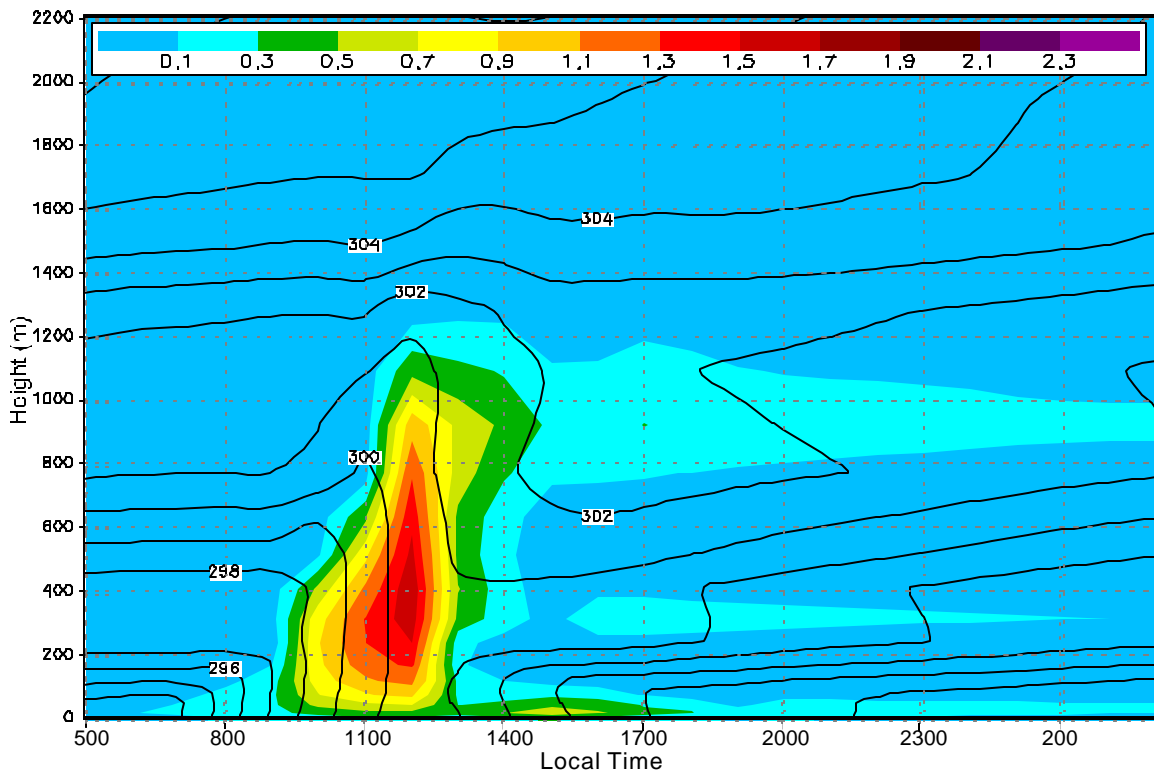


Figure 5.7 Time series profile of turbulent kinetic energy (TKE) and potential temperature at a location 5 km inland. Potential temperature is contoured each 1 degree and TKE (m^2/s^2) is shaded with legend shown.

At 1300 LT the seabreeze front passes over the profile location. A dramatic decrease in the boundary layer height from 1200 to 200 m is noticed at this time; a result

of sea-cooled air replacing the land-warmed air. Again, this signifies the passage of the thermal internal boundary layer; a product of the seabreeze. The proximity of the seabreeze front to the coast does not allow the onshore flow to warm. Therefore, the TIBL height is limited to approximately 200 m. It is noticed that the lapse rate below 100 m is super adiabatic; a result of sea-cooled air passing over warmer land. As a consequence, there is an area of higher turbulence very near the surface. When the sun angle lowers in the late afternoon (1700 LT) the surface begins to cool. As a result, the boundary layer height and turbulence near the surface decrease. After sunset the stable boundary layer is quickly established and gradually grows from less than 100 m to about 150 m through the night.

Figure 5.8 shows the time-series profiles of TKE and potential temperature at a location 100 km inland. This location was chosen to illustrate the temporal boundary layer structure with no seabreeze influence. The overall diurnal variation is similar to the previous example in Figure 5.7. During nighttime hours the boundary layer is stable with a low boundary layer height of a few hundred meters or less. The boundary layer growth occurs rapidly between 900 and 1200 LT. Before sunset the convective boundary layer collapses and transitions to a nocturnal boundary layer less than 100 m in height, slowly growing to 200 m overnight.

Several notable differences exist in the boundary layer structure between the near-coast and inland location (Figure 5.7 and Figure 5.8). The most notable difference is that the seabreeze does not penetrate over the inland location. The convective boundary layer (CBL) is allowed to fully respond to the surface heating without cold advection and the stabilizing effect of the seabreeze. CBL height grows to over 1400 m by 1300 LT and

remains at that height until just after 1700 LT. It is also noticed that the TKE reaches a maximum at the same time the boundary layer reaches its full growth and then slowly declines.

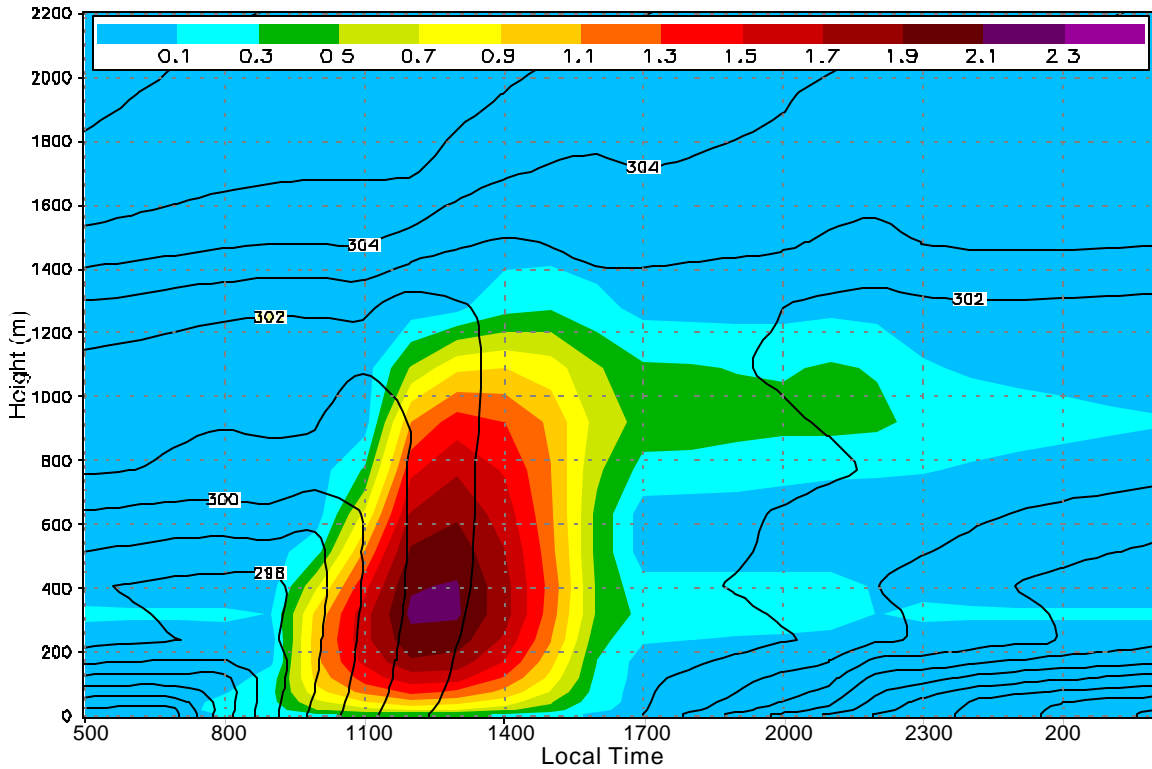


Figure 5.8 Time series profile of turbulent kinetic energy (TKE) and potential temperature at a location 100 km inland. Potential temperature is contoured each 1 degree and TKE (m^2/s^2) is shaded with legend shown.

5.3.2 CALPUFF DISPERSION SIMULATIONS

In Figures 5.9 and 5.10, the coupled ARPS/CALPUFF dispersion simulations are presented. A continuous point source emitting NO_x at a rate of 1 g s^{-1} was placed at each of the profile locations discussed in the previous analysis. These locations (a-d) are shown in a plan view of the model domain (Figure 5.9). Each source was given identical source characteristics: release height of 2 m, 1 m diameter, 1 ms^{-1} exit velocity and 300

K exit temperature. A separate simulation was performed for each source as to exclude interactions between sources in the analysis. All concentration plots are shown in units of $\mu\text{g}\cdot\text{m}^{-3}$ and derived from 100 m spaced, gridded receptors. The ground-level NO_x field is averaged over 3-hr periods. For each source the 3-hour average concentration is shown for two time periods, during the afternoon ranging from 1400-1700 LT (yellow to red shading) and during the nighttime 2300-0200 LT (lt. blue to dk. blue shading). The red (blue) contour in each panel represents the 0.01 $\mu\text{g}\cdot\text{m}^{-1}$ isopleths for the daytime (nighttime) concentration distribution.

Location (a) (shown in Figure 5.9) is 100 km inland and idealistically represents the typical boundary layer of inner continental India. The 3-hr average concentration ending at 1700 LT (Figure 5.10a, yellow to red) exhibits a gaussian distribution down wind from the source. The previous meteorological analysis (Figure 5.5a and Figure 5.8) indicated that during this time period and at this location the boundary layer was in a free-convective state with a mixed layer height on the order of approximately 1500 m. The plume direction is consistent with the northeasterly boundary layer wind field. The plume is rather wide, relative to the over water cases in Figure 5.10c and Figure 5.10d. This is consistent with a large variance in the horizontal wind and associated cross wind dispersion coefficient. In addition, the concentration declines rapidly away from the source because of the diluting effect of the strong vertical boundary layer mixing within a relatively deep boundary layer height.

The nighttime 3-hr average concentration of NO_x for this same location exhibits a much different dispersion pattern (Figure 5.10a, dark blue to light blue). The concentration of NO_x is higher and covers a much larger area both around and downwind

of the point source. The meteorological profile for this time period (Figure 5.8) indicates a very stable nocturnal boundary layer with calm winds ($<1.0\text{m}\cdot\text{s}^{-1}$). The low boundary

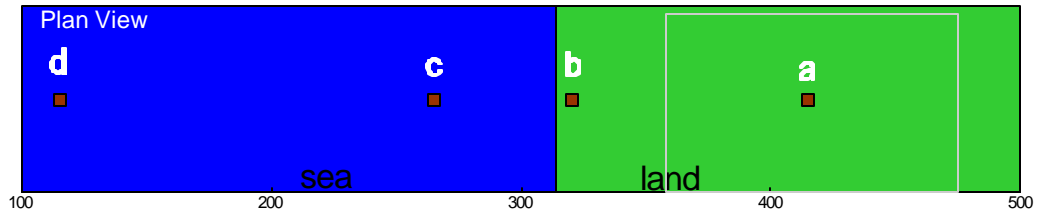


Figure 5.9 Plan view of the point source locations (a,b,c,d).

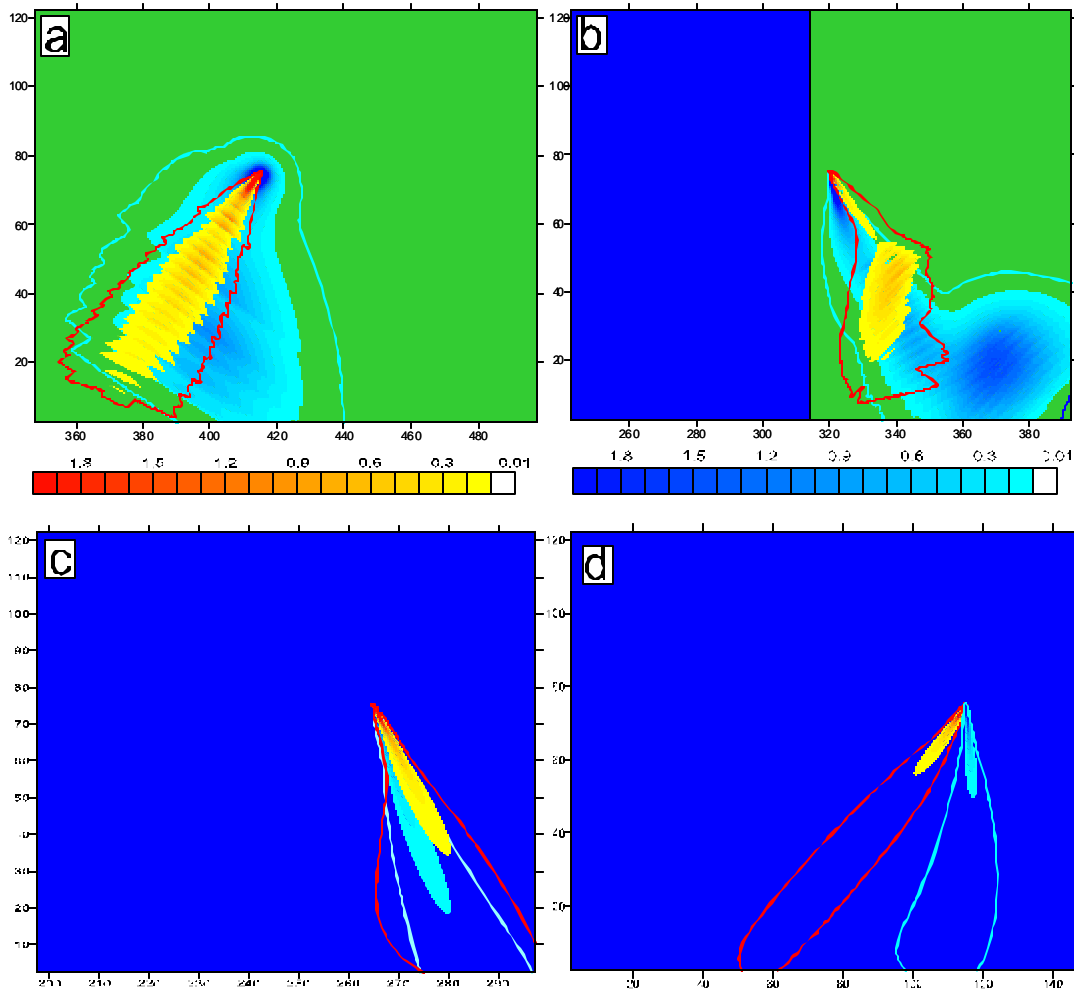


Figure 5.10 Concentration pattern of NO_x ($\mu\text{g}\cdot\text{m}^{-3}$) from the various point sources. Blue shading represents the nighttime concentrations and red shading indicates the simulated daytime concentrations.

layer height is responsible for the high surface concentrations while the very light; almost calm winds with variable wind direction allow the pollutant to pool out over a larger area.

Location **(b)** (Figure 5.10b) is 5 km inland, (shown as location **b** in Figure 5.9) and is representative of how the land-sea interface can affect dispersion patterns. The daytime 3-hr concentration contours (yellow to red) ending at 1700 LT illustrates very clearly the effect of the seabreeze on air dispersion. During this time period the seabreeze slowly advances from 15 to 25 km inland. Within the seabreeze flow the NO_x is transported onshore within a narrow plume. This is expected since the seabreeze low-level flow is less turbulent. It is noticed that an area of higher concentration exists near the seabreeze front. This is possibly due to the convergence of air along the front and the shallow layer of the seabreeze inflow (TIBL).

Nighttime concentrations from the same point source show a different spatial distribution (dark blue to light blue). Similar to the far inland case higher concentration of NO_x covers a larger area than the daytime distribution. Near the source a southward propagating gaussian plume structure is evident. This is consistent with the transition of the seabreeze (NW flow) to land breeze (NE flow). The higher concentrations are a result of the low nocturnal boundary layer height and statically stable near surface layer. A pool of higher concentrations is noticed in the southeastern quadrant of the plot. This is NO_x advected inland within the seabreeze flow earlier in the evening, as the seabreeze front propagated 50 km inland.

The next two NO_x distributions, location **(c)** and **(d)** (Figure 5.10c and Figure 5.10d), are from two point sources located 50 km and 200 km offshore. It is apparent that the diffusion of NO_x is much different within the MBL as compared to overland. The

plumes in both panels exhibit a gaussian distribution with a very narrow plume width. Without the effect of surface heating and subsequent buoyant turbulence, the only turbulence generator is surface wind stress. Since friction over water is much less than that over land and the wind speeds are light, this mechanically generated turbulence is minimal. As a result of this, horizontal and vertical variations in velocity and hence, dispersion coefficients are small. The distribution is much like what one would expect in a low turbulent flow.

There are a few differences between the two offshore locations. The point source closer to shore has a stretched plume of higher concentration. This may be attributed to the lower MBL height over the nearshore source. The plume width is somewhat wider, which may be a result of the offshore seabreeze influence. It is also noticed that the plume from the offshore source 50 km from shore (Figure 5.10c) is being advected towards land more than the plume located 200 km offshore (Figure 5.10d), a signal that the seabreeze can influence the dispersion from sources located offshore.

5.4 SUMMARY

The model simulations show that the boundary layer properties are very different across a region that is affected by a seabreeze circulation. The marine boundary layer well offshore (200 km) changes very little over the diurnal period while closer to shore (50 km) the boundary layer structure is affected. The MBL height decreases within the offshore zone of the seabreeze circulation, due to both subsidence and warmed land air advected in the return flow. Although the dispersion pattern from a point source at the surface well offshore did not change, closer to shore the concentration is higher over a

greater area due to the lower MBL. The plume was also advected towards shore because of the onshore component of the seabreeze. It can be imagined that land-based pollutants trapped in the return flow of the seabreeze would also be advected (recycled) towards shore because of this onshore component.

Close to shore, the model simulated a seabreeze that developed around mid-day at the land-sea interface. In the afternoon the seabreeze strengthened and slowly moved inland in the afternoon and then accelerated 50 km inland just before sunset. The dispersion experiment of a surface point source near the coastline indicated that the seabreeze has a very noticeable effect on atmospheric dispersion overland. Higher surface concentrations were modeled during both the seabreeze episode and during the post seabreeze period later in the evening. Pollutants were transported inland as a result of the seabreeze, and remained concentrated as the stable boundary layer formed.

Overland, the simulations depicted the evolution of the boundary layer as expected. At the well inland location (100 km), the boundary layer was shown to quickly grow during the morning, from stable to convective. In the evening the convective boundary layer quickly stabilizes, then the stable boundary layer slowly deepens through the night. Certain properties like TKE, potential temperature, momentum and boundary layer height were consistent with each other and with observational studies. Hence, the dispersion pattern of an inland point source exhibited an expected distribution; well dispersed during the daytime with low concentrations and higher concentrations at night.

CHAPTER 6

EASTERN NORTH CAROLINA REGIONAL SIMULATION

A detailed account has been given in previous chapters on the background, characteristics and configuration of the ARPS mesoscale model. This chapter presents results of a case study over central North Carolina.

6.1 REGIONAL 6-KM MODEL DOMAIN

In Figure 6.1 the 6-km ARPS domain over North Carolina is outlined in red. The area covers parts of two major regions, the Piedmont and Coastal Plains, which are marked by a large contrast in soil type, vegetation and elevation. The split occurs essentially along a line from the southwest corner of the model domain to the northeast corner. Figure 6.2 highlights the terrain and soil type characterizations used by the ARPS model for the lower boundary condition. Panel 6.2a gives the terrain height derived from USGS DEM data. The northwest portion of the domain (Piedmont) ranges from 100 m above sea level to just over 325 m, while the Coastal Plain is homogeneous in elevation.

Shown in Figure 6.2b are the soil types in the model domain. The Piedmont consists of two main soil types, silty loam and loam. The Coastal Plain soils are mostly either sandy or sandy loam. It is accepted that sandy soils do not retain moisture so they heat much more efficiently and to a higher degree than loamy soils that hold water. As seen in Figure 6.2b, a stark difference is noticed in soil type over this small region.

Three main vegetation types dominate the domain; these are deciduous forest, evergreen forest and cropland. Shown in Figure 6.3a is a spatial representation of the

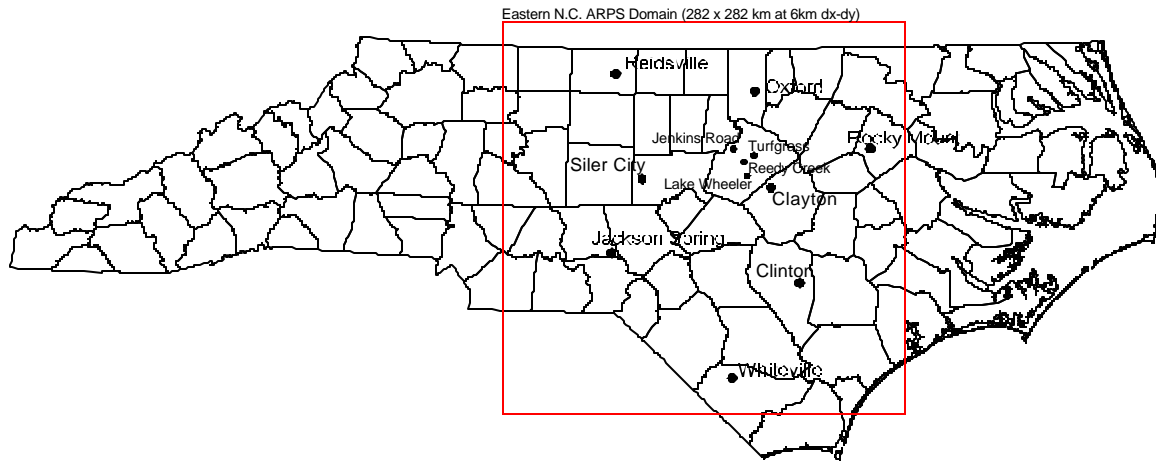
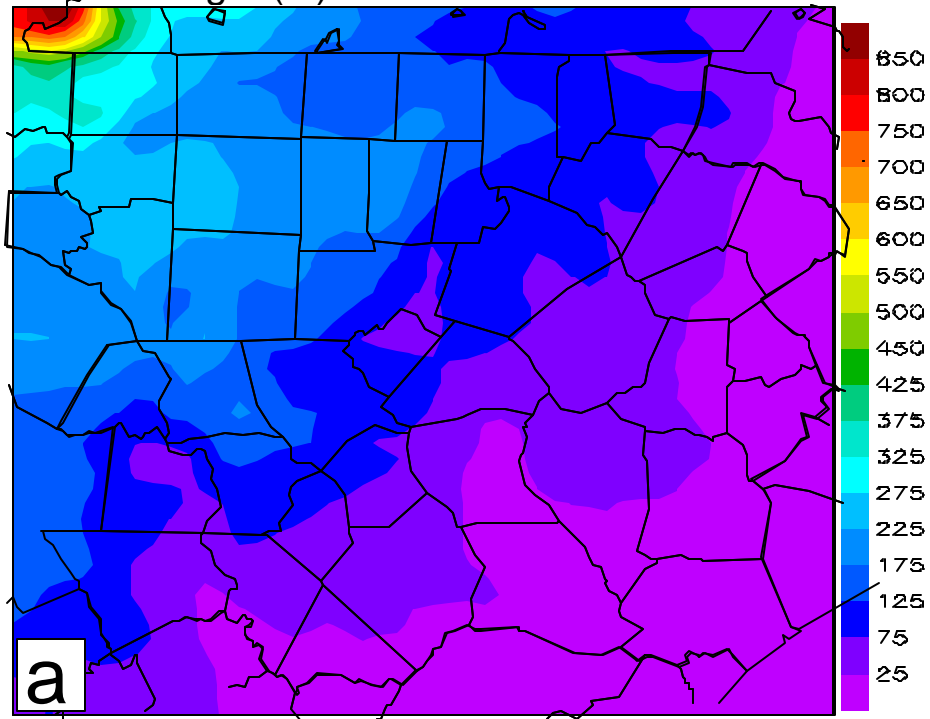


Figure 6.1 Regional view of North Carolina and the location of the 6 km ARPS model domain. Surface station (NC ECO Net) locations are depicted.

vegetation types used by ARPS. The Piedmont is primarily considered deciduous forest while the western coastal plain is made up of open agriculture fields and eastern coastal plain is either evergreen or a mix of evergreen and deciduous forest.

Surface roughness is a crucial factor in the model representation of the boundary layer structure. The values are derived from default specifications assigned to different vegetation types. Shown in Figure 6.3b is the surface roughness derived by ARPS surface preprocessing program. Correlating to the spatial vegetation pattern the specified roughness lengths are: evergreen forest 0.75 m, deciduous forests 0.55 m, open field areas 0.10 m and water 0.001 m. The disparities in surface characteristics across the region are rather large. That is why this region is being studied and the above characteristics will be used to explain the meteorological variations in the following model simulation.

Terrain Height (m)



Soil Type

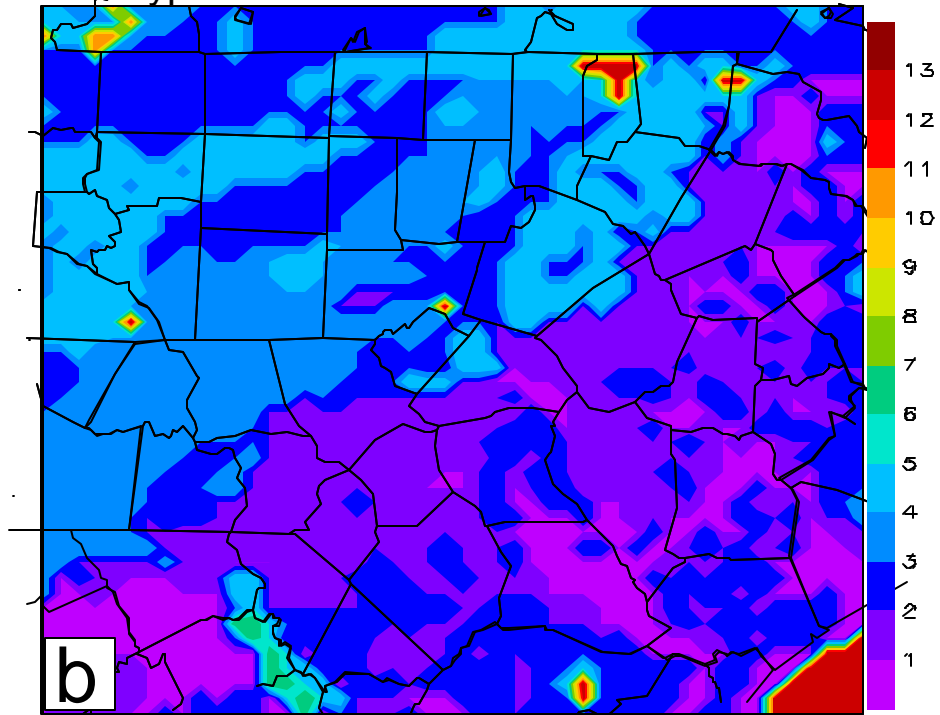
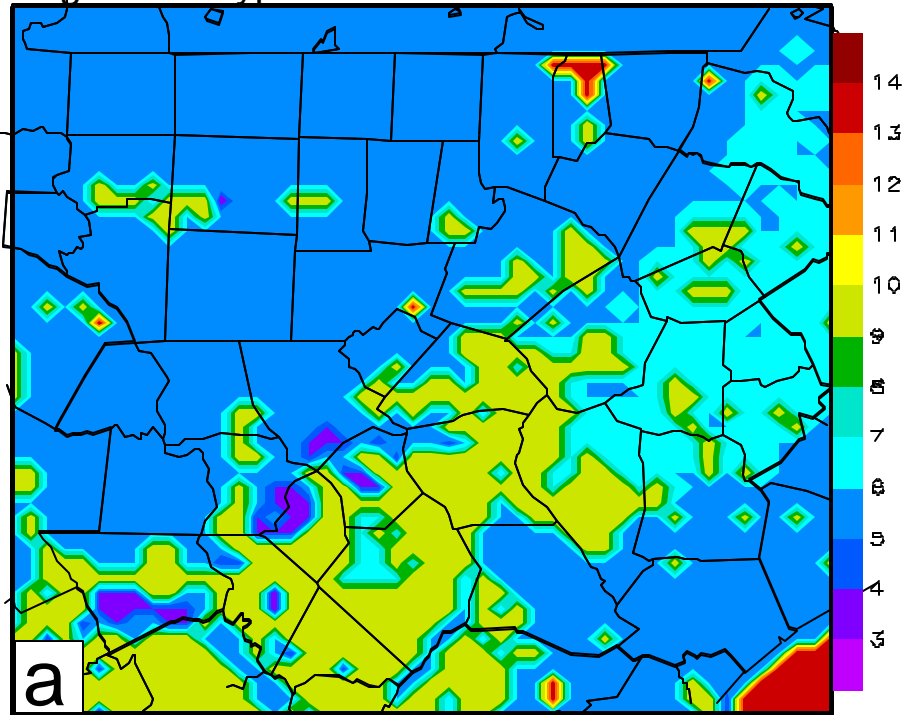


Figure 6.2 Regional view of North Carolina and the location of the 6 km ARPS model domain. Surface station (NC ECO Net) locations are depicted.

Vegetation Type



Surface Roughness

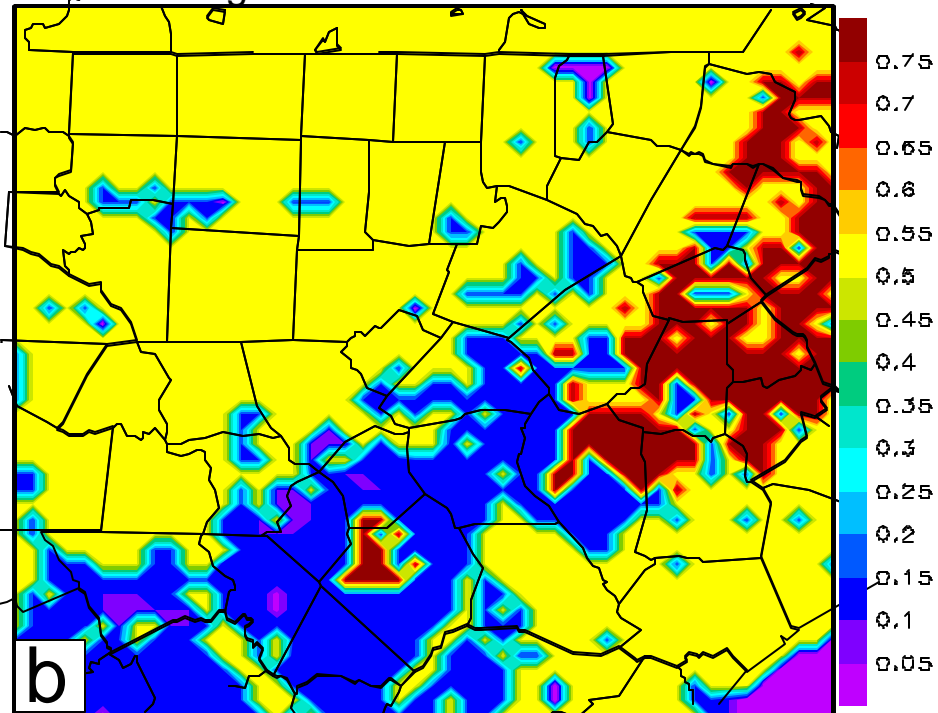


Figure 6.3 Regional view of North Carolina and the location of the 6 km ARPS model domain. Surface station (NC ECO Net) locations are depicted.

6.2 SYNOPTIC OVERVIEW

The selected period of the regional simulation is July 10, 2001 (12 UTC or 0800 LT) thru July 12, 2001 (0800 LT or 12 UTC). It represents the typical weather conditions in North Carolina during the summer season. During the summertime the Bermuda High is located in the western Atlantic Basin near Bermuda. This system is mostly a product of latitudinal circulations between the Inter-Tropical Convergence Zone (ITCZ) to the south and Arctic convergence zone to the north. The net effect is a dominant south to southwesterly flow over the Southeast U.S. around the periphery of the high-pressure system. Fronts typically move southeast from Canada, but lose identity as the potent summer solar heating modifies the air mass.

In this particular case, initially the wind was from a northerly direction, in response to a weak offshore low-pressure system well out in the Atlantic and a weak high-pressure center to the west. In general the synoptic flow was weak over the study area. Figure 6.4a gives the sea-level pressure field and surface wind barbs at 0800 LT on July 10th, from the Eta Data Analysis (EDAS). A weak pressure gradient existed over the Southeast U.S. with light north-northwest surface wind over Eastern N.C. About 24 hrs into the simulation, the weak flow veers to a southeasterly direction, then southwest for most of the day on July 11th (Figure 6.4b and 6.4c). A weak cool front propagates through the region towards the end of the simulation period, during the early morning hours of July 12th (Figure 6.4d), distinguishable by surface wind veering from a northwesterly to northeasterly direction. During this 48-hr period the large-scale pressure gradient remained weak with a wind speed around $2.5 \text{ m}\cdot\text{s}^{-1}$. A brief surge ($5 \text{ m}\cdot\text{s}^{-1}$) does occur in response to a tightening pressure gradient during the last 6-12 hour portion of the simulation as the cool front passes over the study area. This case may present a challenge

for the ARPS model since the conditions were not stationary. At the same time, it provides a 24-hr period of the typical light SW wind and little cloud cover over North Carolina.

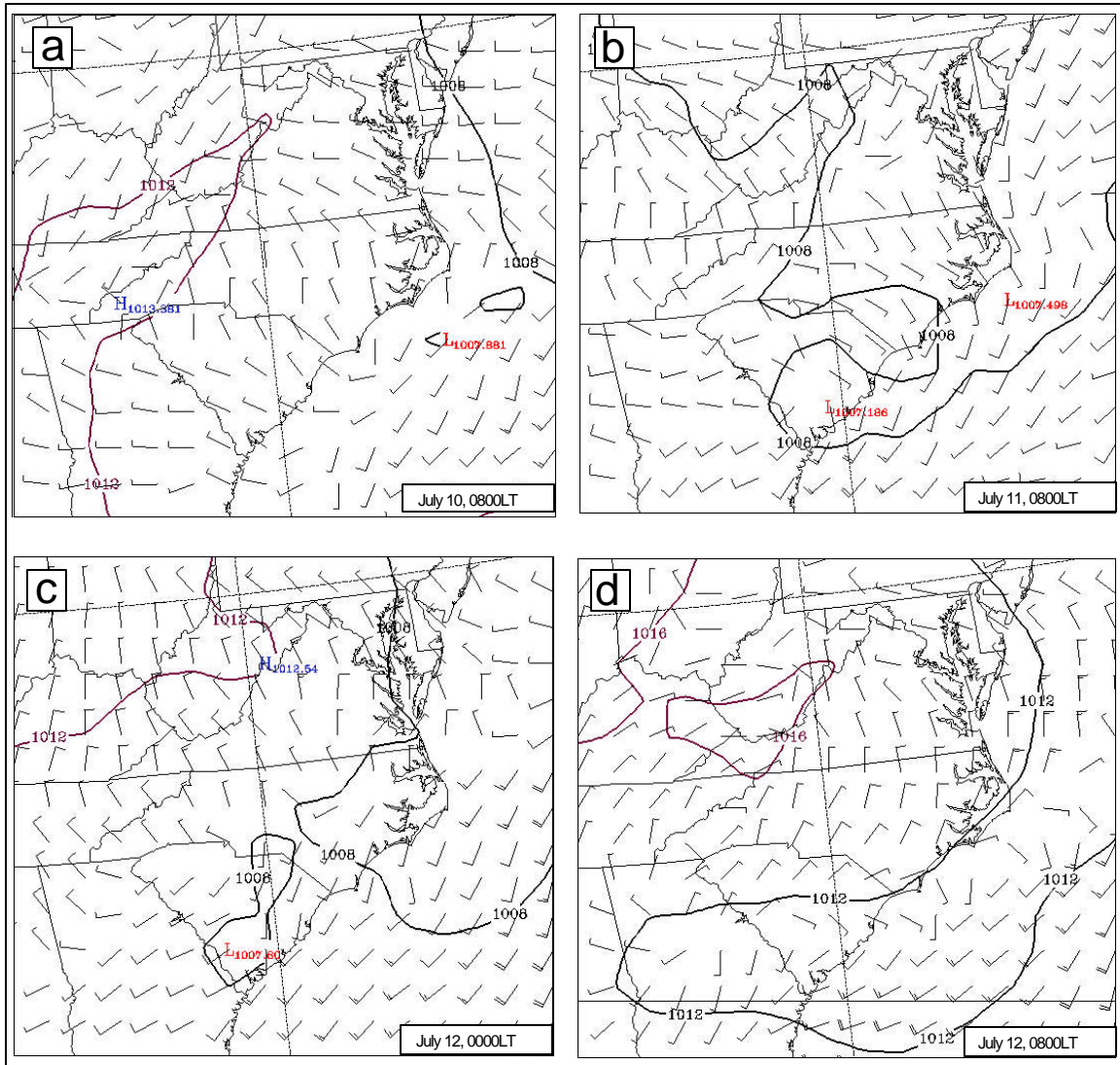


Figure 6.4 Eta Data Assimilation System (EDAS) analysis of sea level pressure gradient (mb) and 10 m wind (kt).

6.3 SPATIAL VARIATIONS OF THE SIMULATED BOUNDARY LAYER

In this simulation, several time periods were chosen in which the spatial variations of wind, surface temperature, potential temperature and TKE were examined.

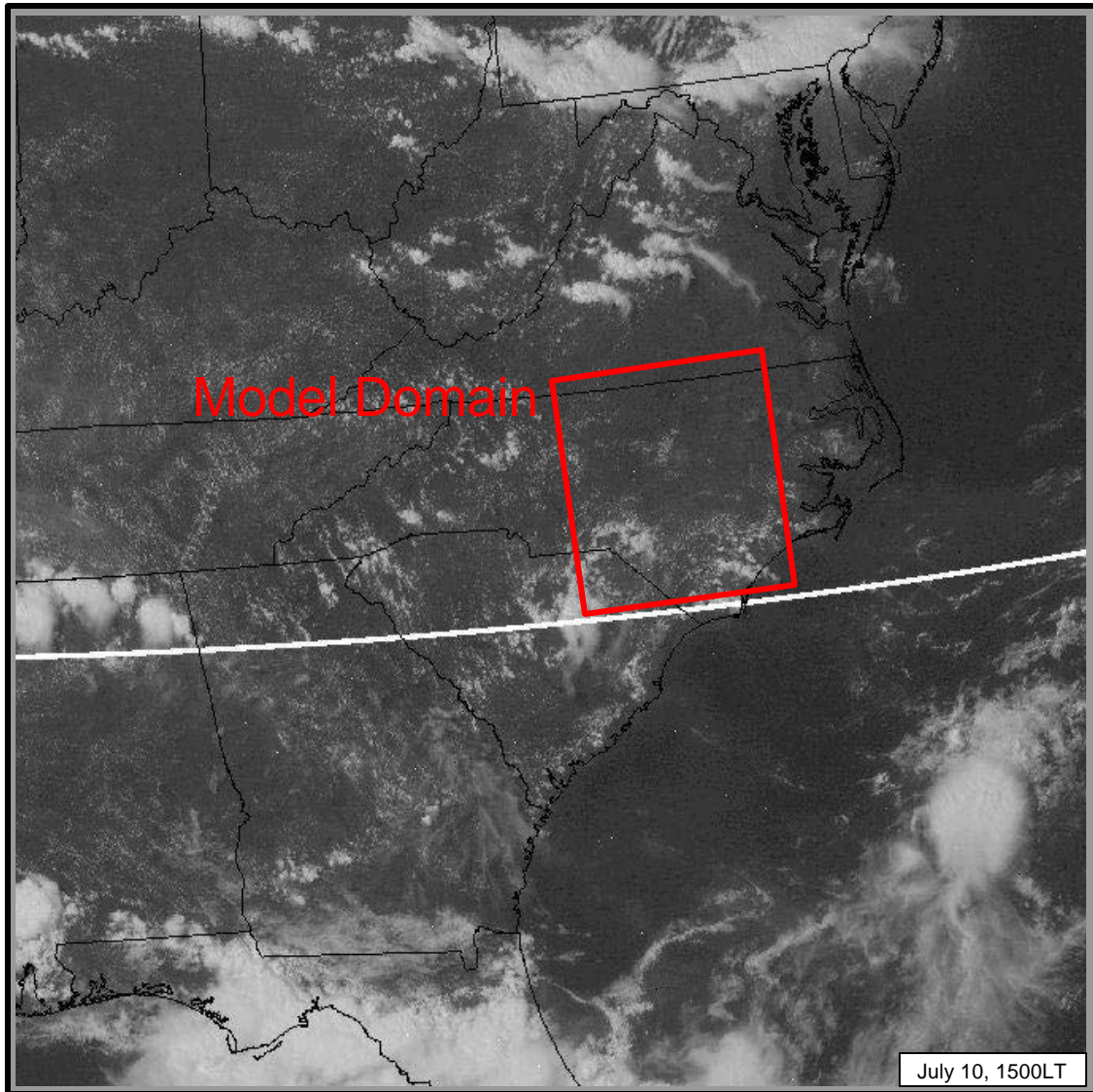


Figure 6.5 GOES-8 visible 1-km satellite image for the region on July 10, 2001 at 1500 LT.

A link between these fields and the variable surface characterization was established. The first analysis is at 1500 LT on July 10th, 7 hrs into the simulation. For the first day, the cloud cover was not extensive (Figure 6.5) and the boundary layer flow was light. This scenario is favorable for the development of a free convective boundary layer in which buoyancy generated turbulence dominates.

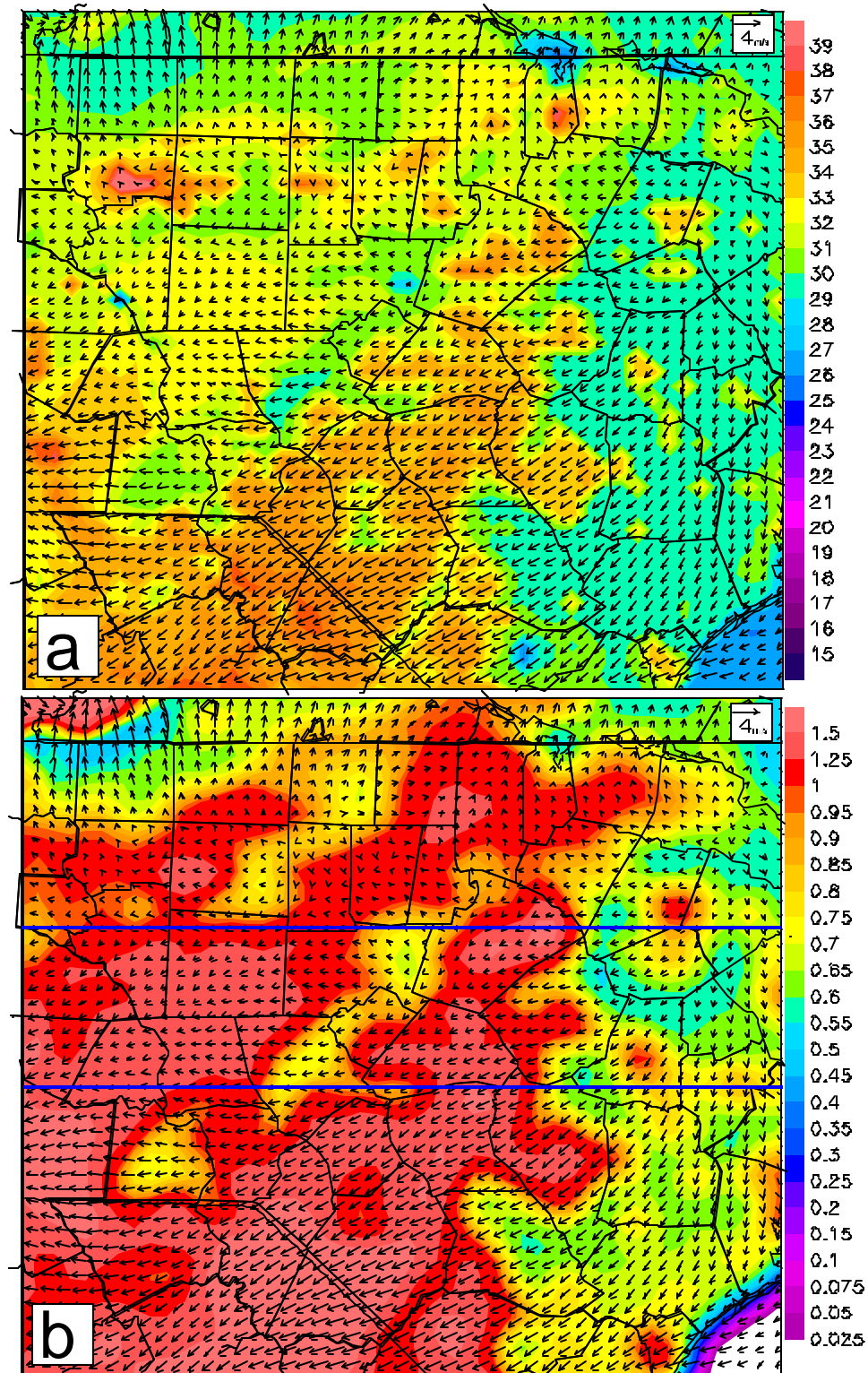


Figure 6.6 (a) Simulated 10 cm surface temperature (C) and 10 m wind vectors. (b) Simulated 100 m TKE (m^2/s^2) and 10 m wind vectors. Both panels are 8 hr forecast for July 10, 2001 at 1500 LT.

Presented in Figure 6.6 are the various properties of the surface and the boundary

layer. Figure 6.6a provides the simulated 10 cm surface temperature at this time. The surface temperature over the model domain ranges from 29° C to 39° C. Soil type and vegetation type seem to be the dominant factor in temperature variation. Areas in the “Sand hills” region of the domain, where a high percentage of the soil texture is sandy, have the highest ground temperature. To the northwest and southeast of this sandy area, where the soil has more clay and loam, the soil temperature averages 3-4° C less. Another major factor in the regional surface temperature variation is the vegetation type. Open field areas are parameterized with a lower vegetation cover and leaf-area index as opposed to deciduous and evergreen forest areas. The lower these factors, the more radiational energy allowed for heating the soil rather than transpiration, reflection and absorption by plant matter.

Comparing Figure 6.3a (Vegetation Type) with the soil temperature in Figure 6.6a yields a strikingly similar pattern. The lime green areas represent open agriculture fields while the light blue represent forests. The spatial variation shows, as expected, that the open pasture/agriculture areas that are warmest and deciduous/evergreen forest areas are coolest. From the surface temperature it appears that the pattern of correlation is better between the temperature and vegetation type, rather than between the temperature and soil type. The surface flux parameterizations (Chapter 3) allow for the modification of the thermal coefficient of bare soil by the percentage of vegetation cover.

Illustrated in Figure 6.7a is the surface skin temperature measured by Advanced Very High Resolution Radiometer (AVHRR) satellite sensors. Although these measurements are accurate over water where the surface radiative properties are known, over land the actual values are not precise. However, the surface temperature pattern may

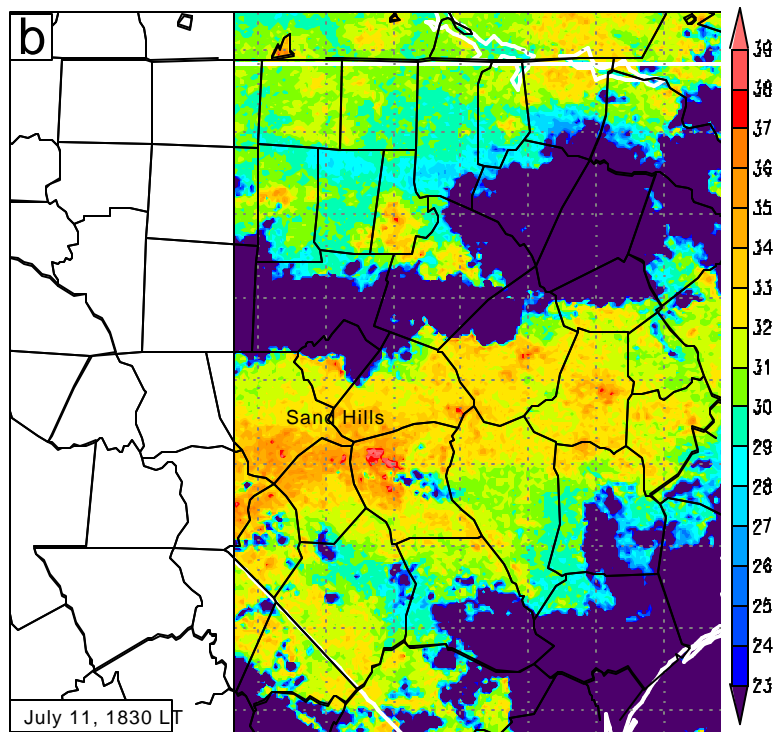
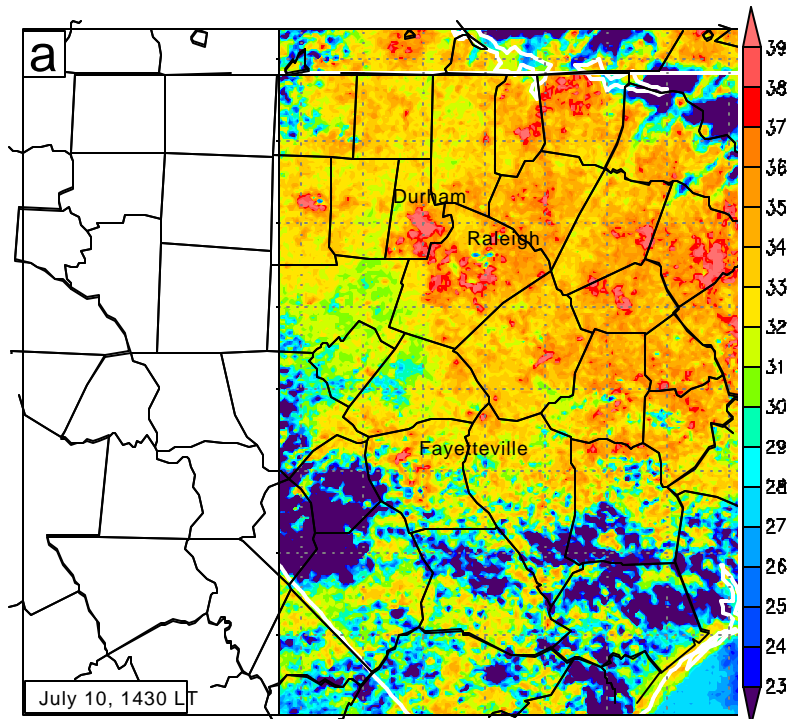


Figure 6.7 Advanced Very High Resolution (AVHRR) Satellite image showing surface skin temperature (C). (a) July 10, 2001 at approximately 1500 LT (b) July 11, 2001 near 1800 LT.

be useful to compare to simulated surface temperatures in order to reassure the land

surface thermal properties are spatially represented in the model. Both the observed (Figure 6.7a) and simulated soil temperature (Figure 6.6a) figures are plotted with the same color scheme. The significantly cooler surface temperatures in the southern part of the domain, mainly the dark blue to purple shading, are representative of cloud cover.

A spatial comparison yields many similarities as well as several discrepancies. Most of the larger urban areas including Raleigh, Durham and Fayetteville are characterized by warmer surface temperatures than their surroundings. This is mainly because, the urban areas are characterized low vegetation and low leaf area index, basically open fields and urbanized areas.

Other locations are also well simulated in term of the relative surface temperature variation. The Sandhills region around and just to the southwest of Fayetteville is warmer than the surrounding areas, although cloud cover obscures some of the Sandhills region. The convectively induced cloud cover seen in the surface temperature image confirms that this area is warmer. Another area that has a good correlation between measured and simulated temperatures is the highly vegetative area just to the southwest and west of Raleigh. This region is a thick-forested area in the Cape Fear River basin and around Lake Jordan. In both the satellite and simulated surface temperature this area is noticeably cooler than the surroundings. Although the satellite temperatures may not be precise, the observed temperatures are very close to the simulated. One exception is the Coastal Plain region; the eastern portion of the domain. This entire region appears to have slightly lower simulated surface temperatures.

In Figure 6.6a the wind vectors are superimposed on the surface temperature. It can be seen that the wind speed is stronger over central portion of the model domain,

particularly over the Sandhills. It is believed that this is primarily a result of the elevated heating in this region. Higher surface temperatures and presumable augmented heat flux, correlates with stronger surface winds. The deciduous and evergreen forest areas are cooler while the open field areas are warmer. The corresponding wind speeds over the cooler surfaces average $1-2 \text{ m}\cdot\text{s}^{-1}$ while the warmer fields have stronger winds of $3-4 \text{ m}\cdot\text{s}^{-1}$.

In Figure 6.6b the TKE at 100 m and the 10 m wind vectors are shown. The TKE varies substantially across the model domain with values as high as $1.5 \text{ m}^2\cdot\text{s}^{-2}$ and as low as $0.5 \text{ m}^2\cdot\text{s}^{-2}$. In addition, the variation directly relates to the surface temperature. On this afternoon when the wind is relatively light, buoyancy driven turbulence dominates TKE production. Therefore it makes sense that a warmer surface results in more convectively unstable boundary layer with higher turbulent energy. These highly convective areas are associated with a deeper boundary layer while the less convective areas will have a significantly lower boundary layer height as seen in the following figures.

Vertical cross section of TKE, potential temperature (contour each 1° C) and horizontal wind, from the same time period, are shown in Figure 6.8a and Figure 6.8b. The first cross section (Figure 6.8a) is taken west-east across the model domain; passing through the Raleigh metro area (shown as upper blue line in Figure 6.6b). The boundary layer is easily identified by the constant potential temperature layer near the surface and by the presence of vigorous turbulent mixing energy. The vertical TKE distribution is consistent with similarity theory and with past observations that state; the maximum TKE within the convective boundary layer occurs at approximately $1/3^{\text{rd}}$ the boundary layer height. The western part of the cross section has maximum TKE of $1.5 \text{ m}^2\cdot\text{s}^{-2}$, occurring at

approximately 400 m. The boundary layer height over this region is approximately 1100 to 1300 m. Another TKE peak ($2 \text{ m}^2\cdot\text{s}^{-2}$) and elevated 1200 m boundary layer height, exists over Raleigh-Durham. Several areas of dampened TKE are also noticed. One over the cooler vegetative surfaces, west of Raleigh, has a minimum in TKE and also a minimum in boundary layer boundary layer height (900 m). Other cooler regions to the east of Raleigh have even less turbulent energy and lower boundary layer heights on the order of 700 m.

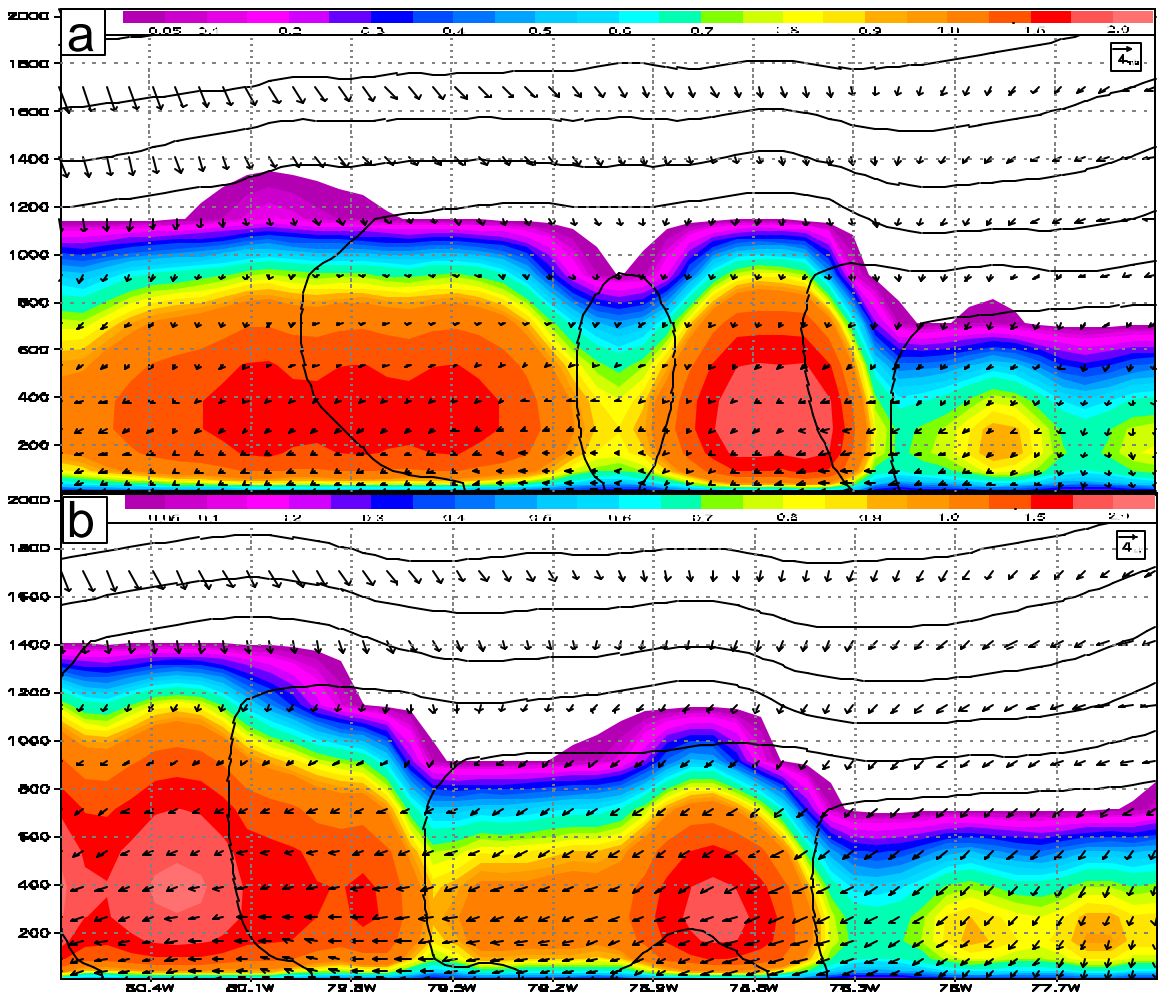


Figure 6.8 (a) Simulated vertical cross-section of potential temperature (contoured each 1 degree), TKE (m^2/s^2) and horizontal wind vectors for July 10, 2001 at 1500 LT for the upper cross-section. (b) Same but for lower west-east cross section depicted in Figure 6.8b.

Overall the boundary layer height seems rather low for the degree of simulated mixing. In this region, during northwesterly 850 mb flow regimes, where the flow is down slope off Appalachian Mountain range, subsidence in the lee of the 2000 m mountain range causes the layer below to warm appreciably. This heating results in a strong inversion, which effectively lowers the potential growth of the boundary layer. In the potential temperature profile, a strong inversion is noted between 1200-2000 m.

In Figure 6.8b, a similar vertical cross section is shown but 50 km south of Raleigh (noted as lower blue line in Figure 6.7b). The same general features are seen, highly convective areas in the western and central portion of the profile, where the surface temperatures are higher. The boundary layer height is actually higher in the western part (1400 m) than the previous profile (1200 m). In the eastern portion of the profile the boundary layer drops to 700 m. Not shown by these figures is the vertical velocity in the boundary layer. It was examined and indicated that there are in fact areas of strong ascent along the boundaries of the high TKE and moderate descent over the areas of low TKE. Differential heating between different landuse types directly causes these circulations, which in turn influence the generation of buoyancy driven TKE and influences mixing height.

The next analysis is for the second day of the simulation, July 11th at 1800 LT. In Figure 6.9a the simulated 10 cm surface temperature is shown alongside the 10 m wind vectors. Similar to the previous analysis, the regional bias of warmer surface temperature is forecast over the Sandhills region of N.C. The surface temperature in this region averages 36° C while surrounding areas range from 29° C to 32° C. The urban centers are approximately 3° C warmer than the surrounding areas. At this time of day the surface

generally begins to cool as the sun angle lowers. Landuse is most noticeable this time of evening where the vegetation pattern, correlates best with the surface temperature variation.

Figure 6.7b provides the AVHRR satellite derived surface skin temperature for the same region, at approximately the same time. In general, the correlation is good between the observation and simulation. The Sandhills region is well depicted as a warmer surface in the satellite image, even though cloud cover obscures areas of the region. Urban centers of Raleigh, Fayetteville/Fort Bragg and Durham are visible as the warmest surfaces. Even the portions of the eastern domain, which seemed to be simulated to cool on the previous day, are better represented.

Overall the wind speed is stronger if compared to the previous day. It appears that a weak surface trough of low pressure is passing through the area. Lighter southwest to west wind is noticed ahead of the trough while stronger northwest winds exist in the central and western domain, behind the trough.

Figure 6.9b shows the 100 m TKE distribution over the model domain. Again, associated with the warmer surface is higher boundary layer turbulence ($1.0 \text{ m}^2 \cdot \text{s}^{-2}$) and higher surface wind speeds ($3\text{-}4 \text{ m} \cdot \text{s}^{-1}$). The increasing synoptic scale momentum above the boundary layer is more easily transferred to the surface by passing through the unstable PBL. The cooler surface areas are quickly stabilizing and represent lower turbulent kinetic energy. The increasing static stability also lessens the amount of downward transport of momentum as an inversion develops near the surface. This late afternoon time was chosen because it illustrates how the surface landuse patterns dramatically influence the spatial variation in the boundary layer. It also shows how the

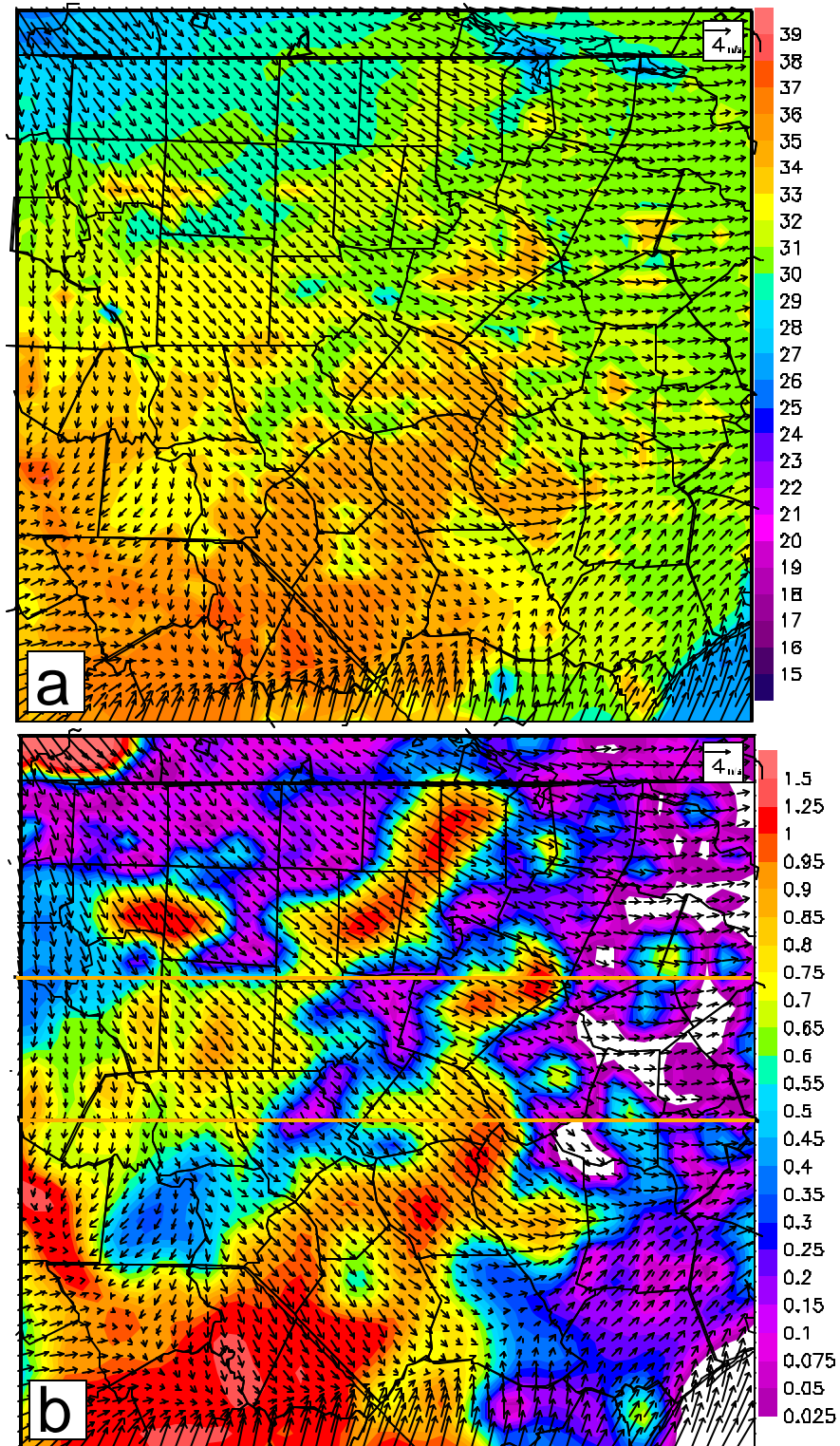


Figure 6.9 (a) Simulated 10 cm surface temperature (C) and 10 m wind vectors. (b) Simulated 100 m TKE (m^2/s^2) and 10 m wind vectors. Both panels are 33 hr forecast for July 11, 2001 at 1800 LT.

urban heat island effect can maintain stronger turbulent mixing even as the surrounding

northwest boundary layer flow is approximately $6-8 \text{ m}\cdot\text{s}^{-1}$, much stronger than the previous day. The sustained TKE over Raleigh is several times higher than surrounding areas. Just to the east and west of Raleigh, the turbulence has almost completely diminished, with values on the order of $0.1 \text{ m}^2\cdot\text{s}^{-2}$. Another noticeable difference between this day and the previous day is the potential temperature distribution and boundary layer height. The boundary layer height over the more turbulent areas is on the order of 2000 m, almost twice the previous day. This could be explained by the fact that a front is progressing through the area, bringing along cooler temperatures aloft. Different from the previous day, this effectively removes the low-level inversion (cap) allowing the boundary layer to more easily grow through rapid entrainment. Another factor is the stronger boundary layer winds, which aid in shear-induced boundary layer growth.

The lower cross-section (Figure 6.10b) is 50 km south of Raleigh, crossing through the northern portion of the Sandhills. This cross-section dissects several highly turbulent boundary layers. The most notable is over the warm surface of the Sandhills. Similar to the urban heat island effect, this region prolongs instability, relative to surrounding cooler areas. The boundary layer height over these convective areas is approximately 2000 m, while the region to the east of the Sandhills is becoming less unstable with a boundary layer height ranging from 1000-1400 m.

The third analysis from this 48-hr simulation occurs at 0400 LT on July 12th. At this time an interesting feature is propagating through the region. The sea-level pressure and surface wind depicted by the EDAS analysis in Figure 6.4d indicated a backdoor cold front that passed through the region during the last 12-hrs of the simulation. The model simulation does a good job capturing the evolution of this disturbance. In Figure 6.11a,

the 10 cm surface temperature and 10 m wind are shown for 0400 LT. Surface

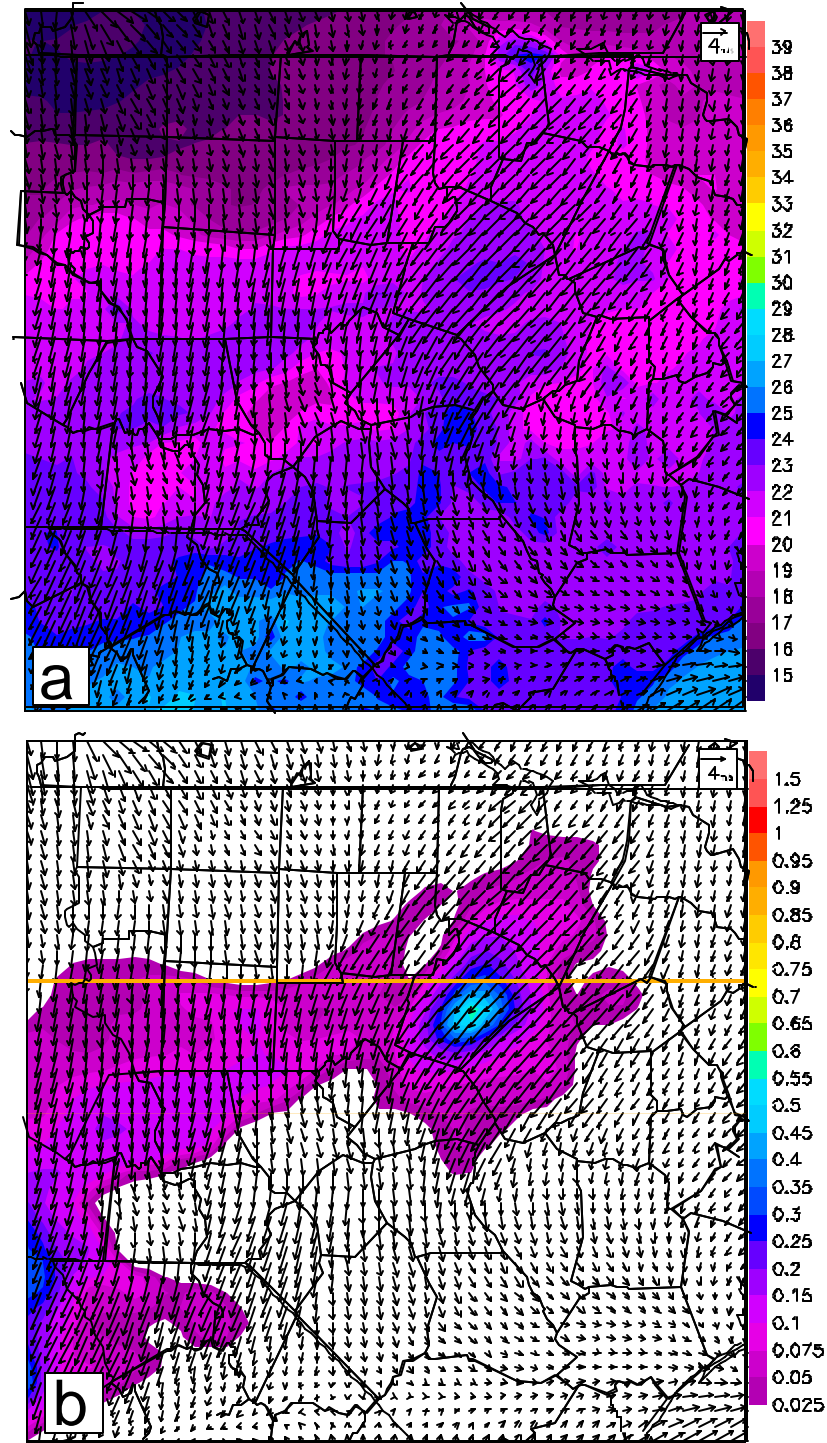


Figure 6.11 (a) Simulated 10 cm surface temperature (C) and 10 m wind vectors. (b) Simulated 100 m TKE (m^2/s^2) and 10 m wind vectors. Both panels are 43 hr forecast for July 12, 2001 at 0400 LT.

temperatures are once again warmer over the Sandhills and over the urban centers (23-24°C) while cooler over the forested areas (20-21°C). The windfield depicts the frontal disturbance very well as a surge of 4-5 m·s⁻¹ northeasterly winds. Figure 6.11b provides the corresponding 100 m TKE and 10 meter wind for the same time. The front is also shown to increase the turbulence near the surface. Mechanically induced turbulence is enhanced by increased wind shears near the surface. Turbulence is stronger and the boundary layer is slightly deeper over the warmer land surface around Raleigh. The static stability is lowered when the surface is warmer; this allows less restriction on forced convective mixing. Figure 6.12a shows the west-east vertical cross-section that passes through the Raleigh area. A thin layer of significant TKE exists close to the surface where this wind shear induced turbulence is generated. The stable boundary layer depth averages approximately 100 m with the maximum TKE (0.5-0.9 m²·s⁻²) values occurring near the surface. A very strong jet is noticed between 100 and 600 m where wind speeds are on the order of 12-14 m·s⁻¹. It is also noticed that the static stability is strong, which reduces the surface wind substantially. The potential temperature cross-section also reveals the presence of the front. From west to east the potential temperature decreases, especially at higher levels. The largest cool advection aloft occurs near the frontal position. This baroclinicity is the forcing behind the stronger upper-level winds. This is an interesting example of how the boundary layer structure may behave during cold frontal passage.

The next cross-section, 50 km south of the previous one, shows basically the same properties. Figure 6.12b is a cross-section over the central portion of the domain; the location is noted on Figure 6.11b. A thin layer of higher turbulence exists at two locations

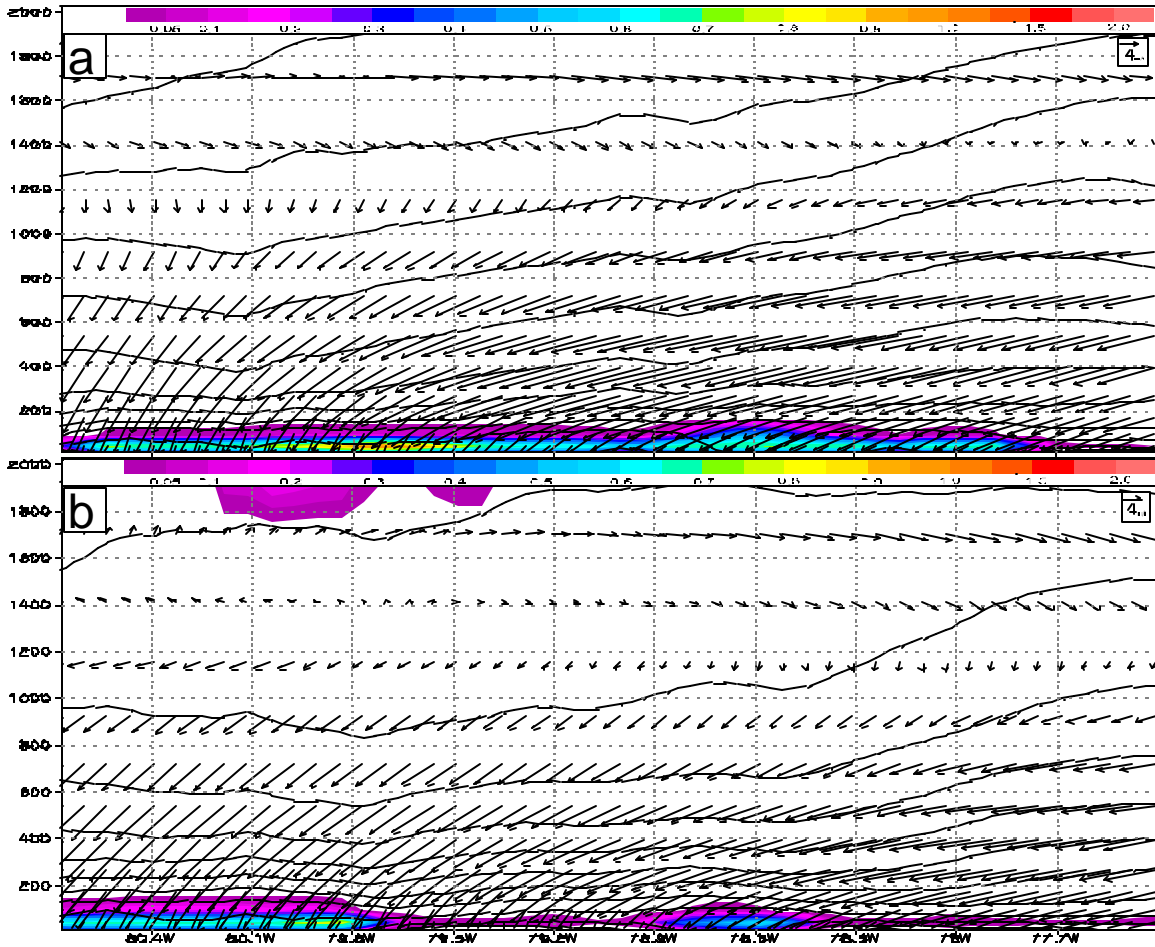


Figure 6.12 (a) Simulated vertical cross-section of potential temperature (contoured each 1 degree), TKE (m^2/s^2) and horizontal wind vectors for July 12, 2001 at 0400 LT for the upper cross-section. (b) Same but for lower west-east cross section depicted in Figure 6.8b.

near the surface; indicating the depth of the shear induced nocturnal boundary layer being between 100-150 m. The more turbulent layers correspond to the same areas that have stronger 10 m winds, approximately $5 \text{ m}\cdot\text{s}^{-1}$. The areas in between are less turbulent and associated nocturnal boundary layer is shallower. Consistent with the reduced turbulence, the near surface wind is much lighter ($1\text{-}2 \text{ m}\cdot\text{s}^{-1}$). Similar to the previous cross-section, a strong jet of east-northeasterly wind exists above the boundary layer to a height of 600-800 m. It is also seen that the leading edge of the advancing front is consistent with the

vertical potential temperature distribution. The isentropes slope upwards from the front towards the cooler air to the northeast. Ahead of the front there is little in the way of horizontal temperature gradient.

6.4 COMPARISON OF SIMULATED AND OBSERVED METEOROLOGY

An array of surface observations from the NC EConet's AgNET cluster is now used to explicitly evaluate the model simulation. From the eleven AgNET stations within the 6-km model domain; observations of 2 m temperature and 10 m wind speed and direction are compared with the same time series of simulated data from the closest grid point to these surface stations. In addition to time series comparison plots for each station, a table of model performance statistics is provided. These statistics break the time series down into three categories: the entire time series, daytime and nighttime. Daytime is defined as the time period between 0800 LT and 2000 LT, while nighttime is defined as 2100 LT to 0700 LT. These statistical measures of model performance include five indicators: mean bias error (MBE), variance (VAR), root mean square error (RMSE), mean average error (MAE) and index of agreement (IOA). Refer to Chapter 3, Section 5 for more details on the model performance statistics.

In Figure 6.13, a comparison between the simulated (blue) and observed (red) 2 m temperature time series is provided for each of the AgNET stations. Corresponding to these time series, statistical measures of model performance are given in Table 6.1. It appears that the model slightly underestimates the near surface temperature. During the daytime this trend is more apparent as all locations have warmer high temperatures than predicted. During the first day of the simulation, the maximum high temperature is as

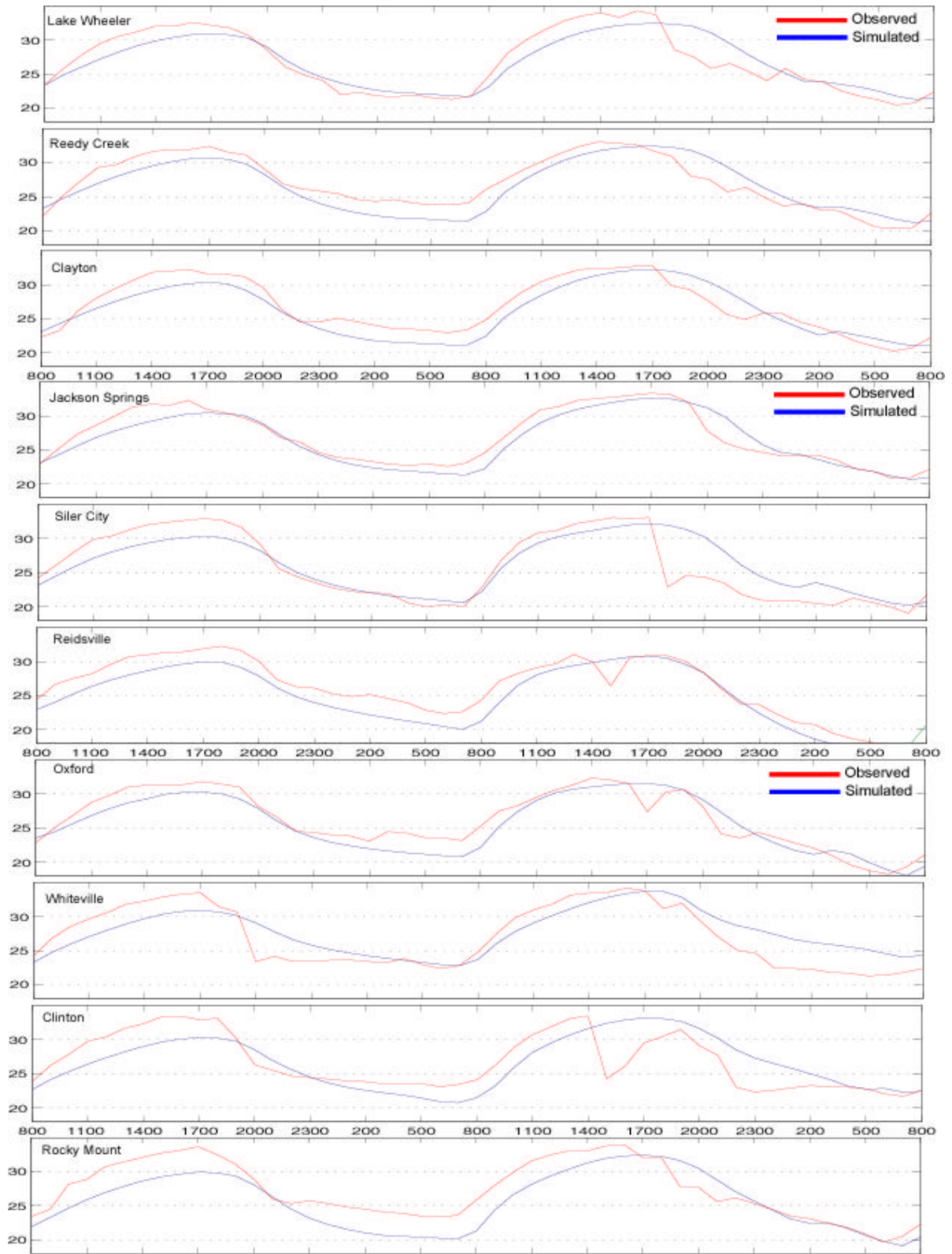


Figure 6.13 Observed and simulated 2 m temperature, 48 hr time series for all NC ECO Net stations.

much as 3.5 °C higher (Whiteville, Clinton and Rocky Mount) than forecasted. Simulated

daytime temperatures at several stations were better, with underestimates of the high temperature being only 1-1.5°C; these include the stations of Lake Wheeler, Reedy Creek, Jackson Springs and Oxford.

Table 6.1 Performance statistics of the simulated and observed 2-meter temperature

Stats	Obs Sta.	LakeW	Reedy	TurfG	Clay	JackS	SilerC	Reidv	Oxfd	White	Clint	RockyM	JenkR	Avg All
MBE	All	-0.12	-0.60	-0.98	-0.76	-0.59	0.24	-1.56	-0.73	0.58	-0.18	-1.72	-0.72	-0.60
	Day	-1.24	-0.95	-0.96	-1.09	-1.24	-0.98	-1.44	-0.89	-1.45	-1.14	-2.36	-1.16	-1.24
	Night	1.03	-0.22	-1.00	-0.42	0.07	1.51	-1.60	-0.54	2.56	0.77	-1.06	-0.27	0.07
VAR	All	3.56	2.92	2.49	2.45	1.71	6.88	1.51	2.23	6.19	8.39	3.85	1.43	3.63
	Day	3.18	2.15	2.32	1.82	0.75	8.11	2.21	2.06	1.65	10.66	3.28	0.72	3.24
	Night	1.53	3.64	2.87	3.04	1.91	2.93	0.77	2.48	2.79	4.93	3.86	1.86	2.72
RMSE	All	1.87	1.79	1.84	1.73	1.42	2.61	1.98	1.65	2.53	2.87	2.59	1.38	2.02
	Day	2.14	1.72	1.77	1.71	1.50	2.95	2.05	1.66	1.92	3.40	2.96	1.43	2.10
	Night	1.59	1.88	1.94	1.76	1.36	2.26	1.82	1.63	3.04	2.31	2.20	1.36	1.93
MAE	All	1.51	1.59	1.59	1.54	1.12	1.94	1.75	1.39	2.16	2.37	2.21	1.18	1.70
	Day	1.93	1.54	1.58	1.60	1.27	2.30	1.77	1.37	1.74	3.01	2.73	1.28	1.84
	Night	1.13	1.66	1.62	1.51	0.96	1.62	1.65	1.38	2.58	1.83	1.71	1.10	1.56
IOA	All	0.94	0.94	0.93	0.95	0.97	0.91	0.95	0.96	0.88	0.84	0.90	0.97	0.93
	Day	0.86	0.90	0.90	0.91	0.94	0.75	0.83	0.89	0.89	0.71	0.80	0.93	0.86
	Night	0.89	0.83	0.83	0.85	0.92	0.80	0.93	0.90	0.61	0.75	0.82	0.92	0.84

Table 6.2 Performance statistics of the simulated and observed 10-meter wind speed.

Stats	Obs Sta.	LakeW	Reedy	TurfG	Clay	JackS	SilerC	Reidv	Oxfd	White	Clint	RockyM	JenkR	Avg All
MBE	All	0.06	0.66	0.75	0.87	0.07	0.48	0.22	0.70	0.51	0.25	0.10	0.93	0.47
	Day	-0.20	0.33	0.37	0.40	-0.28	0.09	-0.01	0.33	0.70	0.31	-0.06	0.44	0.20
	Night	0.33	0.94	1.12	1.27	0.37	0.86	0.46	1.04	0.35	0.16	0.24	1.35	0.71
VAR	All	0.45	0.65	1.12	0.88	1.03	0.77	0.54	0.73	1.17	0.79	0.41	0.84	0.78
	Day	0.48	0.42	1.03	0.53	0.68	1.00	0.67	0.44	1.39	0.43	0.49	0.99	0.71
	Night	0.31	0.67	1.00	0.80	1.16	0.29	0.34	0.78	0.96	1.15	0.32	0.21	0.67
RMSE	All	0.67	1.04	1.29	1.27	1.01	0.99	0.76	1.10	1.18	0.92	0.64	1.30	1.01
	Day	0.71	0.72	1.06	0.81	0.86	0.98	0.80	0.73	1.35	0.71	0.69	1.07	0.87
	Night	0.63	1.23	1.49	1.54	1.12	1.01	0.74	1.36	1.02	1.06	0.61	1.43	1.10
MAE	All	0.55	0.83	1.00	0.98	0.82	0.87	0.61	0.84	0.97	0.75	0.51	1.18	0.83
	Day	0.61	0.63	0.75	0.62	0.70	0.85	0.66	0.53	1.15	0.59	0.56	0.94	0.72
	Night	0.51	0.98	1.24	1.28	0.91	0.91	0.57	1.11	0.83	0.89	0.47	1.35	0.92
IOA	All	0.87	0.59	0.52	0.52	0.71	0.72	0.63	0.63	0.47	0.66	0.77	0.39	0.62
	Day	0.86	0.81	0.67	0.79	0.56	0.66	0.72	0.83	0.18	0.62	0.82	0.39	0.66
	Night	0.87	0.36	0.42	0.27	0.76	0.77	0.35	0.42	0.68	0.65	0.62	0.33	0.54

On the second day of the model simulation, the model better estimated the high temperatures. Most surface observations are less than 1°C warmer than the simulation. The mean bias error (MBE) in Table 6.1 indicates that over the entire time series, during the daytime, all stations temperatures are underestimated. The negative bias of the model is most apparent at Rocky Mount (-2.36), Whiteville (-1.45) and Reidsville (-1.44). Some of the less bias stations include Reedy Creek (-0.95), Turfgrass (-0.96) and Oxford (-0.89). The average bias for all stations during the daytime is -1.24.

Mean average error (MAE) is a good indicator of the average absolute difference between the simulated and observed value. For the daytime period the MAE for all the station averages 1.84°C . Certain stations like Jenkins Road and Jackson Springs have a low MAE closer to 1°C , while other stations, such as Clinton and Rock Mount are nearly 3°C . The index of agreement (IOA) is another good measure of model performance. The IOA for the daytime temperatures indicates the model does a good job at catching the trends in the temperature time-series. Most stations have an index of agreement 0.90 or above.

It is noticed that a sudden decrease in the observed temperature occurred at several stations; these are not present in the simulated time series. The records show that rain accompanied these temperature drops. Radar images indicated a weak line of storms formed over the Sandhills and moved southeast towards the coast. The model simulations did form weak storms around this time but the storms were displaced much further south. A possible reason for the lack of showers in the model simulation may be overall negative bias in temperature, which will reduce the instability and lead to less rainfall. This large difference in temperature extends into the late evening for these affected stations.

Nighttime temperatures were simulated well when compared to the observations. Figure 6.13 indicates the first overnight period, for several of the surface stations, was well represented by the model, with differences less than 0.5°C . The better-simulated locations include Lake Wheeler, Jackson Springs, Siler City and Whiteville. A few stations were not as well represented; among these are Rocky Mount and Reidsville. Over the second nighttime period, the 2 m temperatures are well characterized by the model.

Similar to the first night, Lake Wheeler and Jackson Springs were almost perfectly simulated, as are stations like Reedy Creek, Clayton, Reidsville, Oxford and Rocky Mount. The statistics (Table 6.1) show that, indeed the nighttime temperatures were much better simulated than the daytime temperatures. However, large biases occurred during periods following the rain-induced cool down in the observations at some stations including Whiteville, Siler City, Clinton and Lake Wheeler. These stations have a positive bias because of the rain event while the other stations have a weak negative bias. The average bias of all stations is 0.07.

The MAE during the night is consistently lower than the daytime. Some stations are dramatically improved like Rocky Mount (Lake Wheeler), which had a MAE of 2.73 (1.93) during the day and 1.74 (1.13) at night. The average MAE for all the stations is 1.84 during the day and 1.56 at night again showing the better overall precision at night.

The next analysis involves the comparison between the simulated and observed wind speeds at 10 m. Similar to the 2 m temperatures, the observed wind speeds from the AgNET surface stations are compared to the model predicted wind speeds at the closest grid points. Figure 6.14 presents the time series of both the observed and predicted 10 m wind speed for each surface station. In general both the observed and simulated wind speeds across the domain are similarly light (less than $2 \text{ m}\cdot\text{s}^{-1}$) for the first 24 hr period while stronger for the second period. The time series comparison is strikingly alike for many of the stations. For example, at Rocky Mount the wind speed starts off at $1 \text{ m}\cdot\text{s}^{-1}$ and remains light for the first daytime period. The observed wind speed is almost identical to that predicted during this time. At the beginning of the second day, both the observed and predicted wind increases to $3 \text{ m}\cdot\text{s}^{-1}$ as daytime heating is realized. Just

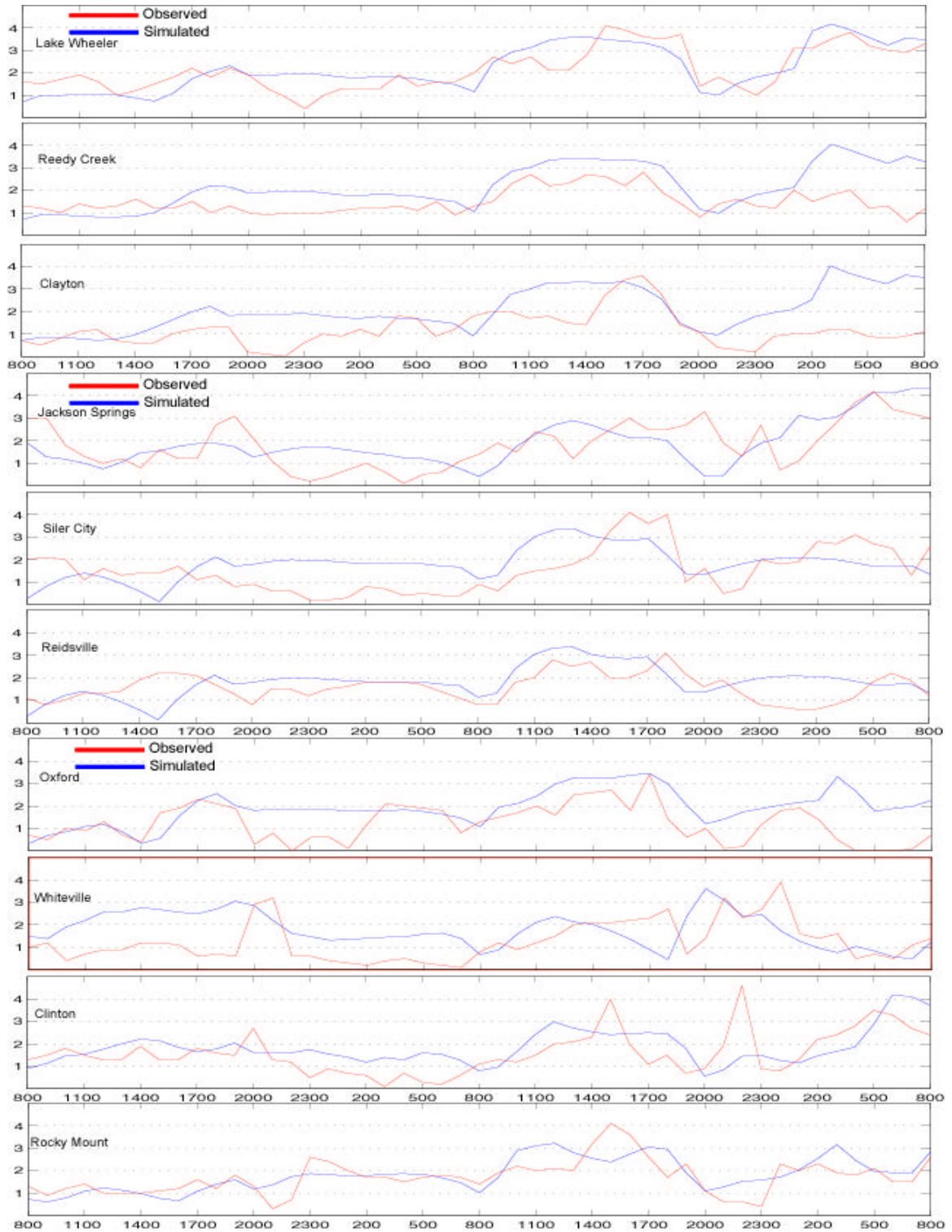


Figure 6.14 Observed and simulated 10 m wind speed, 48 hr time series for all NC ECO Net stations.

before sunset the wind relaxes in both the observed and simulated time series. In the early

morning on the last night of the simulation, the wind increases once again in response to the cool front that passes the area.

Statistics for this time series are given in Table 6.2. Smallest values of RSME and MAE, over the entire time-series occur at Rocky Mount. Lake Wheeler was also well represented by the model simulation. The model picks up on an increase in wind speed from $1.0 \text{ m}\cdot\text{s}^{-1}$ to $2.0 \text{ m}\cdot\text{s}^{-1}$ at around 1400 LT on the first day. On the second day the simulation depicts an increase in wind speed from $1.0 \text{ m}\cdot\text{s}^{-1}$ to $3.5 \text{ m}\cdot\text{s}^{-1}$; this same trend is shown in the observations. The same decrease in wind speed at 2000 LT on the second day, as well as the abrupt increase towards the end of the simulation period are shown in both data sets. The MAE at Lake Wheeler for the entire time series is $0.55 \text{ m}\cdot\text{s}^{-1}$.

Several stations have poorly represented winds by the model. These include Turfgrass, Jenkins Road and Whiteville. Some of the discrepancies may be attributed to the fact that the measurement height at Turfgrass is at 2 m not the standard 10 m and the Jenkins Road site has a close, tall canopy of trees surrounding the tower from all sides. Whiteville's poor correlation is not completely understood but it could be due to its proximity to the boundary of the model. However, the statistics reveal that all but one station had a MAE of less than $1.0 \text{ m}\cdot\text{s}^{-1}$, with most of these close to $0.75 \text{ m}\cdot\text{s}^{-1}$. The average MAE of all the stations is $0.83 \text{ m}\cdot\text{s}^{-1}$. A slightly lower average MAE is observed during the day ($0.72 \text{ m}\cdot\text{s}^{-1}$) as compared to night ($0.92 \text{ m}\cdot\text{s}^{-1}$).

Hogrefe et. al. (2001) calculated similar model performance statistics for the RAMS and MM5 modeling systems and found MAE of the wind speed, 1.41 and $1.34 \text{ m}\cdot\text{s}^{-1}$, respectively. Their study also showed that both the RAMS and MM5 have positive

bias for the 10 m wind speed. The bias of the model (MBE) indicates that these models, consistently over estimate the 10 m wind speed.

The better simulated stations in terms of the MAE, (Lake Wheeler and Rocky Mount) have small positive bias (MBE) values of $0.06 \text{ m}\cdot\text{s}^{-1}$ and $0.10 \text{ m}\cdot\text{s}^{-1}$, respectively. The average bias of all stations is $0.47 \text{ m}\cdot\text{s}^{-1}$, which compares to the MBE values of $0.61 \text{ m}\cdot\text{s}^{-1}$ for the RAMS and $0.28 \text{ m}\cdot\text{s}^{-1}$ for MM5. Breaking the bias down by day and night indicates that most of the positive bias is a result of over predicting the nighttime wind speed. The nighttime wind speed bias for all stations averages $0.71 \text{ m}\cdot\text{s}^{-1}$ while the daytime is only $0.20 \text{ m}\cdot\text{s}^{-1}$. The index of agreement (IOA) between the simulated and observed wind speed is not as good as for the temperature, but decent relative to the more difficult prediction of wind speed. The same stations which had a low MAE and low MBE also have high index of agreement with the observations.

In Figure 6.15, time series of both the predicted and observed wind vectors for each station are shown. This plot gives a good idea of correlations between simulated and observed wind speeds as well as the wind directions. From the wind speed analysis it was determined that both the Lake Wheeler and Rocky Mount stations were well represented by the model. The wind vectors reveal the same information and show that the wind direction is also well simulated. On the first day, the wind speed was light because the synoptic forcing was weak. During regimes such as this the wind speed and direction are highly influenced by local scale effect (Avissar and Chen, 1993; Chen and Avissar, 1994a,b; Lynn et al. 1995a). It was hoped that increasing the landuse resolution would allow the model to better resolve these smaller scale influences, but the comparison in Figure 6.15 shows a lot of discrepancy between the model and observation, during this

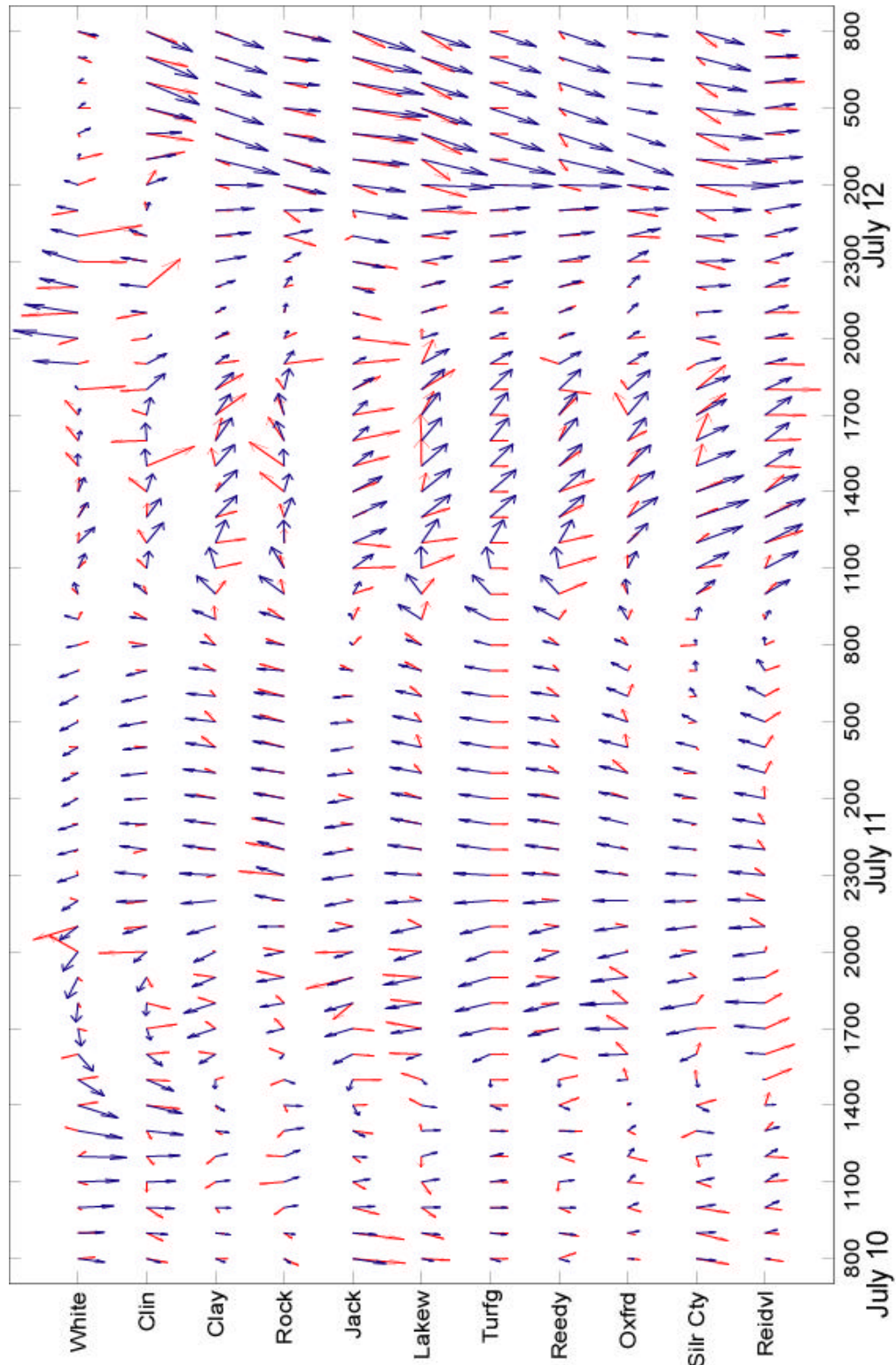


Figure 6.15 Observed and simulated wind vectors, 48 hr time series for all NC ECO Net stations.

free convective period. The light winds are well simulated only in terms of their

magnitude; wind directions differ as much as 180° for many sites.

During the first nighttime period, as the boundary layer becomes stable, the simulated wind direction becomes better correlated with the observations. Stations like Rocky Mount, Lake Wheeler and Reedy Creek are better modeled than Turfgrass and Whiteville. On the second day, both the wind direction and speed are better simulated presumably because the synoptic flow is more prominent. However, there are larger differences in the wind direction. The last 12 hr period of the simulation, when the cool front progresses through the region, the comparison of the wind vectors is very good. It is encouraging that the model depicts this event with a high degree of skill.

6.1 SUMMARY OF REGIONAL SIMULATION

The first case study for the July 10th thru July 12th period, combines several interesting boundary layer scenarios, central to air quality considerations. On the first day (0800 July 10th – 0800 July 11th) the boundary layer is characterized as convective, during the day, where buoyancy driven turbulence is the main contributor to TKE generation. Additionally, it was shown that the boundary layer height was limited to about 1000 m by a strong subsidence inversion. In these situations the wind speed is typically light, cloud cover nonexistent and ozone production maximized. Supporting this, the North Carolina Department of Natural Resource/Division of Air Quality reported a peak in observed ozone on this day.

At night the boundary layer became moderately stable under clear skies and light winds. Surface temperature estimations from the model during the day were consistent with AVHRR satellite images in terms of the warmer and cooler patterns over the region.

The typically warmer Sandhills region and some of the larger urban centers were simulated as warmer surfaces. Turbulence was also higher over these warmer locations. Landuse from the model's perspective has a definite impact on the degree of turbulence as well as the boundary layer height. The boundary layer height over the more convective areas is greater than that over the less convective forest areas. During the first day of this event, the model consistently underestimated the daytime temperature by several degrees while simulating the nighttime temperature better. The wind speed was well simulated during the day for most stations, but the wind direction was off by as much as 180°. Once the boundary layer became stable at night the wind direction better compared to the model results. It is thought that during light wind conditions when the boundary layer is highly convective, the variation in wind direction is greater and more difficult to model.

On the second day of the simulation, 0800 LT July 11th – 0800 LT July 12th, the synoptic flow was more pronounced. Wind speed in the boundary layer was much higher than the first day. This was the main difference between the two days as the cloud cover remains low and surface heating similar. This leads not only to turbulence generation by buoyant convection, but also shear. Again, this type of situation is typically realized in North Carolina during the summer ahead of cold fronts. The model simulated TKE showed stronger turbulent energy on the second day as well as a deeper boundary layer. The boundary layer height directly correlated to the surface heating and associated TKE distribution.

A comparison of simulated 2 m temperatures with the observations on the second day was better than the first day during both the day and night, although the model still contained a cool bias. The wind speed was also better simulated on the second day, as

was the wind direction. The model did a very good job on both the strength and timing of a cool front that passed through the region towards the end of the simulation.

CHAPTER 7

RALEIGH AREA HIGH-RESOLUTION METEOROLOGICAL AND AIR DISPERSION SIMULATIONS

One of objectives of this study is to simulate small-scale variations in the boundary layer, which are not adequately predicted by larger scale meteorological models. The other objective is to use this high-resolution meteorology as the input for pollution dispersion simulations, in order to account for the effect of local-scale features on air dispersion. These goals are exclusively targeted in this final chapter.

First, the landuse parameterization for the 1 km model domain over Raleigh is presented. Then, the 1 km simulated boundary layer meteorology is discussed. This includes an examination of the windfield, turbulence, potential temperature and surface temperature. Model validation is then discussed including a comparison of the simulated wind profiles with SODAR observed profiles. A comparison between statistical model performance indicators of 6 km and 1 km simulations is also presented. Dispersion simulations from the CALPUFF dispersion model are then presented and discussed.

7.1 RALEIGH AREA 1 KM ARPS DOMAIN

Raleigh, North Carolina, is located on the edge of where the Piedmont and Coastal Plain regions intersect. The 1 km model domain is centered over the main urban core of Raleigh and extends to cover most of Wake County including Research Triangle Park, Cary and Garner. In Figure 7.1 the model domain is shown with respect to the ARPS 6 km model domain discussed in the previous chapter. Also, depicted in this figure

are the major roadways of Raleigh. The 440 Beltline outlines the core of Raleigh and is the major roadway of travel around the area. Interstate 40 is another major commute route as is Capital Boulevard. Areas that are highly commercialized are downtown Raleigh, Cary, Research Triangle Park, Capital Boulevard and Garner.

Figure 7.2a presents the terrain specification for the model domain. Across the domain the terrain ranges from just under 50 m to about 140 m. The terrain variation

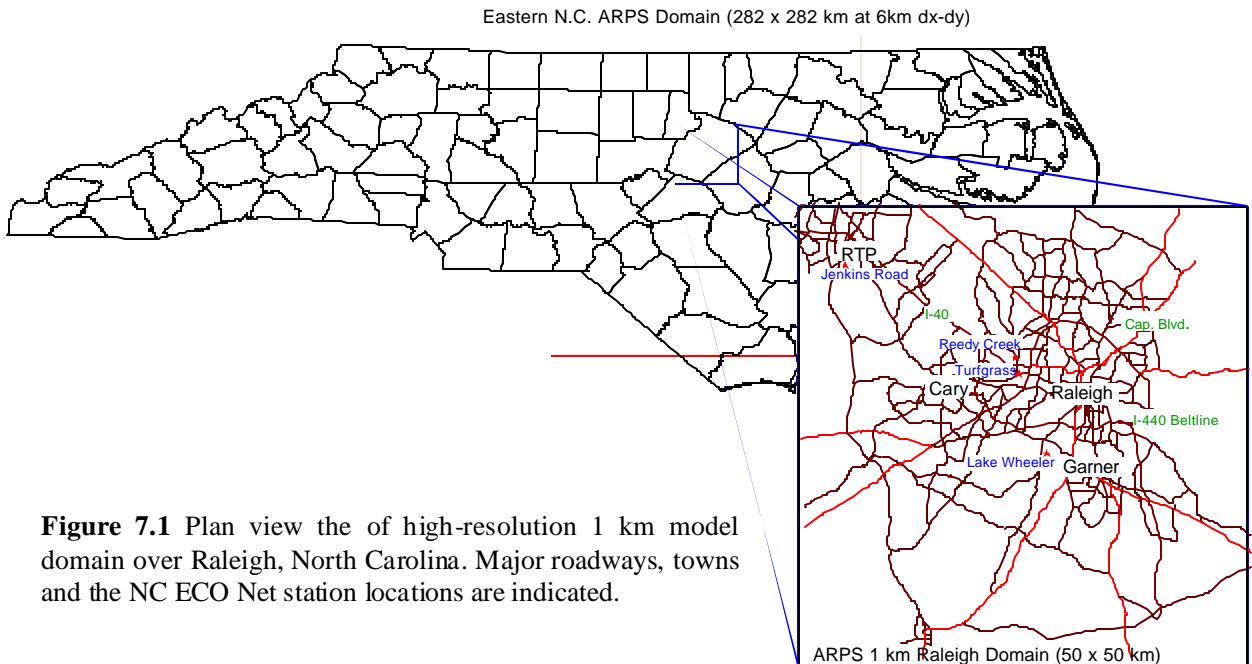


Figure 7.1 Plan view the of high-resolution 1 km model domain over Raleigh, North Carolina. Major roadways, towns and the NC ECO Net station locations are indicated.

indicates several identifiable features. A ridge runs from south to north in the western portion of the Raleigh area. This ridge peaks at 130-140 m and slopes downward to well below 100 m over a distance of 10 km or less. This ridge is of importance from a hydrological perspective because it marks the separation of the two largest river basins in eastern North Carolina. The Neuse River Basins' catchment region is the area to the east of this ridge and the Cape Fear River Basin starts to the west of the ridge. These river basins are easily identifiable in the terrain field. Another feature of interest is the valley that runs from west to east in between the two highest peaks. Over a distance of a few kilometers, the terrain slopes from approximately 130 m to less than 100 m. These areas are mentioned because it will be shown that this relatively small terrain variation influences the simulated meteorology.

Presented in Figure 7.2b is the soil type for the region. Three soil types dominate the model domain: sandy loam, loam and silty loam. The main soil type in the southern part of the domain is sandy loam (light purple). This area represents the border between the Piedmont and Coastal Plain, where the more open areas of the Sandhills region meet the predominately forest areas of the Piedmont. Loamy soil (dark purple) is the primary soil texture in the far western domain where deciduous forests are prevalent. Silty loam soils exist in the central domain.

Vegetation type classification for this area is presented in Figure 7.2c. The western and northern portion of the domain is predominately classified as deciduous forestland (light blue). In the far southern part and along the eastern boundary of the domain, vegetation type is mainly cropland or open fields. The same is true for the area surrounding the main core of Raleigh. ARPS does not have a separate vegetation or soil

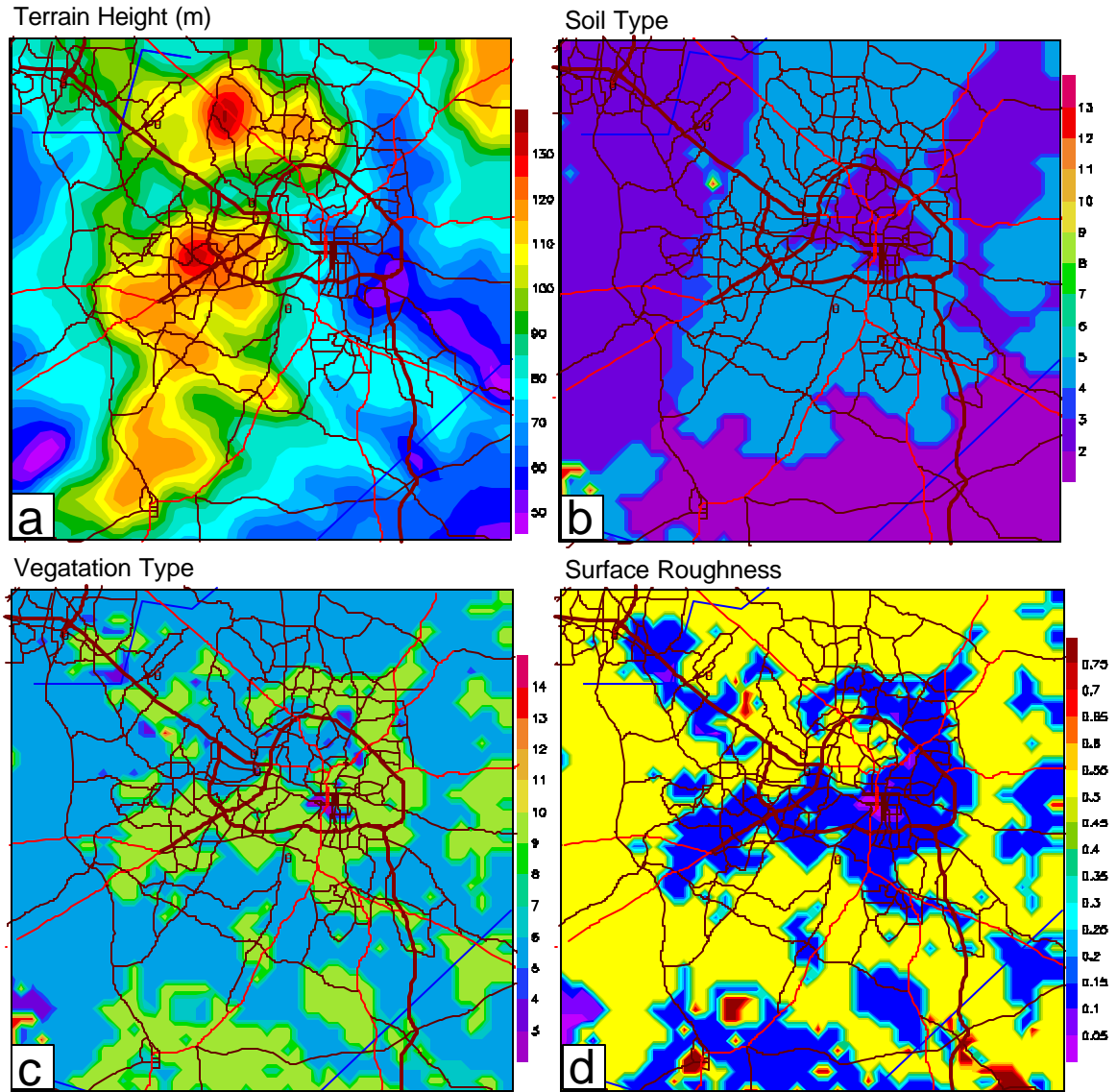


Figure 7.2 Terrain and landuse properties over the Raleigh, North Carolina region as parameterized by ARPS.

classification for urban areas. It improperly classifies the urban area of Raleigh as an open field. It was shown in the previous chapter that this classification does aid in appropriately warming the urban areas relative to surrounding rural areas. However, the problem with this classification is the lowered surface roughness parameterization. For the Raleigh area this presents less of a problem since the urban center does not contain the widespread area of tall buildings like the cities of New York and Saint Louis. Figure

7.2d gives the surface roughness parameterization for the domain. As mentioned in the previous chapter, surface roughness is derived from the vegetation classification. It is seen that around Raleigh, the roughness length is 0.1 m, which corresponds to the open field vegetation type. Deciduous forest areas are assigned a roughness length of 0.55 m while several small patches of mixed deciduous and evergreen forests are 0.75 m.

The diversity in surface characteristics over this small 50 x 50 km area around Raleigh is significant. It is this diversity that will be the main topic in the discussion of the simulated meteorology. The following section presents the meteorology for this case study.

7.2 SIMULATED 1 KM METEOROLOGY

The first analysis time is on the afternoon of the first day (1500 LT on July 10th, 2001). A synoptic overview provided in the previous chapter showed that the pressure gradient was weak at this time. Because of the weak large scale influence the wind speed is light and the wind direction is more controlled by landuse distinctions. Landuse is also more influential on the boundary layer turbulence and boundary layer height. In the 6 km simulations for this same case, it was noticed that the convective boundary layer at this time was mostly dominated by buoyancy-induced turbulence.

Figure 7.3a shows the simulated 10 cm surface temperature at 1500 LT. The surface characterization is easily identifiable by the temperature distribution. The areas classified as open fields, are significantly warmer than the surrounding deciduous forest. Temperatures over the warmest areas are around 38° C while the outlying rural region is a much cooler 29-30° C. AVHRR satellite images presented in the previous chapter

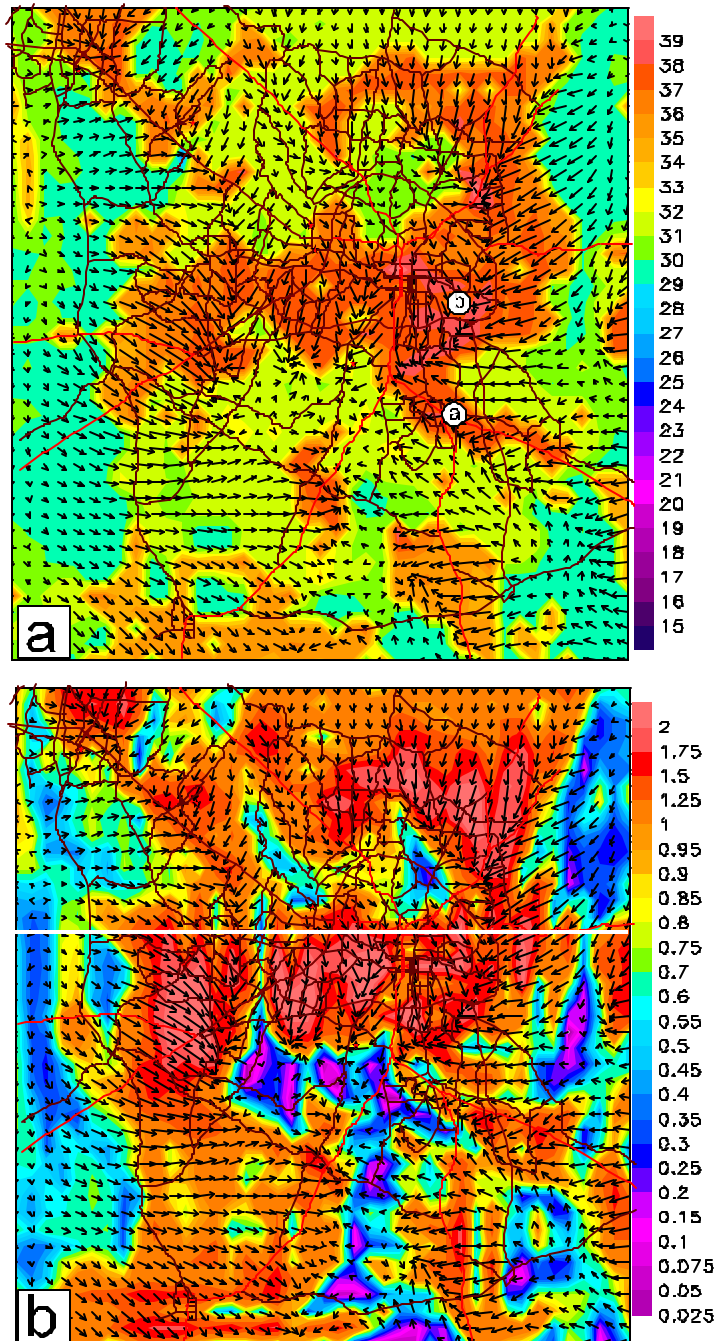


Figure 7.3 (a) Simulated 10 cm surface temperature (C) and 10 m wind vectors. (b) Simulated 100 m TKE (m^2/s^2) and 10 m wind vectors. Both panels are for July 10, 2001 at 1500 LT.

indicated similar strong surface temperature gradients around Raleigh. It must be addressed that AVHRR surface temperature measurements overland are not as accurate

as over homogeneous surfaces like water, but the identification of an urban heat island is somewhat realistic. Other open areas in the southern part of the domain are also simulated much warmer.

The 10 m wind vectors are overlaid on the surface temperature in Figure 7.3a. Surface temperature has a significant impact on the wind field. Area (a) marked on Figure 7.3a signifies a highly commercialized zone in the suburb of Garner. The warmer surface induces greater sensible heat flux in this region. The heat flux gradient present along the surface temperature gradient is causing the local wind to converge on the warmed surface. A noticeable convergence zone exists over the commercialized area. This same convergence zone extends over another area (marked as area (b)) in east Raleigh. The heat flux gradient between this warmed surface and the cooler surface to the east has caused the wind to shift from the cool to warm surface. In fact, complex convergence and divergence patterns exist over the entire domain, all of which appear to be influenced by the surface temperature distribution.

Turbulence energy at 100 m (TKE), associated with this surface temperature variation, is presented in Figure 7.3b. The same 10 m wind field is also shown. High turbulence ($2.0 \text{ m}^2 \cdot \text{s}^{-2}$) exists over the heated urbanized and open field areas. The elevated turbulence corresponds to the locations where the convergence zones lie and where the wind speed is enhanced. Areas where the turbulence is low (less than $0.5 \text{ m}^2 \cdot \text{s}^{-2}$), the wind speed is relatively calm. Overall the turbulence and wind fields depict a highly convective boundary layer where strong thermals develop because of surface heating.

Figure 7.4a shows a west-east cross-section of the boundary layer at 1500 LT with the location shown as a white line on Figure 7.3b. Shown in the cross-section are TKE

(shaded), potential temperature stratification (contoured) and horizontal wind vectors. Most noticeable are the highly turbulent regions associated with the areas of high surface temperature and low-level flow convergence. TKE in these regions is high ($2.0 \text{ m}^2 \cdot \text{s}^{-2}$), while adjacent areas have values less than $0.5 \text{ m}^2 \cdot \text{s}^{-2}$. These turbulent regions are associated with ascending motion and the less turbulent areas in between have downward motion.

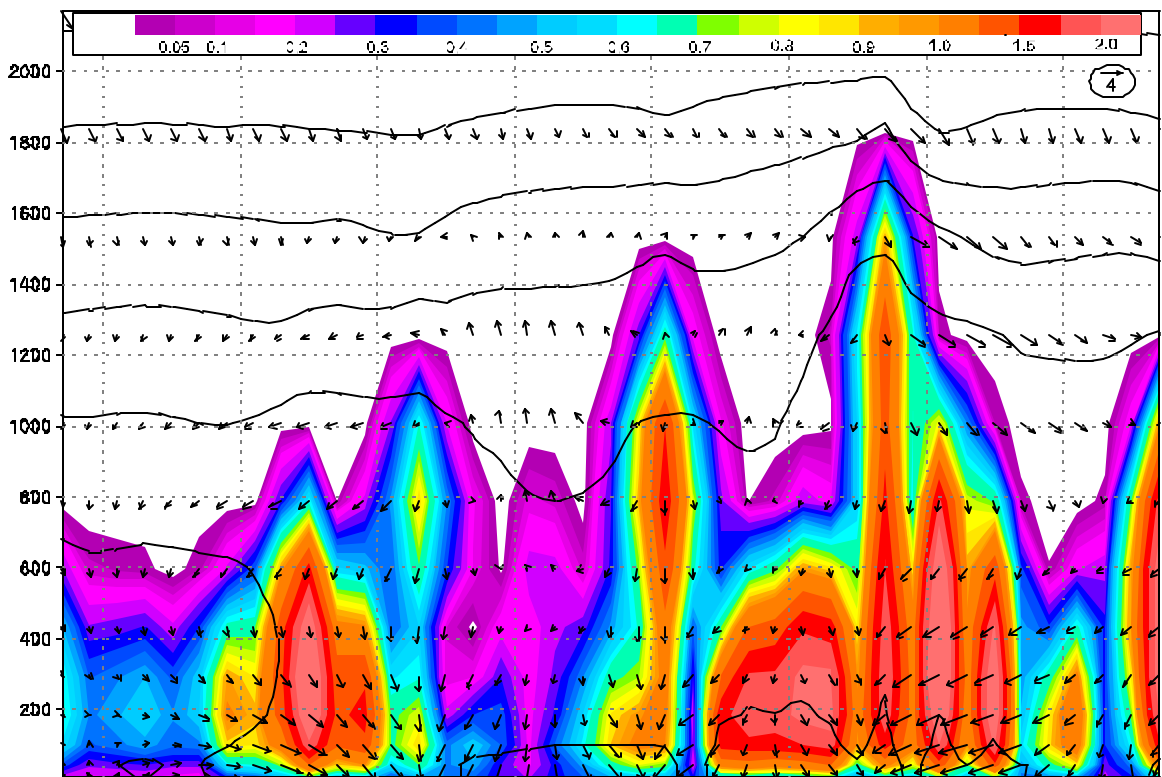


Figure 7.4 Simulated vertical cross-section of potential temperature (contoured each 1 degree), TKE (m^2/s^2) and horizontal wind vectors for July 10, 2001 at 1500 LT for the upper cross-section.

Also, the potential temperature profile correlated well with the convection depicted by the TKE. At the root of the strong turbulent region in the eastern part of the cross-section, an unstable or super-adiabatic potential temperature profile exists in the surface layer. This area is associated with the warmer open areas illustrated in the

previous figure. In the far western section of the cross-section, reduced turbulence is a result of relatively cooler air near the surface, associated with the cooler forested areas. Shown by both the potential temperature and TKE, the boundary layer height is highly variable as a result of spatial variation in surface temperature and heat flux. Over highly turbulent regions where the surface temperatures are greater, the boundary layer height is between 1200 m and 1600 m. Over the less turbulent areas the boundary layer height is as low as 700 m. This figure illustrates the ability of 1 km simulations to explicitly resolve spatial variations of boundary layer height and turbulence (TKE) in response to changes in surface characteristics.

The next analysis is during the early morning of the next day (0500 LT on July 11th, 2001). Figure 7.5a gives the simulated 10 cm surface temperature for this time. Typically, this early morning time is when the surface reaches a minimum temperature. The surface temperature is for the most part, homogeneous (approximately 20°C). Because of this, the terrain influence is more noticeable than landuse. Figure 7.5b shows the elevation with the 10 m wind vectors. It does appear that the terrain is influencing the flow pattern. In general, valley regions have lighter surface wind speeds, particularly the west-east valley between the two higher peaks. Over the higher areas the wind speed is on the order of 4 m·s⁻¹ while in the valley the wind is less than 1.0 m·s⁻². This variation is likely a result of slope flow of cooler air into the valley, increasing the stability of the nocturnal boundary layer. The wind speed and direction seem to be modified along the stronger terrain gradients. Areas along the ridge slopes show the wind direction diverging from higher to lower elevations. For example, on the western boundary of the main ridge, the wind backs from the northwest down the terrain gradient while over the ridge the

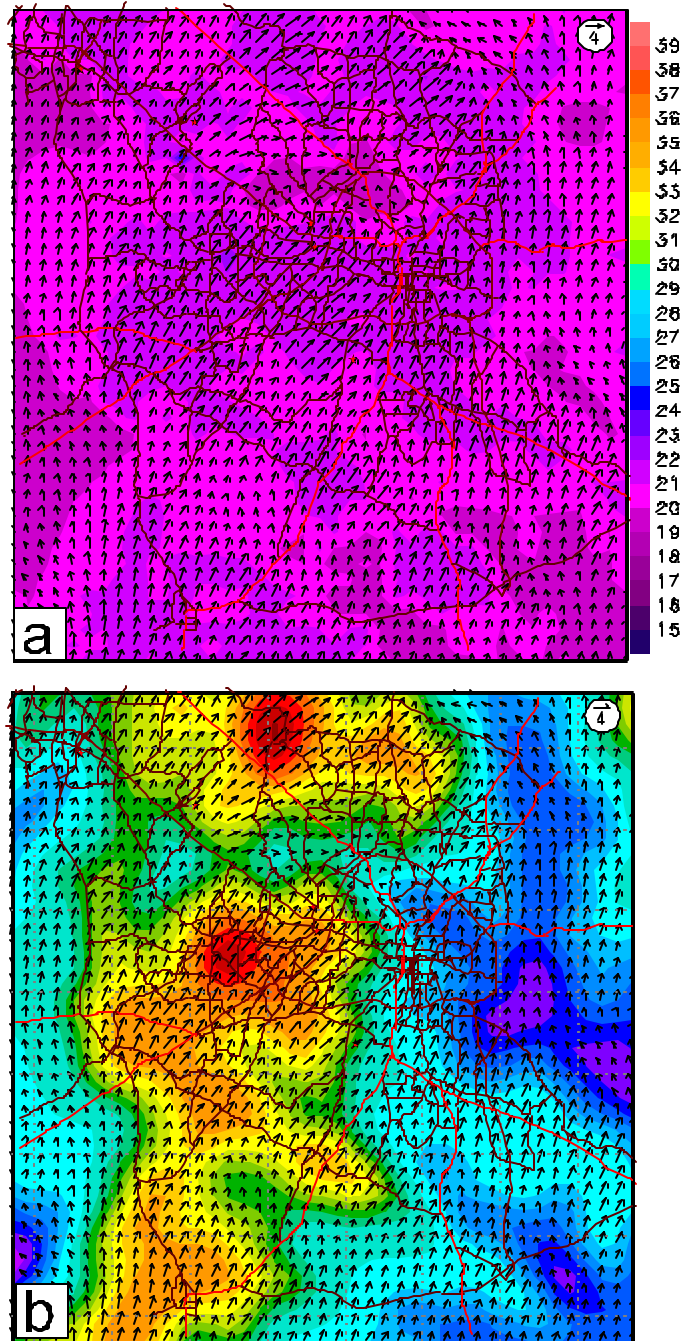


Figure 7.5 (a) Simulated 10 cm surface temperature ($^{\circ}\text{C}$) and 10 m wind vectors. (b) Terrain height (m) and 10 m wind vectors. Both panels are for July 11, 2001 at 0500 LT.

wind is southwesterly. Even maintenance though the topography in the domain is not that significant when compared to mountainous regions, the model does show sensitivity to

even slight terrain variations.

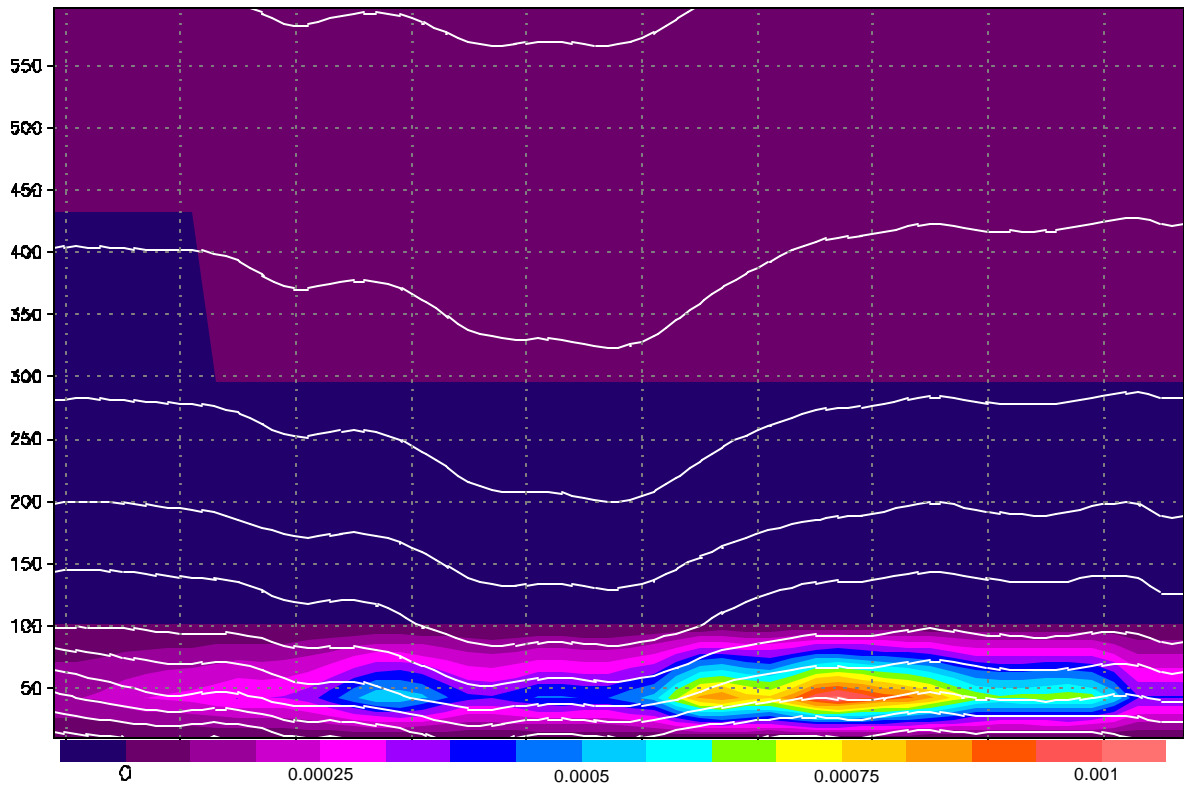


Figure 7.5 (c) TKE ($m^2 \cdot s^{-2}$) and potential temperature (each 1 K) vertical cross-section through the center of the 1 km model domain at 0500 LT on July 11th, 2001.

Figure 7.5c shows a vertical cross-section of simulated TKE (shaded) and potential temperature (contoured each 1 K), west to east through the center of the domain. The profile reveals that the turbulence is very low near the surface, on the order of $0.001 m^2 \cdot s^{-2}$. Additionally, the TKE distribution points to a stable boundary layer height of 75-100 m, which is similar to the SODAR reflectivity record shows in Figure 7.10. It is also noticed that the potential temperature profile indicates a strong statically stable layer below 100 m while the static stability lessens between 100-300 m and then becomes near-

neutral above 400 m. In the SODAR record (Figure 7.10), strong reflectivity correlates well with the strong temperature stratification below 100 m.

The next day, as illustrated by the 6 km simulation, is characterized differently from a boundary layer structure standpoint. Free convection was shown to dominate during the first day. On the second day, the larger scale pressure gradient increases, as do the associated boundary layer winds. It is during this period when shear-induced turbulence in the boundary layer becomes a significant generator of turbulence.

Figure 7.6a presents the surface temperature and 10 m wind speed at 1400 LT on July 11, 2001. A similar temperature pattern is noticed when compared to the previous day (Figure 7.3a). Again, the urbanized areas parameterized as open fields with little vegetation are much warmer (37-39° C) than the highly vegetative forest regions (30° C). As a result, the wind field is modified as the air is transported over these regions. Unlike the previous case, however, a preferred wind direction is established by the stronger boundary layer flow. Still, convergence zones are induced along surface temperature gradients, parallel to the large-scale flow. The convergence pattern (marked as area (a)) is indicative of a horizontal roll structure, typically seen when strong boundary layer flow exists over a warm surface. Figure 7.6b gives the 100 m TKE and 10 m wind vectors for the same time. Higher turbulence is more widespread than the previous day. The stronger boundary layer wind speed is the likely reason for this difference. Convergence zones, possibly associated with the horizontal roll features are more turbulent. In the eastern section of the domain, on the downwind side of the warmer urban area, divergence is noticed in the wind field. As expected, the areas of divergence or downward motion are less turbulent.

Figure 7.7 is a west-east cross-section of TKE, potential temperature and horizontal wind, through the center of the domain. The exact location is illustrated as a

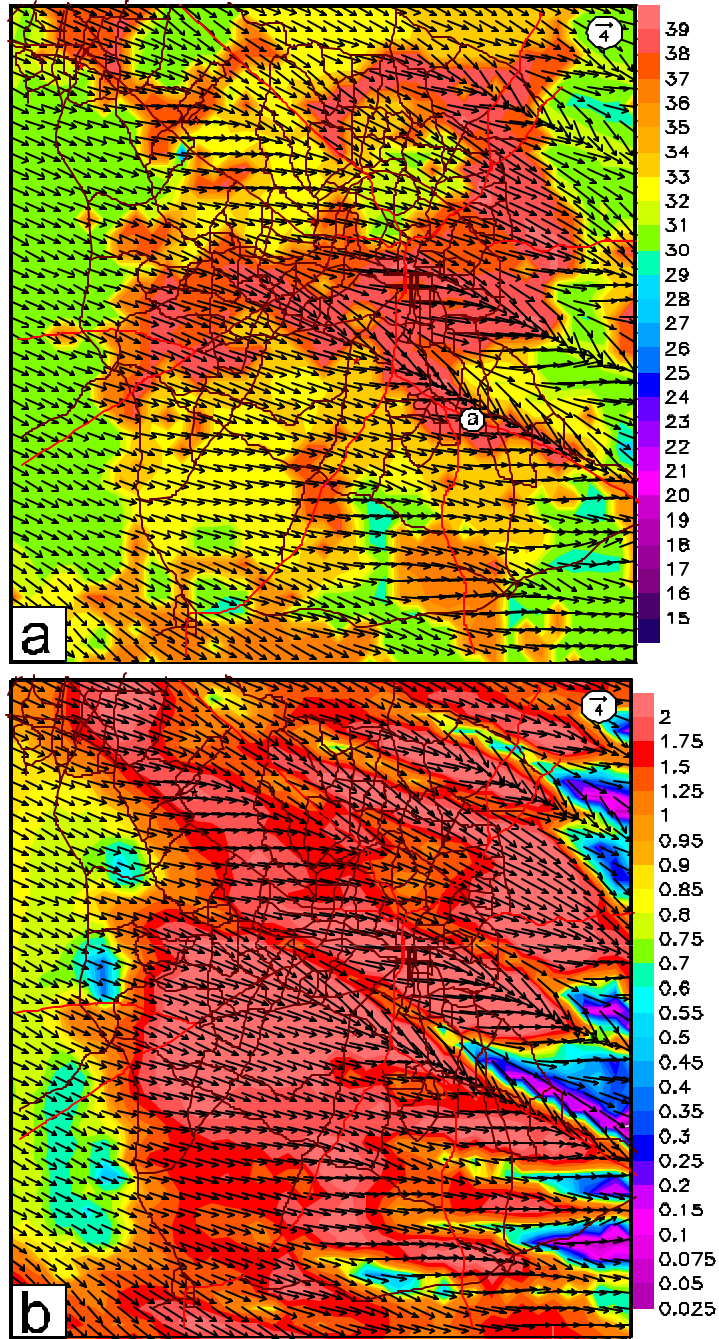


Figure 7.6 (a) Simulated 10 cm surface temperature (C) and 10 m wind vectors. (b) Simulated 100 m TKE (m^2/s^2) and 10 m wind vectors. Both panels are for July 11, 2001 at 1400 I.T.

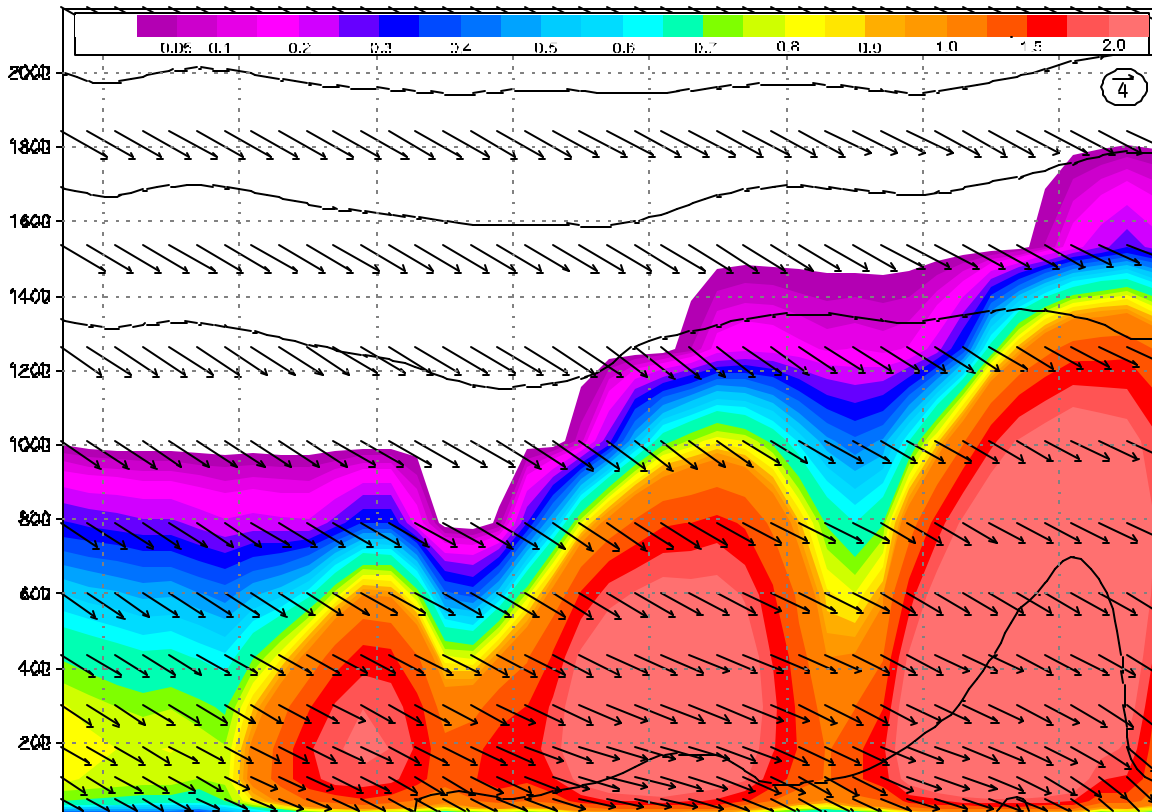


Figure 7.7 Simulated vertical cross-section of potential temperature (contoured each 1 degree), TKE (m^2/s^2) and horizontal wind vectors for July 11, 2001 at 1400 LT for the upper cross-section.

white line in Figure 7.6b. A much different vertical boundary layer structure is evident. For one, the boundary layer wind is nearly homogeneous in both speed and direction. The boundary layer height varies significantly, between 1000 m in the western to 1600 m in the eastern part of the cross-section, as depicted by the TKE distribution.

The potential temperature stratification indicates an increasingly deeper super-adiabatic layer near the surface from west to east. Turbulence does show significant variation. This cross-section intercepts three of the convergence zones noticed in the previous figure. Turbulence within these convergence areas is twice as strong as in the subsidence areas between. Turbulence increases to a maximum within 100 m above the surface, indicating that shear induced turbulence is significant. On the previous day, TKE

reached a maximum at a higher altitude (200-300 m) in the boundary layer, indicating a boundary layer dominated by free-convection.

The final analysis is presented for the morning of July 12th, 2001 at 0500 LT. Indicated in the analysis of the 6 km simulation, around this same time period, a summer time cool front backed in from the northeast. The simulated surface 10 cm temperature and 10 m wind speed are shown in Figure 7.8a. Like the previous morning, surface temperature does not vary significantly over the region (20-22° C). Terrain variation and possibly some influence from the slightly warmer surface over the southwestern domain, appear to have the dominating influence on the 10 m wind. Figure 7.8b shows the underlying elevation with respect to the 10 m wind. In the lower lying areas, the wind speed is less than that over other higher areas. In the valleys the wind speed is on the order of 1-2 m s^{-1} , while over elevated areas the wind speed is as much as 6 m s^{-1} . It is also noticed that the wind direction appears to diverge around the higher terrain. Again, the model simulations seem to be sensitive to not only surface characteristics but also terrain variations during stable conditions.

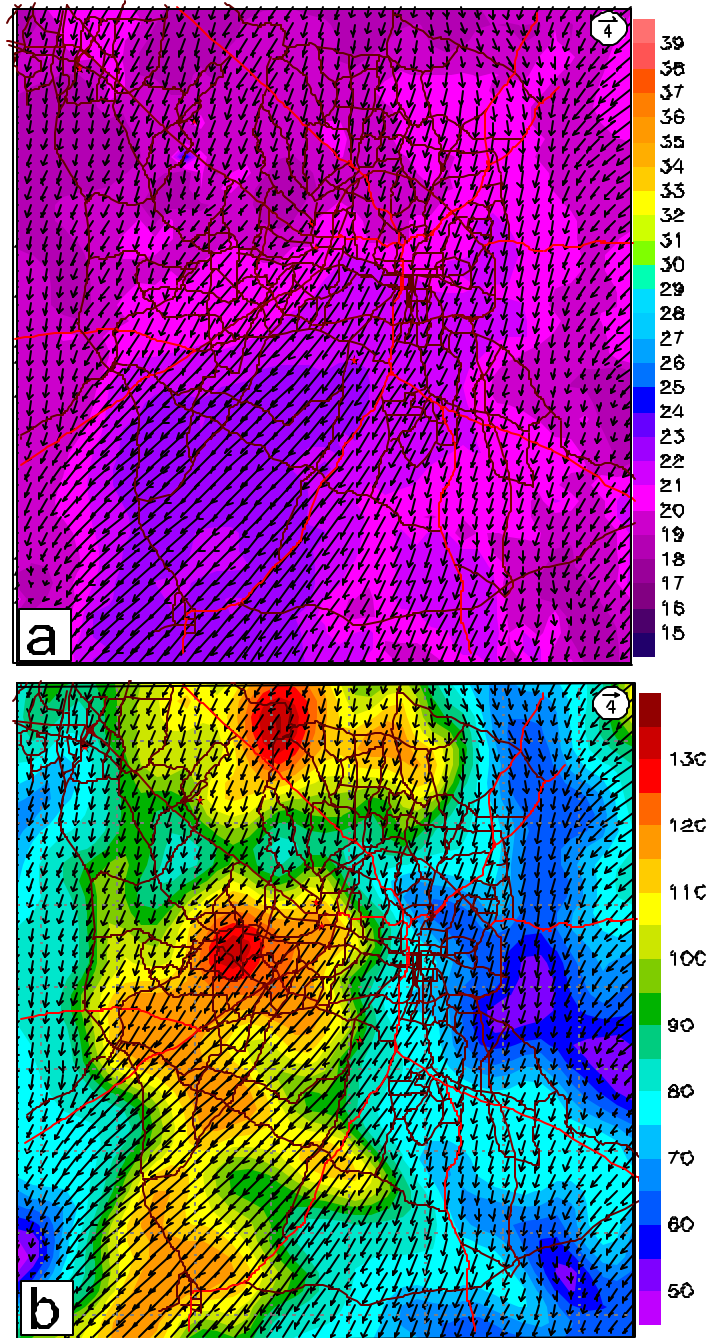


Figure 7.8 (a) Simulated 10 cm surface temperature (C) and 10 m wind vectors. (b) Terrain height (m) and 10 m wind vectors. Both panels are for July 12, 2001 at 0500 LT.

7.3 COMPARING SIMULATED METEOROLOGY WITH OBSERVATIONS

In Figure 7.9, the Digital Facsimile Data (DFS) from the Model 2000 SODAR is plotted for the 48 hr period of the simulation. DFS data is synonymous with the SODAR sound reflectivity, which directly correlates to the strength of the returned sound signal. Typically, DFS data is used to distinguish the depth of the boundary layer as well as boundary layer turbulent structures. Overlaid on the DFS data is the simulated potential temperature profile at the closest grid point to the SODAR location. The DFS data is available to a height of 600 m while the simulated potential temperature is plotted from the surface to 1 km.

As shown in the upper panel of Figure 7.9, from left to right, the boundary layer height begins to grow at 0800 LT from approximately 200 m until it extends out of the range of the SODAR, around midday. The potential temperature stratification for the first few hours is well correlated with the estimated boundary layer growth observed by the SODAR. The simulated slope of growth also appears to match that of the DFS data. The DFS data reveals a convective boundary layer between 1100 LT and approximately 1800 LT. Discrete convective plumes are seen in the DFS data as brief strong spikes in the reflectivity. During this time the simulated potential temperature distribution indicates a super-adiabatic layer below 50 m; a needed ingredient for convective instability such as that seen in the SODAR data. The convective activity in the DFS data appears to decline after 1600 LT. Correlating to this, the simulation shows that surface heating has already peaked by this time and the boundary layer has reached a state of equilibrium. In the simulated potential temperature distribution, the surface is shown to begin cooling around 1830 LT. At this time the boundary layer collapses in a rapid transition from convective

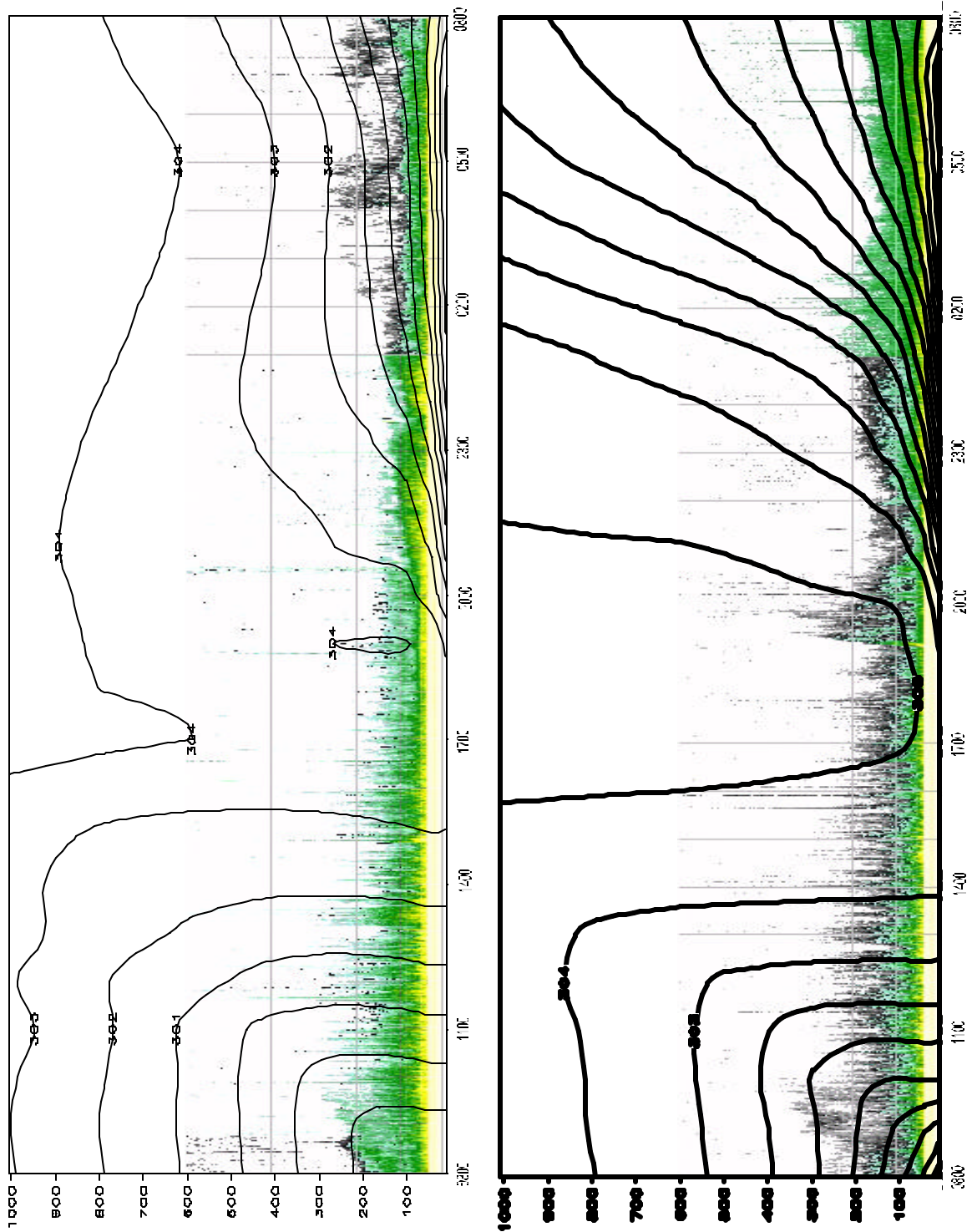


Figure 7.9 Aerovironment Model 2000 SODAR observed reflectivity (dB) for July 10, 2001 (0800 LT) to July 12, 2001 (0800 LT). Simulated potential temperature is contoured (K) each 1 degree for the corresponding period.

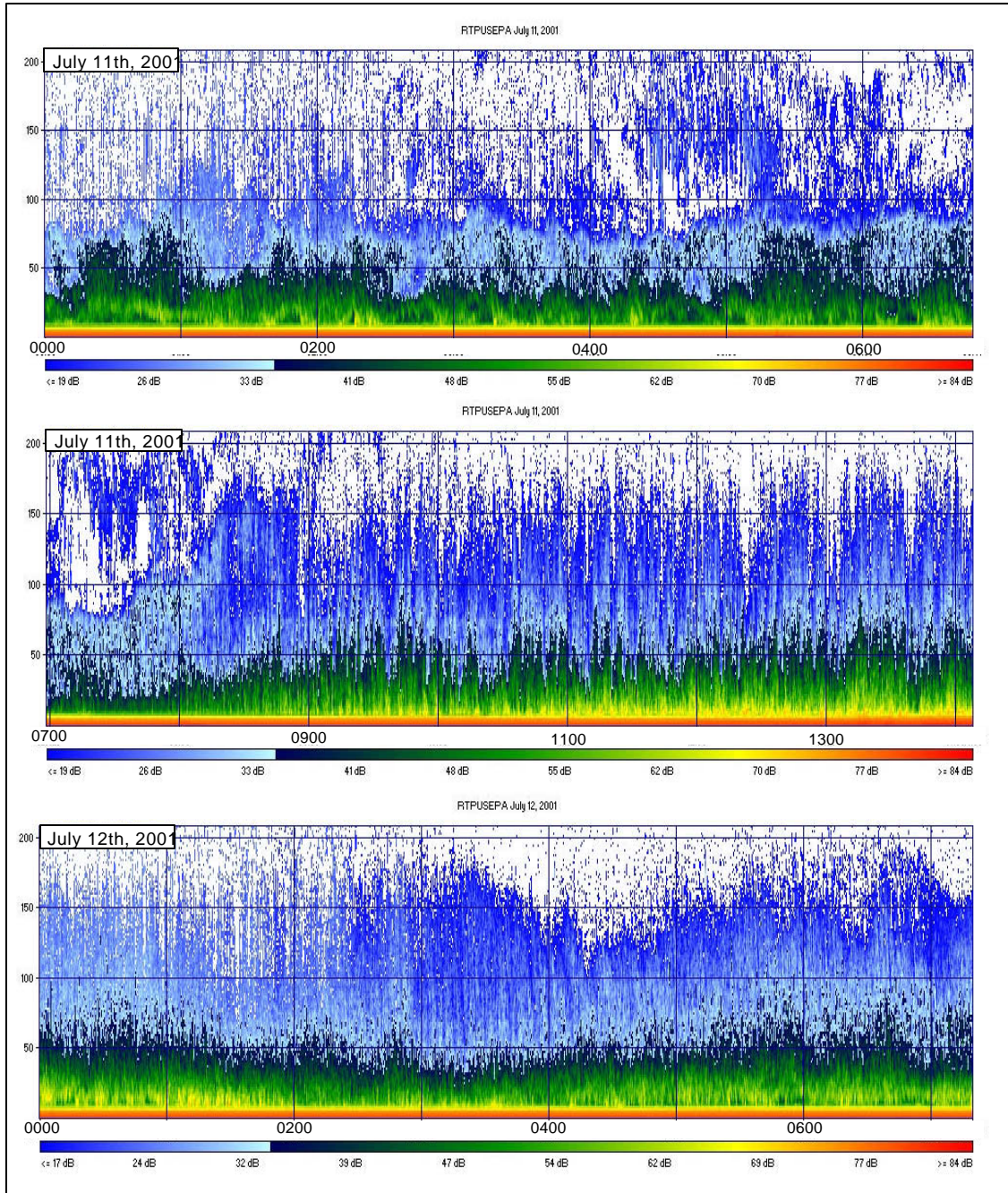
to stable condition. Around the same time, the DFS data reveals stabilization of the lower

boundary layer.

The boundary layer height at 2030 LT as measured by the SODAR data, is well defined with a value of about 100 m. The potential temperature profile is consistent with this observation. A residual layer is noticed in the potential temperature between 100 m and 900 m. This decaying mixed layer reflects less sound energy, unlike the thermally stratified stable boundary layer. During the night, the simulated potential temperature profile points towards a deepening nocturnal boundary layer, from 100 m at sunset to approximately 250 m at sunrise the following morning. It can be seen that throughout the night, the simulated potential temperature compares reasonably well with the observed SODAR reflectivity. Strong static stability is simulated in a layer from the surface to about 100 m. Within this layer is where the SODAR senses stronger return signals while above this layer, between 100 m and 300 m, the SODAR reflectivity is less but still significant. The upper layer is simulated as stable but the static stability is less than that at the surface.

The top panel in Figure 7.10 presents the DFS data from the Model 4000 miniSODAR for the morning of July 11th, 2001. The miniSODAR provides higher resolution measurements below 200 m. The DFS data in this figure is comparable to the same data from the Model 2000 SODAR. Between midnight and 0700 LT the boundary layer depth of 100 m is easily identified as the higher reflectivity region. Shear induced mixing at the top of the boundary layer, specifically between 0100-0200 LT and just after 0500 LT, are noticed as higher reflectivity regions. The most stable observed portion of the nocturnal boundary layer exists below 50 m. In Figure 7.9 the simulated potential temperature is most statically stable over this same depth.

Figure 7.10 Aerovironment Model 4000 miniSODAR observed reflectivity for July 10, 2001 (0800 LT) to July 12, 2001 (0800 LT).



During the next 24 hr cycle, the DFS data compares well with the simulated potential temperature pattern (Figure 7.9). The boundary layer quickly becomes

convective by mid-morning. The simulated potential temperature profile is somewhat delayed in this growth but does indicate a highly convective boundary layer through 1700-1800 LT. MiniSODAR DFS data from 0700 to 1400 LT is shown in the center panel of Figure 7.10. The miniSODAR indicates the rapid boundary layer growth at 0800 LT. Also seen in this figure are the convective structures near the surface beginning at 0900 LT.

The simulated potential temperature profile in Figure 7.9 indicates a stable boundary layer developing at approximately 1800 LT. The DFS data suggest that the boundary layer becomes stable at around 2000 LT. During the night, between 2000 LT and 0800 LT, the simulated potential temperature and DFS estimated boundary layer heights are well correlated. Specifically, between 2100 LT and 0100 LT the simulated layer of higher static stability directly relates to the layer of observed high reflectivity. The depth of this layer is approximately 200 m. In the early morning, between 0100 and 0300 LT a disturbance or weakness in the stability is noticed in the DFS data. This corresponds to the cool front, which was simulated, moving through the region at around this same time. It must be indicated that the simulated disturbance was not as noticeable as it was in areas south of Raleigh. Figure 7.8b shows the terrain and 10 m wind speed around this same time. Referring to this figure, the disturbance is most noticed over the higher elevation areas to the southeast of the SODAR site. It is likely that the boundary layer was more stable over the SODAR site so that the frontal passage is not as apparent at the surface. Figure 7.10 gives the miniSODAR observation for this time, from 0000 LT to 0730 LT on July 12th. Between 0000 LT and 0230 LT the DFS data shows a more mixed structure when compared to the time period between 0300 LT and 0700 LT. The

boundary layer becomes less stable and better mixed as the weak front moves past the Jenkins Road site.

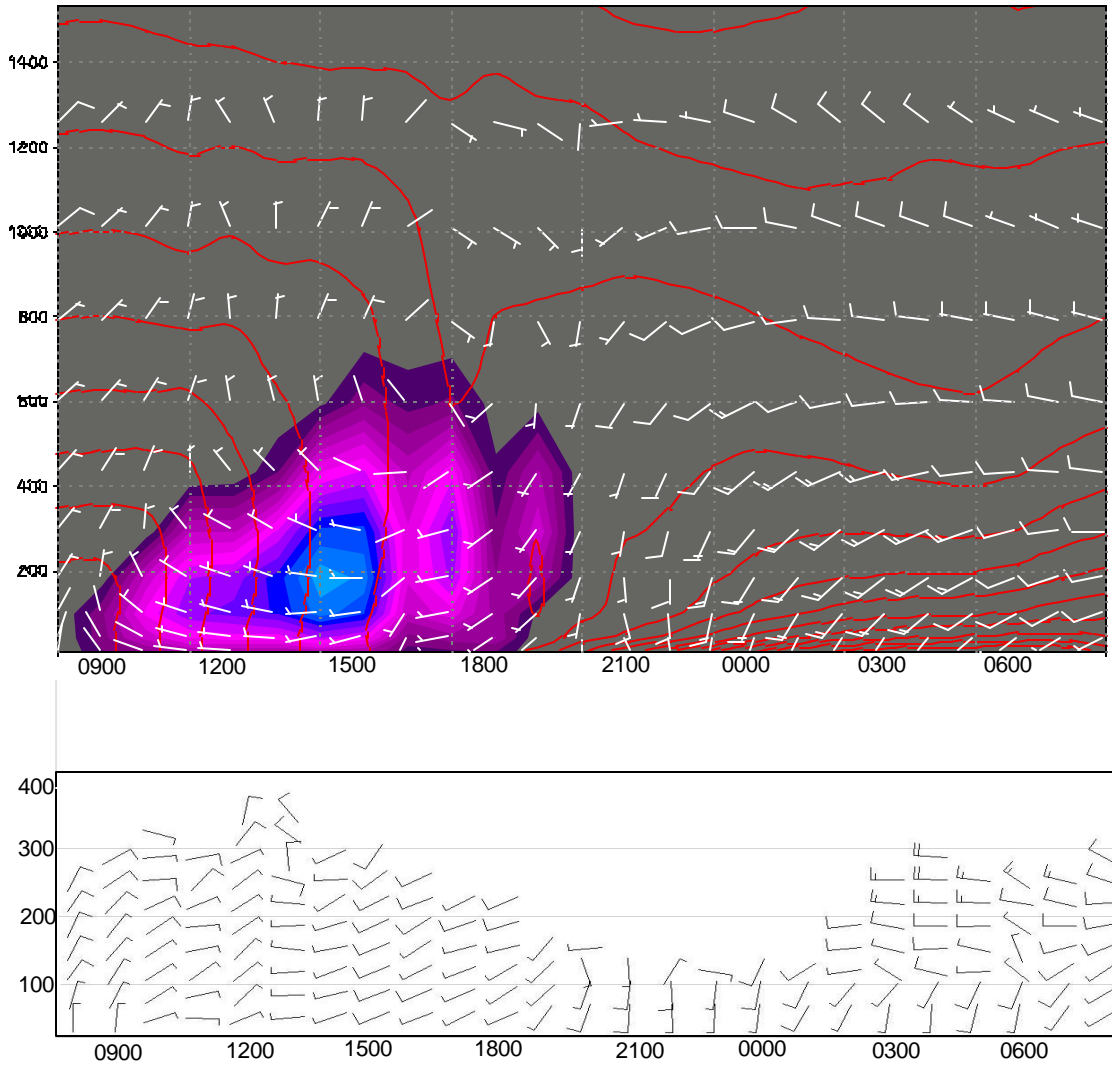


Figure 7.11 Simulated potential temperature (contoured 1 degree), TKE (shaded) and wind (kt) profile (upper). Aerovironment Model 2000 observed wind profile (kt) for July 10, 2001 (0800 LT) to July 11, 2001 (0800 LT).

The next two figures (Figure 7.11 and Figure 7.12) present time series of the simulated wind profiles, potential temperature and TKE from the closest grid point to the SODAR site. Corresponding to these simulated time series, the SODAR (Model 2000) observed wind profiles are shown in the panel beneath the simulated. The simulated time-

series profile extends to 1400 m while the SODAR wind observations extend to 400 m. Figure 7.10 presents the results from the first 24 hrs.

For the first few hours (0800-0900 LT) on the morning of July 10th, the observed wind speed (kt) and direction are consistent with the simulated profile. Near the surface up to 400 m the wind is from the north-northeast at around 5-10 kt, remaining practically constant until about 1200 LT. At this time a wind shift from north-northeast to west takes place. The simulated wind profile shows this same shift in wind direction, however, the shift occurs several hours early at about 1000 LT. Over the remainder of the daytime (1300-1800 LT), the wind remains fairly constant from the west at 5 kt or less. During this time the simulated and observed wind profiles are practically the same. After 1800 LT, a shift in wind direction, from westerly to southerly, is noticed in both profiles. The wind speed is also similar, holding steady at 5 kt. Beginning at midnight (0000 LT), the wind direction shifts to southwesterly in both the simulated and observed profiles. The simulated wind speed just above the surface is stronger (15 kt) than the observed.

Towards daybreak at around 0600 LT the comparison between the simulated and observed wind profiles is more consistent than earlier in the morning. Figure 7.12 presents the same type of comparison for the final 24 hr period of the simulation. Between 0800 and 1500 LT both profiles show a similar west to west-northwest flow at between 5 and 10 kt, from the surface to around 400 m. Some variations in the observed wind direction are noted between 1600 and 2100 LT. This variation is not simulated well by ARPS.

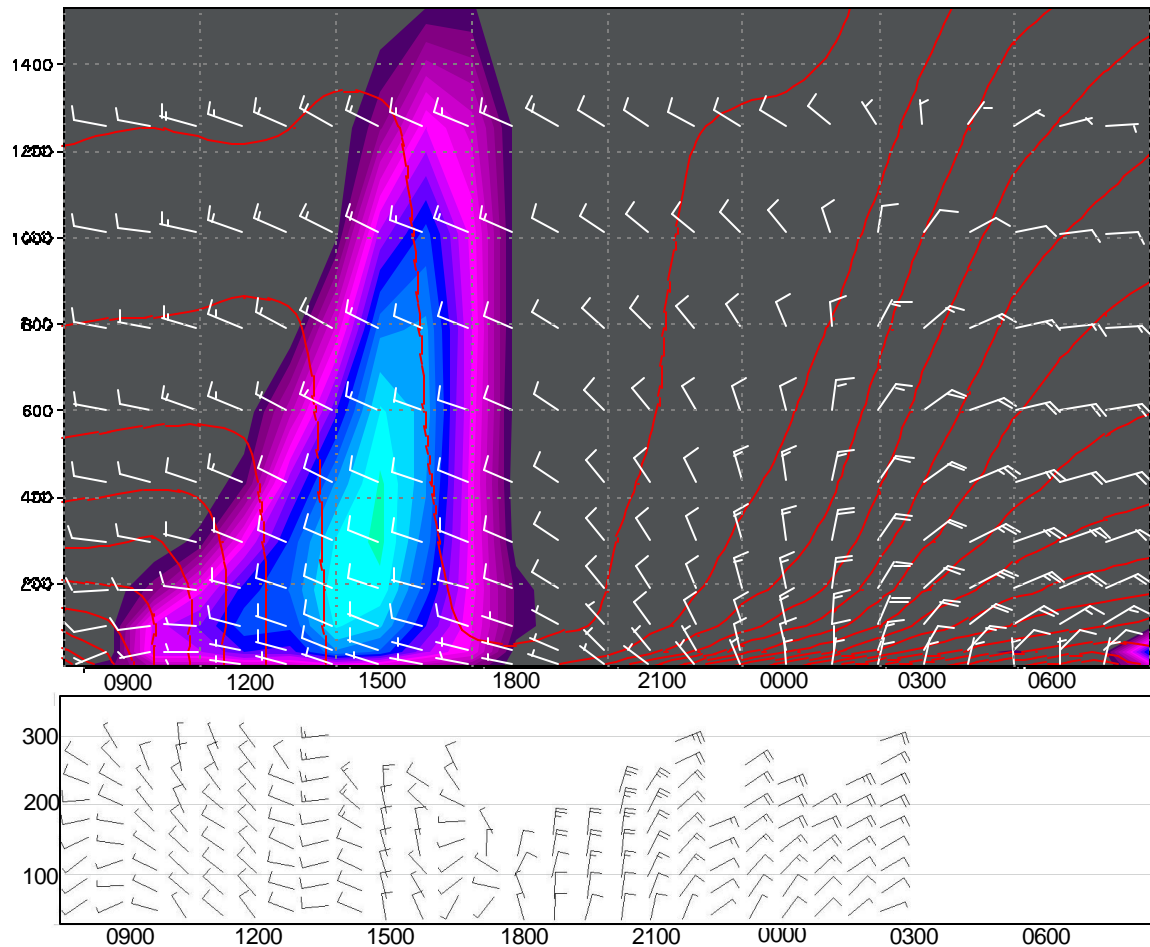


Figure 7.12 Simulated potential temperature (contoured 1 degree), TKE (shaded) and wind (kt) profile (upper). Aerovironment Model 2000 observed wind profile (kt) for July 11, 2001 (0800 LT) to July 12, 2001 (0800 LT).

During the following night, a comparison of the simulated and observed wind is much better. Both profiles show northerly winds of 5-10 kt near the surface increasing to 15 kt above 200 m. This area of stronger wind correlated well with the DFS derived boundary layer height and a nocturnal jet feature. The cool front simulated in both the 6 km and 1 km simulations and noticed in the DFS data is well depicted by both profiles in Figure 7.12. Just after midnight, specifically between 0100-0300 LT, the wind shifts from northerly to northeasterly. At the same time the wind speed increases from 15 kt to 20 kt

at the top of the nocturnal boundary layer. For the final few hours of the simulation the model values remain well correlated with the SODAR wind profile.

For the 6 km simulation, model projections of wind speed, direction and temperature were compared to observations in the region. In the 1 km domain, three of these NC ECONet surface meteorological stations exist: Lake Wheeler, Turfgrass, Reedy Creek and the EPA's Jenkins Road station. The following discussion compares various model performance indicators of the 6 km simulation to those of the 1 km simulation. Table 7.1 presents the model performance statistics for 10 m winds for both the 1 km simulation and Table 7.2 presents the same for the 6 km simulation. Mean bias error (MBE in $\text{m}\cdot\text{s}^{-1}$) for the 1 km case is more biased towards higher wind speeds than the 6 km simulation. For all stations the model bias increases between the 6 km and 1 km simulations. At Lake Wheeler the bias increases from $0.06 \text{ m}\cdot\text{s}^{-1}$ to $0.36 \text{ m}\cdot\text{s}^{-1}$, Reedy Creek from $0.66 \text{ m}\cdot\text{s}^{-1}$ to $0.78 \text{ m}\cdot\text{s}^{-1}$, Turfgrass from $0.75 \text{ m}\cdot\text{s}^{-1}$ to $0.1.36 \text{ m}\cdot\text{s}^{-1}$ and Jenkins Road from $0.93 \text{ m}\cdot\text{s}^{-1}$ to $1.01 \text{ m}\cdot\text{s}^{-1}$. Looking at the day versus nighttime biases reveals that the bias increase has more contribution from higher daytime wind speeds. The average bias of all the stations during the day rises from $0.24 \text{ m}\cdot\text{s}^{-1}$ in the 6 km case to $0.72 \text{ m}\cdot\text{s}^{-1}$ in the 1 km case, while the nighttime average bias remains similar ($0.93 \text{ m}\cdot\text{s}^{-1}$ to $0.99 \text{ m}\cdot\text{s}^{-1}$).

Contrary to the MBE, the mean average error (MAE) is not as much influenced by the scale change. The average error for all four stations was $0.89 \text{ m}\cdot\text{s}^{-1}$ for the 6 km simulation and $0.99 \text{ m}\cdot\text{s}^{-1}$ for the 1km. Again, the increase in average error is more noticed during the day ($0.74 \text{ m}\cdot\text{s}^{-1}$ to $0.91 \text{ m}\cdot\text{s}^{-1}$) than at night ($1.02 \text{ m}\cdot\text{s}^{-1}$ to $1.04 \text{ m}\cdot\text{s}^{-1}$). In line with the above statistics, the index of agreement is less in the 1 km case. It is

Table 7.1 Performance statistics of the high resolution 1 km simulated and observed 10 m wind speed including Mean Bias Error (MBE), Variance (VAR), Root Mean Square Error (RMSE), Mean Absolute Error (MAE) and Index of Agreement (IOA). All indicate over the entire time series, Day indicates statistics between 0800 LT and 1900 LT, Night indicates between 2000 LT and 0700 LT. Avg. All is the average statistic of all stations.

1 km Stats	Obs Sta.	LakeW	Reedy	TurfG	JenkR	Avg. All
	All	0.36	0.78	1.38	1.01	0.88
MBE	Day	0.27	0.69	1.16	0.78	0.72
	Night	0.44	0.80	1.56	1.18	0.99
	All	0.48	0.48	1.03	0.50	0.62
VAR	Day	0.27	0.69	1.16	0.78	0.72
	Night	0.36	0.30	0.51	0.20	0.34
	All	0.77	1.04	1.71	1.23	1.19
RMSE	Day	0.82	1.01	1.68	1.12	1.16
	Night	0.73	0.96	1.71	1.26	1.17
	All	0.61	0.86	1.41	1.09	0.99
MAE	Day	0.65	0.84	1.22	0.94	0.91
	Night	0.59	0.82	1.56	1.18	1.04
	All	0.80	0.62	0.45	0.47	0.59
IOA	Day	0.79	0.72	0.47	0.39	0.59
	Night	0.80	0.30	0.41	0.33	0.46

Table 7.2 Performance statistics of the 6 km simulated and observed 10 m wind speed including Mean Bias Error (MBE), Variance (VAR), Root Mean Square Error (RMSE), Mean Absolute Error (MAE) and Index of Agreement (IOA). All indicate over the entire time series, Day indicates statistics between 0800 LT and 1900 LT, Night indicates between 2000 LT and 0700 LT. Avg. All is the average statistic of all stations.

6 km Stats	Obs Sta.	LakeW	Reedy	TurfG	JenkR	Avg. All
	All	0.06	0.66	0.75	0.93	0.60
MBE	Day	-0.20	0.33	0.37	0.44	0.24
	Night	0.33	0.94	1.12	1.35	0.93
	All	0.45	0.65	1.12	0.84	0.76
VAR	Day	0.48	0.42	1.03	0.99	0.73
	Night	0.31	0.67	1.00	0.21	0.55
	All	0.67	1.04	1.29	1.30	1.07
RMSE	Day	0.71	0.72	1.06	1.07	0.89
	Night	0.63	1.23	1.49	1.43	1.19
	All	0.55	0.83	1.00	1.18	0.89
MAE	Day	0.61	0.63	0.75	0.94	0.74
	Night	0.51	0.98	1.24	1.35	1.02
	All	0.87	0.59	0.52	0.39	0.59
IOA	Day	0.86	0.81	0.67	0.39	0.68
	Night	0.87	0.36	0.42	0.33	0.49

believed that the highly convective conditions on the first day may have a lot to do with the poor wind speed prediction. In addition, the land use properties are likely not

Table 7.3 Performance statistics of the high resolution 1 km simulated and observed 2 m temperature including Mean Bias Error (MBE), Variance (VAR), Root Mean Square Error (RMSE), Mean Absolute Error (MAE) and Index of Agreement (IOA). All indicate over the entire time series, Day indicates statistics between 0800 LT and 1900 LT, Night indicates between 2000 LT and 0700 LT. Avg. All is the average statistic of all stations.

1 km Stats	Obs Sta.	LakeW	Reedy	TurfG	JenkR	Avg. All
	All	-0.12	-0.60	-0.98	-0.72	-0.60
MBE	Day	-1.24	-0.95	-0.96	-1.16	-1.08
	Night	1.03	-0.22	-1.00	-0.27	-0.12
	All	3.56	2.92	2.49	1.43	2.60
VAR	Day	3.18	2.15	2.32	0.72	2.09
	Night	1.53	3.64	2.87	1.86	2.48
	All	1.87	1.79	1.84	1.38	1.72
RMSE	Day	2.14	1.72	1.77	1.43	1.77
	Night	1.59	1.88	1.94	1.36	1.69
	All	1.51	1.59	1.59	1.18	1.47
MAE	Day	1.93	1.54	1.58	1.28	1.58
	Night	1.13	1.66	1.62	1.10	1.38
	All	0.94	0.94	0.93	0.97	0.95
IOA	Day	0.86	0.90	0.90	0.93	0.90
	Night	0.89	0.83	0.83	0.92	0.87

Table 7.4 Performance statistics of the 6 km simulated and observed 2 m temperature including Mean Bias Error (MBE), Variance (VAR), Root Mean Square Error (RMSE), Mean Absolute Error (MAE) and Index of Agreement (IOA). All indicate over the entire time series, Day indicates statistics between 0800 LT and 1900 LT, Night indicates between 2000 LT and 0700 LT. Avg. All is the average statistic of all stations.

6 km Stats	Obs Sta.	LakeW	Reedy	TurfG	JenkR	Avg. All
	All	-0.41	-1.02	-0.99	-0.93	-0.84
MBE	Day	-1.04	-1.10	-0.69	-1.14	-0.99
	Night	0.25	-0.92	-1.28	-0.74	-0.67
	All	2.41	1.57	1.56	1.58	1.78
VAR	Day	2.81	1.60	1.76	0.75	1.73
	Night	1.33	1.65	1.32	2.46	1.69
	All	1.59	1.61	1.59	1.56	1.58
RMSE	Day	1.94	1.66	1.47	1.42	1.62
	Night	1.16	1.55	1.70	1.70	1.53
	All	1.24	1.45	1.43	1.36	1.37
MAE	Day	1.72	1.53	1.29	1.27	1.45
	Night	0.77	1.37	1.56	1.48	1.30
	All	0.96	0.96	0.95	0.96	0.96
IOA	Day	0.89	0.90	0.93	0.94	0.91
	Night	0.94	0.90	0.88	0.89	0.90

parameterized with enough accuracy, which will be more noticeable in smaller scale simulations.

Table 7.3 gives the 2 m temperature model performance statistics for the 1 km simulations while Table 7.4 gives the same for the 6 km. Contrary to the wind speed, the

2 m temperature cool bias noted in the 6 km simulation is significantly less in the 1 km simulation. At Lake Wheeler the change is from -0.41°C to -0.12°C , at Reedy Creek from -1.02°C to -0.60°C , at Turfgrass from -0.99°C to -0.98 and at Jenkins Road from -0.84°C to -0.60°C . The 1 km simulated nighttime temperatures are the main reason for the less bias temperature prediction, the average for all stations improved from -0.67°C to -0.12°C , while the daytime temperature bias average for all stations is similar for both simulations (-0.99°C to -1.08°C). The mean average error actually increases for all stations in the 1 km simulation. The average MAE for all the stations slightly increased from 1.37°C in the 6 km simulation to 1.47°C in the 1 km. The index of agreement remains similar between the two simulations. Altogether, the temperature predictions by the 1 km simulation are not significantly different.

7.4 COUPLED ARPS-CALPUFF DISPERSION SIMULATION

The high-resolution meteorology from the simulation over Raleigh is being used to drive the CALPUFF dispersion simulation. The primary meteorological variables needed by CALPUFF are the three dimensional wind field, potential temperature, boundary layer height, friction velocity, Monin-Obukhov Length and convective velocity scale. With these variables, CALPUFF simulates the transport and diffusion of material from a specified source.

7.4.1 EXPERIMENT BACKGROUND AND DESIGN

In the Raleigh area, recent urbanization and an increasing population has elevated concerns of pollution, particularly automobile emissions. Larger cities like Los Angeles,

New York City, and Chicago have major problems with this type aspect of air pollution. Because of this, a need exists to study the local meteorology and the influence it has on the dispersion of pollutants in this small region.

Among the major contaminants from automobile emissions is particulate matter with aerodynamically equivalent spherical particle diameter of 2.5 μm or less, distinctly known as $\text{PM}_{2.5}$. Recent work at the Environmental Protection Agency in Research Triangle Park (Singh, Huber and Braddock, 2001, draft) has concentrated on developing a city scale automobile emission model, which can provide detailed emission rates along the roadways in Wake County and other cities. The Microscale Emission Factor Model for Particulate Matter (MicroFacPM) for predicting real-time motor vehicle emissions was used to estimate the diurnal $\text{PM}_{2.5}$ emission rate. This model takes into account many details including the vehicle fleet composition for the region, which accounts for different vehicle types and even the aging of automobiles of this fleet. Other factors accounted for are: length and time of travel, vehicle speed, time and day of the year, ambient temperature and relative humidity. The travel time accounts for cold starts, or the engine warm up period; a warmer engine releases less PM. Ambient temperature is used to address an important factor: air conditioners straining of the engine therefore releasing more $\text{PM}_{2.5}$.

For the CALPUFF simulation, two major roadways are integrated as line sources, with a constant emission rate per unit distance along the road length. The first thoroughfare, Interstate 40 is the major commute route from Raleigh to Research Triangle Park (RTP). The second roadway, Capital Boulevard is a highly commercialized road that runs from downtown Raleigh to the north where it splits before leaving the city.

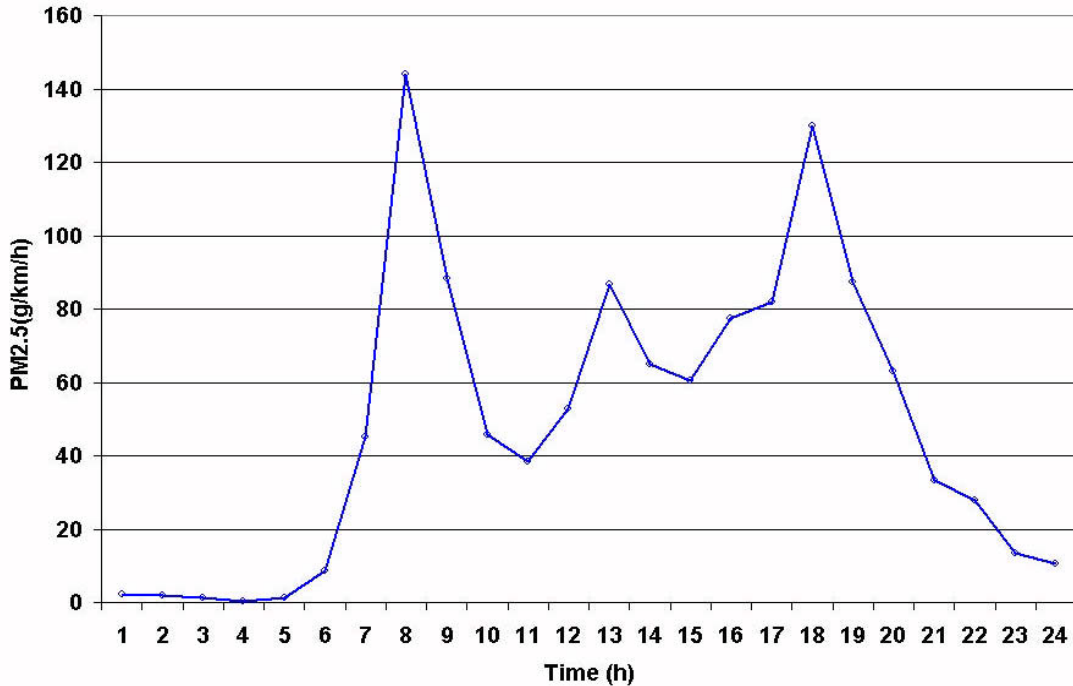


Figure 7.13 MicroFacPM simulated, diurnal PM2.5 concentration (g/km/hr) along Capital Blvd.

In order to model these non-linear roadways as line sources, the roads were split into line segments; approximately 18 separate line sources were specified to define I-40. Capital Boulevard was split into 13 line sources. Figure 7.1 shows the location of the roadways with respect to the model domain.

In CALPUFF, options are available to vary the emission rate throughout the diurnal period. Maximum source strength is prescribed and a percentage of the maximum is set for each hour of the day. Figure 7.13 shows the diurnal emission rate, calculated from the MicroFacPM model for Capital Boulevard. Even though Interstate 40 has more traffic congestion, this same diurnal emission rate was assigned. The diurnal variation shows very low emission rates between 2300 LT and 0500 LT. Large peaks are observed during the morning commute and afternoon drive home, with moderately high emissions associated with daytime activity in between.

The release height of PM_{2.5} was specified as 1 m and the roadway width was defined as 100 m. To obtain a surface concentration distribution, gridded receptors were spaced every 250 m within the 50 x 50 km domain. In the following section, the surface concentrations of PM_{2.5} for the 48 hr simulation are presented for several key time periods.

7.4.2 SIMULATED PM_{2.5} CONCENTRATIONS FROM CALPUFF

The first simulation takes place at 1000 LT on July 10th. Figure 7.14 presents the simulated surface concentration of PM_{2.5} ($\mu\text{g}\cdot\text{m}^{-3}$). To aid in the analysis, simulated 10 m wind vectors are overlaid on the concentration field as well as the major roadways around Raleigh. It needs to be noted that “hot spots” in the concentration field, near the simulated roads are a result of discrete receptors being very close if not right on the road source. Adding more receptors or increasing the resolution in the concentration pattern can dampen these “hot spots”, but this significantly increases the computational time so it was not done.

Along I-40, the mean wind direction is from the northwest. Highest simulated concentrations ($1.0\text{-}2.5 \mu\text{g}\cdot\text{m}^{-3}$) are directly over the roadway, as one would expect. A detailed look at the statistics reveals a maximum concentration of $2.55 \mu\text{g}\cdot\text{m}^{-3}$. The concentration apparently decreases rapidly away from I-40. Downwind from the interstate, the concentration decreases to $0.1 \mu\text{g}\cdot\text{m}^{-3}$ within several kilometers. A small fraction ($.001 \mu\text{g}\cdot\text{m}^{-3}$) of the pollutants are simulated well away from the road source, approximately 10 km.

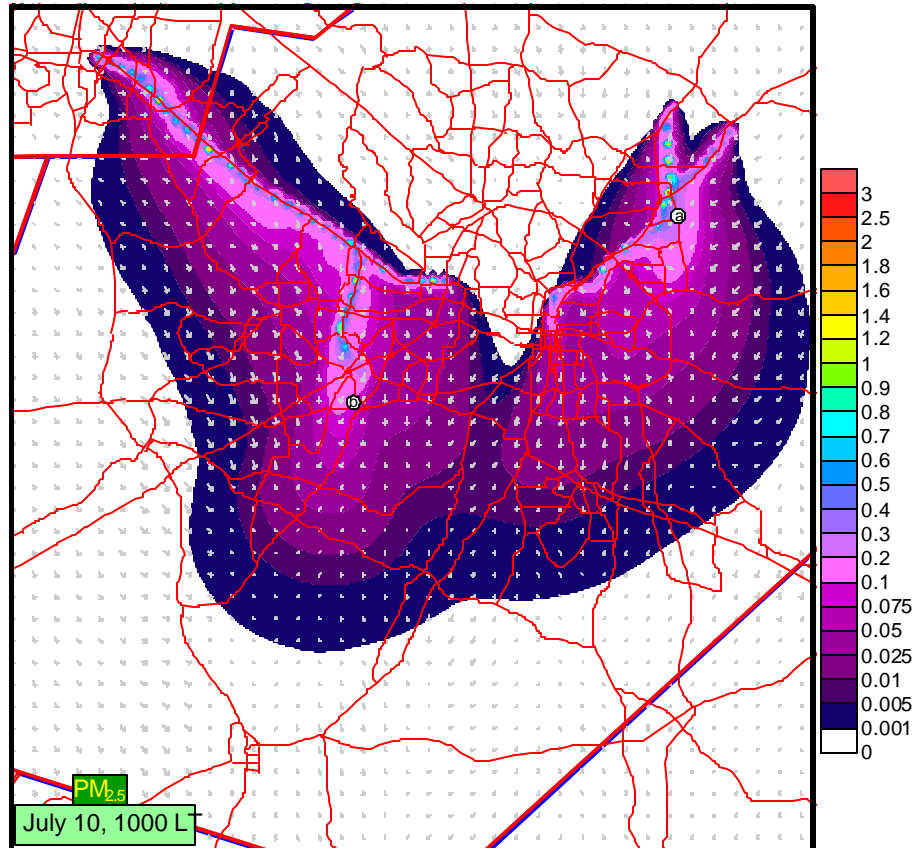


Figure 7.14 Simulated 1 hr average $PM_{2.5}$ concentration (ug/m^3) and 10 m wind vectors at July 10th at 1000 LT.

The wind direction with respect to the road has a noticeable influence on the simulated local concentrations. When wind is parallel to the roadway, the concentration increases as the $PM_{2.5}$ builds up in air parcels transported along the road. For example, in Figure 7.14 along the northern portion of Capital Blvd. (marked with circled a) the wind is nearly parallel to both the left and right fork of the road. The concentration is elevated where these two roads meet. Essentially, it appears that convergence in the wind field is resulting in convergence of the polluting material. In addition, the wind speed is light so the material is not quickly transported away from the source region. Location (b) in Figure 7.14 also illustrates a similar situation. The local wind is along this I-40 road

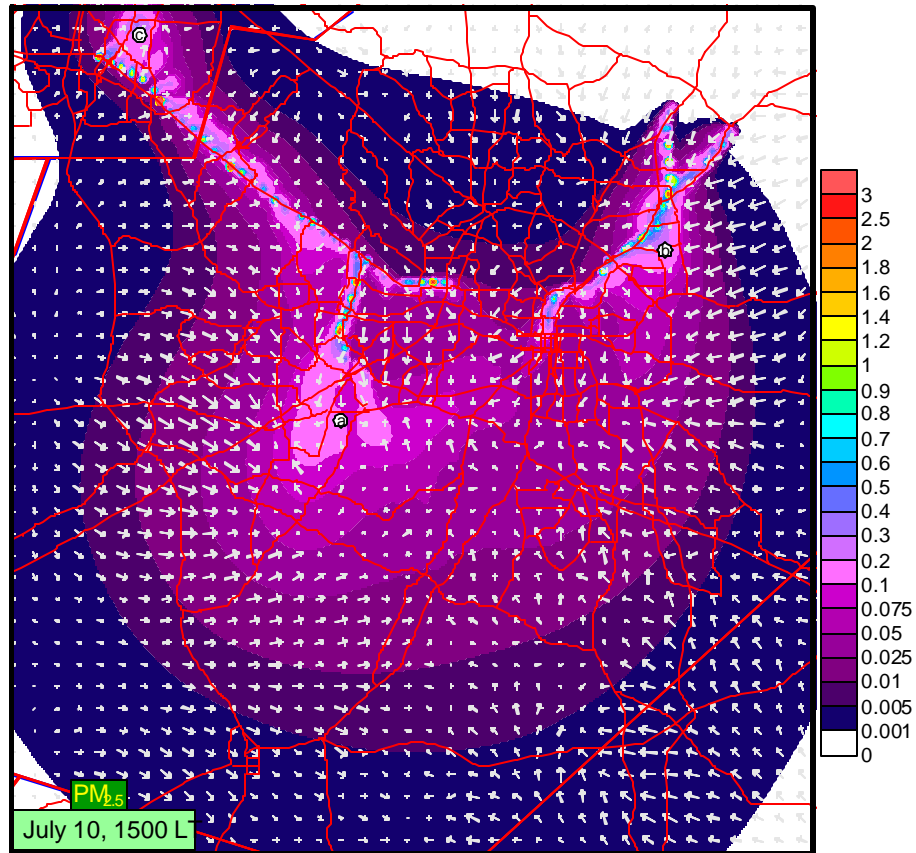


Figure 7.15 Simulated 1 hr average $PM_{2.5}$ concentration ($\mu\text{g}/\text{m}^3$) and 10 m wind vectors at July 10th at 1500 LT.

segment; therefore an elevated plume of pollutants exists downwind of the roadway. Areas where the wind is perpendicular to the road, concentrations quickly decrease as one moves away from the road source.

Shown in Figure 7.15 is the surface concentration of $PM_{2.5}$ at 1500 LT on July 10th. From the concentration data, the highest point concentration is $10.14\mu\text{g}\cdot\text{m}^{-3}$. As in the previous example, the greater concentrations are over the simulated roadways. The wind field is extremely complex as the large scale wind is light and complex variations in the surface heating leads to coherent convective patterns. Location (a) marked on the

figure shows an apparent microscale zone of wind convergence in which the surface concentrations are greater relative to other areas. Referring back to Figure 7.3a and Figure 7.3b, the meteorology near this time reveals low turbulence and cooler surface temperatures in this area. Higher concentration location (b) is in another area where the wind is also converging. In the two hours before 1500 LT this semi-static convergence zone has allowed a build up of material, transported from the two northern roadways. The highly convective boundary layer with large variations in wind speed and direction has diffused trace amounts of PM_{2.5} over much of the region. Additionally, the relatively light wind allows the local buildup of material not transported away from the city.

The next simulated time is in the early evening of July 10th at 1800 LT. At this time, previously discussed observations from the Model 2000 SODAR system suggest that the boundary layer began to collapse as the surface temperatures cooled. Traffic congestion is greatest at this time. Figure 7.16 presents the simulated surface concentration of PM_{2.5}. The maximum concentration measured from the receptor grid is greater than other previous times (16.74 $\mu\text{g}\cdot\text{m}^{-3}$). The pattern reveals more widespread areas of higher concentrations away from the road sources as well as greater concentrations along the roadways. Near location (a) the surface concentration is noticeably greater as a result of light wind and convergence. The boundary layer is quickly stabilizing in this location, so the pollutants are not efficiently dispersed away from the road source or further up in the atmosphere. Two other areas (location (b) and (c)) show a similar trend. Location (b) seems to have higher simulated concentrations because of two factors. One, the wind flow is across the two road sources so air parcels are loaded with twice the amount of material. Secondly, the more concentrated zone is

along an area of noticeable wind convergence. Location (c) appears to be a result of wind speed convergence. Material transported away from the source region builds up in an area where the wind suddenly slows. The reason for lighter wind speed over this small area is probably the cooler surface temperature and less unstable boundary layer.

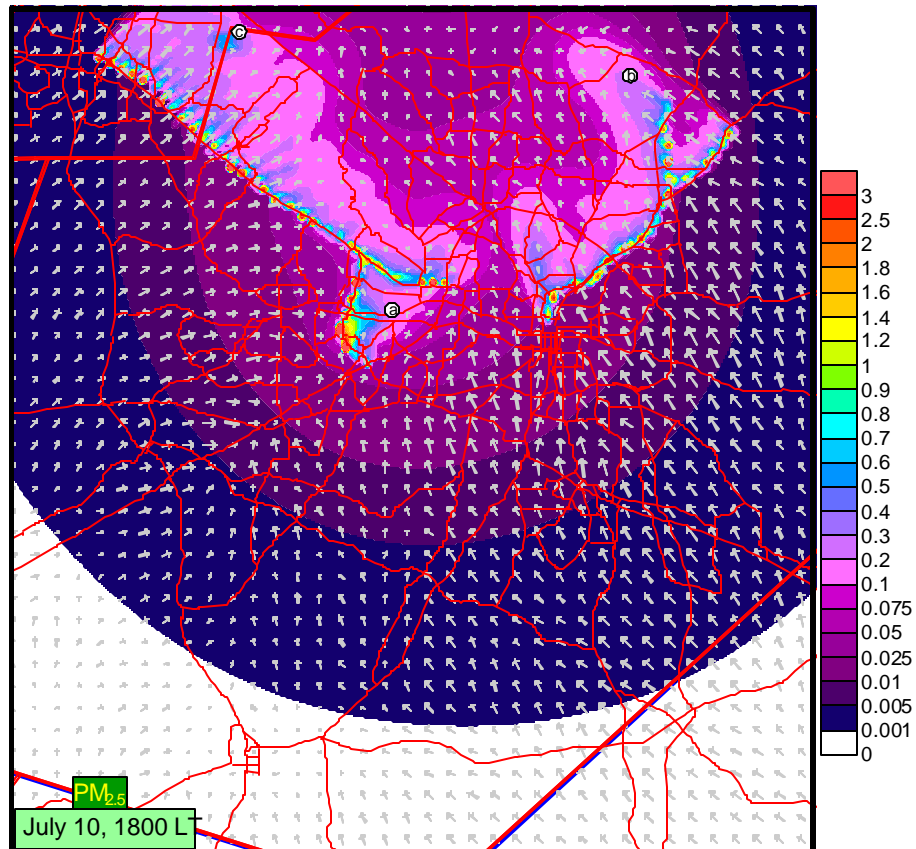


Figure 7.16 Simulated 1 hr average PM_{2.5} concentration ($\mu\text{g}/\text{m}^3$) and 10 m wind vectors at July 10th at 1800 LT.

Figure 7.17 gives the surface concentration a few hours later (2100 LT). At this time the SODAR data indicates a stable boundary layer has formed. The maximum sampled point concentration ($3.29 \mu\text{g}\cdot\text{m}^{-3}$) from the receptor grid is much lower than it was at 1800 LT. This is attributed to the lessened source strength as traffic diminishes.

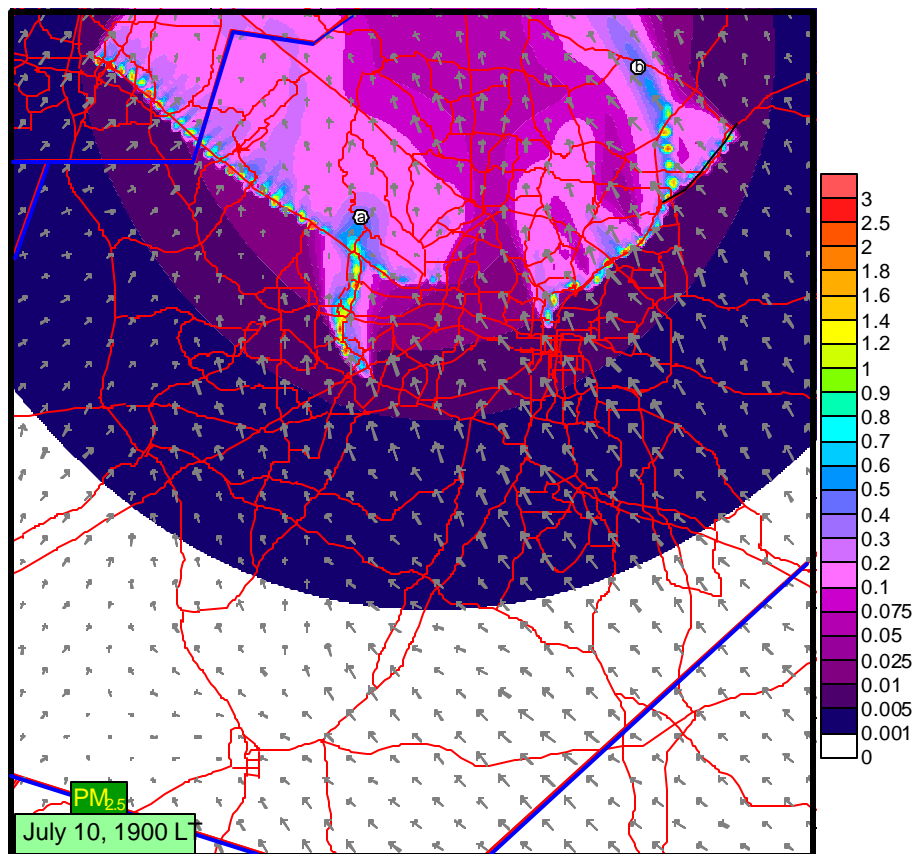


Figure 7.17 Simulated 1 hr average $PM_{2.5}$ concentration (ug/m^3) and 10 m wind vectors at July 10th at 2100 LT.

The receptors near the simulated roadways are showing less $PM_{2.5}$ when compared to the previous time. Location (a) indicates an area of elevated $PM_{2.5}$ away from I-40. Again, it appears the reason for this is the lower wind speed and obvious wind convergence. Location (b) is another elevated area of concentrations. The material transported by the wind crossing the two road segments is likely the cause of the elevated concentrations.

MicroFacPM estimated emissions shown in Figure 7.13 indicate the emission rate is very low during the early morning. The simulated surface concentrations at 0200 LT are shown in Figure 7.18. Even though the boundary layer height is low and near surface stability is high, the simulated concentrations are small. The highest reported

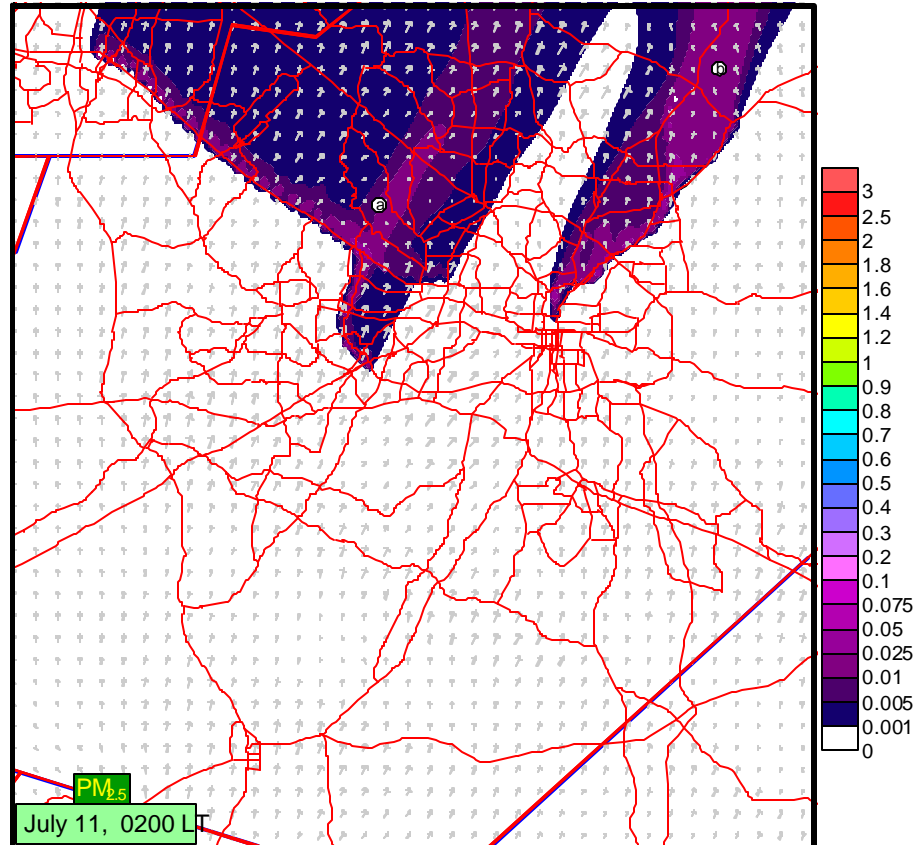


Figure 7.18 Simulated 1 hr average $PM_{2.5}$ concentration ($\mu\text{g}/\text{m}^3$) and 10 m wind vectors at July 11th at 0200 LT.

concentration from the receptor grid is significantly lower ($0.05\mu\text{g}\cdot\text{m}^{-3}$). The concentration pattern reveals two areas, location (a) and (b), where the concentration of $PM_{2.5}$ is relatively high. Referencing the domain elevation given in Figure 7.2a shows that these areas correspond to lower valleys where the boundary layer is more stable as a result of slope flow from surrounding elevated areas. Although the ambient emissions rate was prescribed low; these regions would present problems, from a high concentration standpoint, if some toxins were accidentally released in high quantities.

The next simulation is for the following morning (July 11th at 0800 LT). This time corresponds to high traffic volume and greater emission rates. Figure 7.19 shows the

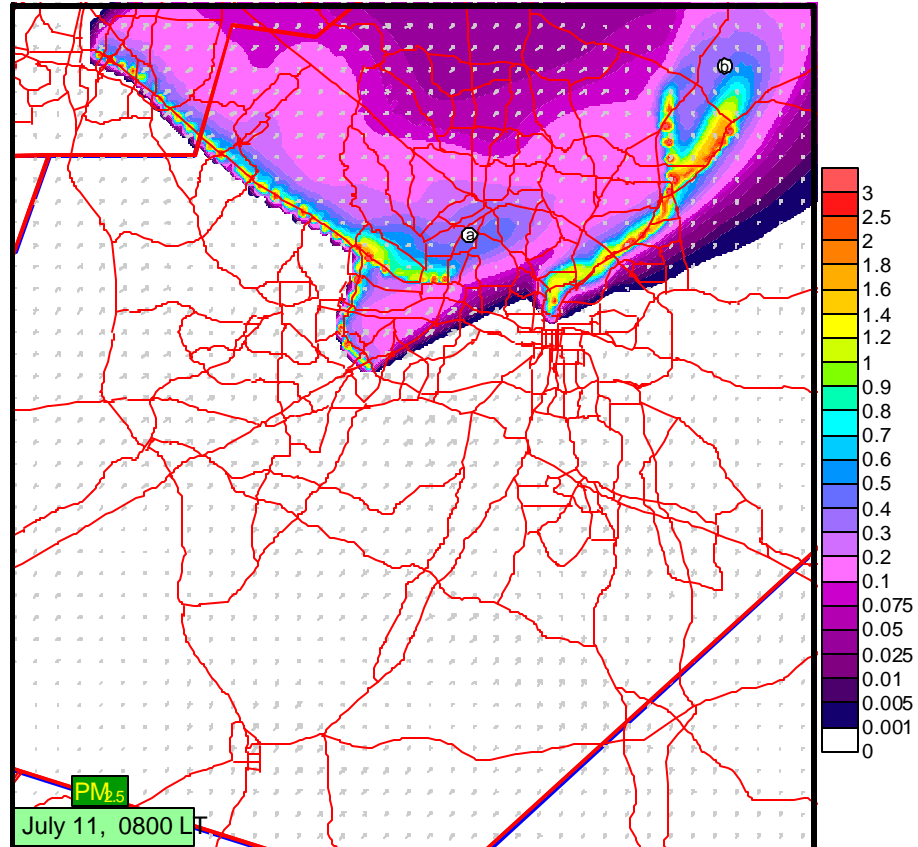


Figure 7.19 Simulated 1 hr average $PM_{2.5}$ concentration ($\mu\text{g}/\text{m}^3$) and 10 m wind vectors at July 11th at 0800 LT.

simulated concentration from the two major roadways at this time. The maximum concentration from the 250 m spaced grid of receptors is $6.25 \mu\text{g}\cdot\text{m}^{-3}$. Widespread higher concentrations, relative to all the other times, exist around the roadways. The light wind simulated by ARPS and still low boundary layer height is the cause of these elevated concentrations. The same two low lying areas discussed in the previous figure, appear to significantly influence the concentration away from the roadways. The boundary layer is more stable and wind is lighter in these areas. Contributing to this is the flow direction relative to the roadway. The flow appears to be modified by the terrain, which in turn modifies the concentration field.

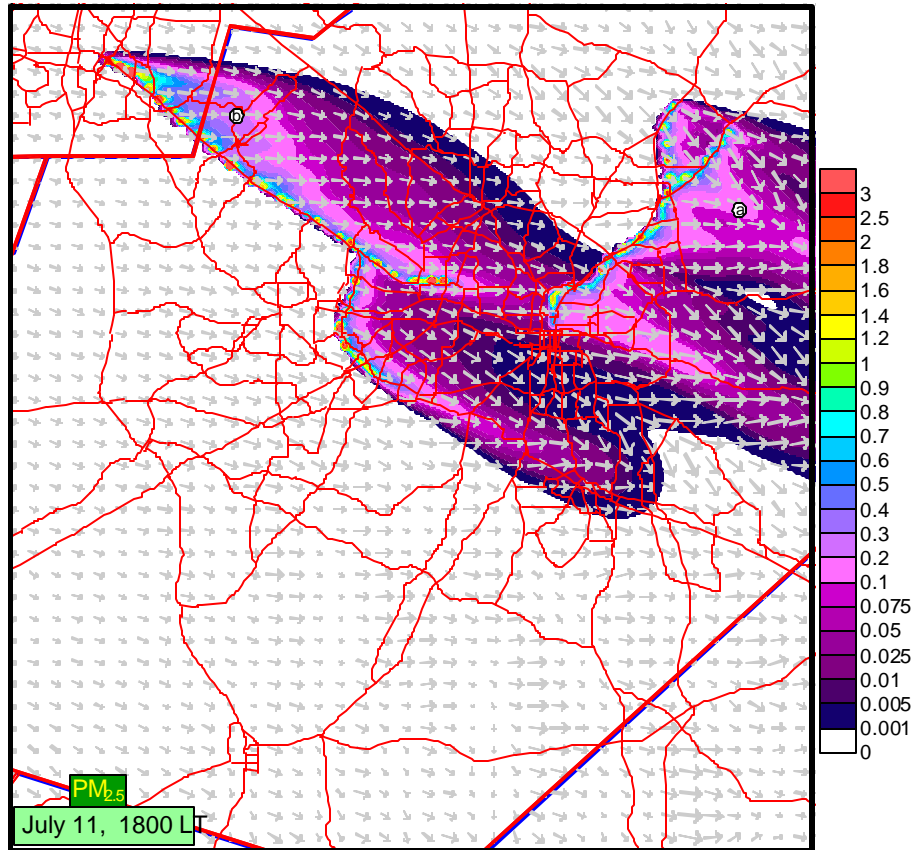


Figure 7.20 Simulated 1 hr average $PM_{2.5}$ concentration ($\mu\text{g}/\text{m}^3$) and 10 m wind vectors at July 11th at 1800 LT.

Figure 7.20 gives the surface concentration pattern at 1800 LT on July 11th. Again, this is a busy commute period so the emission rate is elevated along the two simulated roadways. The maximum concentration ($21.02 \mu\text{g}\cdot\text{m}^{-3}$) in the domain is greater than that for any other time. At the same time on the previous day the highest concentration was approximately $16 \mu\text{g}\cdot\text{m}^{-3}$ while during the early mornings the maximum concentration is much lower (around $5 \mu\text{g}\cdot\text{m}^{-2}$), even though the source strength is similar. It is believed that the loading of $PM_{2.5}$, from higher emissions throughout the day, is a main contributor to the higher concentrations in the evenings than in the mornings. This implies that air quality in the region may be worst in the

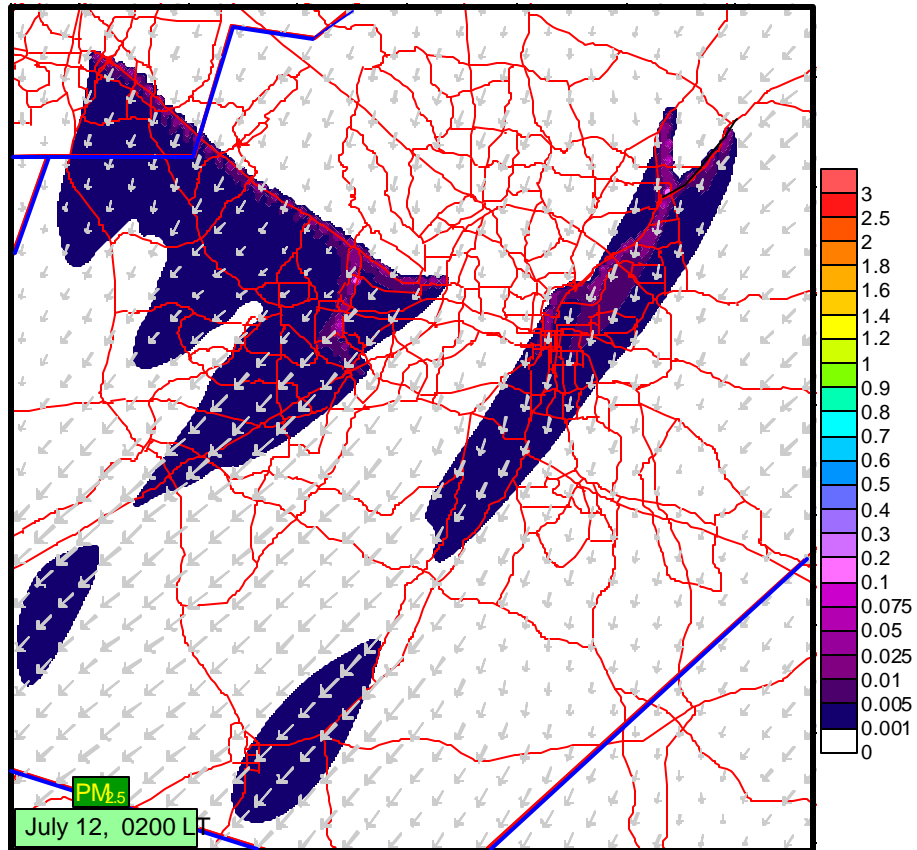


Figure 7.21 Simulated 1 hr average $PM_{2.5}$ concentration (ug/m^3) and 10 m wind vectors at July 12th at 0200 LT.

evenings. The concentration pattern relates higher levels of $PM_{2.5}$ to convergence areas. Location (a) shows this, as do several other areas. Location (b) is another concentrated area; the most likely cause is the along road wind direction.

The next simulation of the concentration field occurs on July 12th at 0200 LT. The highest reported concentration in the model domain is $0.58 \mu g \cdot m^{-2}$. Similar to the previous night the surface based concentration (Figure 7.21) is much less than that during the day. The wind speed is stronger than the previous night as a cool front has backed into the region. After daybreak on the following morning Figure 7.22 shows the surface concentrations increase as a result of the increase in traffic (0800 LT). The maximum

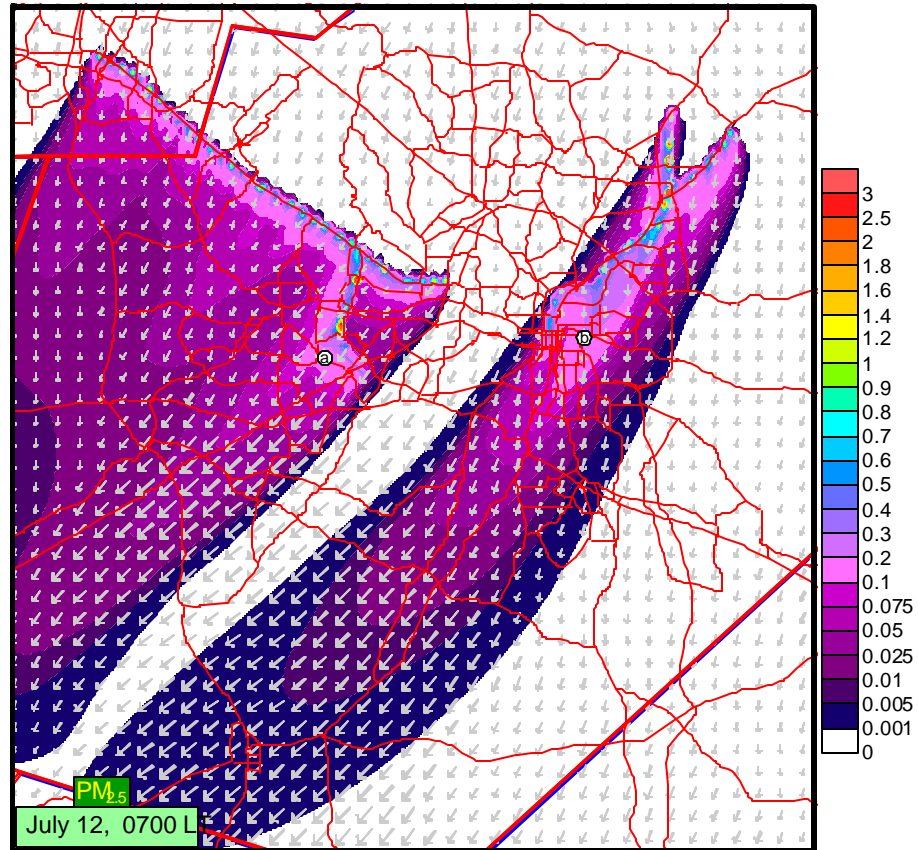


Figure 7.22 Simulated 1 hr average PM_{2.5} concentration (ug/m³) and 10 m wind vectors at July 12th at 0800 LT.

concentration ($5.96 \mu\text{g}\cdot\text{m}^{-2}$) in the model domain is similar to the previous morning. Unlike the prior morning, the wind speed is stronger and the emissions are transported more quickly away from the roadways. A similar pattern, seen at other times, is the plume of higher concentrations downwind of road source where the wind direction is parallel to the roadway. In locations where the wind is perpendicular to the road, the concentrations quickly diminish as one moves away from the source region.

7.4.3 SUMMARY

The dispersion analysis of PM_{2.5} from roadway emission over the Raleigh area included an examination of concentration patterns as influenced by local meteorology.

The main contributor to the surface concentrations in this case is the traffic count or source strength. It was shown that the early evening hours are associated with the highest concentrations along and downwind from the roadways. Mid-morning is another time when the air is more concentrated but to a much lesser degree than the evening. A reason for this is the diurnal variation in traffic volume. Overnight, the traffic is much less than that during the day. The loading of the atmosphere with local emissions is much greater during the day. So as the boundary layer collapses in the evening, more particulate matter is present near the surface. At night, material from the previous day has time to be either advected out of the region or deposited on the surface, without a chance for more particulates to be introduced. In the early morning, when traffic increases, there is little residual material from the previous night. The increased concentrations at this time are mostly due to the peak in emissions over a few hours.

Examination of the relation of concentration pattern to the local meteorology showed that several weather related factors influence the $PM_{2.5}$ variation. The wind direction relative to the roadway is one of the important factors. When air travels along the direction of the roadway, parcels are continually loaded with pollutants. A straight road such as I-40 running northwest to southeast between Raleigh and RTP will have higher concentrations when the wind is from the northwest or southeast.

Higher resolution modeling with the 1 km ARPS simulation revealed several microscale convergence zones resulting from horizontal sensible heat flux gradients. In the dispersion simulation, these convergence zones are directly related to higher surface concentrations. The convergence is not only wind convergence but also pollution convergence. Areas of light wind are also associated with higher concentrations. The

lighter wind in this case is a result of convective micro-downdrafts and lowered boundary layer depth during the day and more stable conditions at night. The landuse influence on the meteorology can be attributed to these meteorological variations.

The terrain heights are also shown to influence the wind field and therefore, the concentrations field. Higher areas, specifically the higher south to north ridge in the western part of the domain is associated with slightly stronger wind at night and therefore lower concentrations. The low lying areas just to the east of this ridge are shown to be more stable as a cooler slope flow is established at night. This drainage flow allows pollutants to collect over highly populated suburbs around Raleigh. Although the emission rate and concentrations are much lower at night, these areas have a tendency to collect pollutants when compared to other higher areas.

CHAPTER 8

SUMMARY AND CONCLUSIONS

Although humans reside in atmospheric boundary layer and have a continuous, intimate contact with the processes that dominate this layer; its chaotic, random nature is difficult to quantify. A main reason for this difficulty is the irregular surface that dominates the earth. Boundary layer behavior, persuasions and tendencies in one region cannot be automatically equated to the same of another region since surface characteristics are not identical. In North Carolina, the highly variable geographical characteristics, prime the region for multi-scale diverse weather phenomena. The mountains, piedmont and coastal plains have unique combinations of soil, vegetation, roughness and terrain features. Additionally, the Atlantic Ocean's influence dominates the weather and climate of areas near the land-sea interface. The stark difference in thermal properties between land and sea induce mesoscale land and seabreeze circulations on a continuous basis. Similar thermally direct circulation tends to form along vegetation, surface thermal, and soil moisture gradients. Elevated terrain can also significantly alter the flow within the boundary layer.

The boundary layer investigations described in this thesis employed a variety of tools to assist in better understanding of the complex variations that occur in the lower troposphere as a result of regional and local scale surface heterogeneities. A distinctive combination of atmospheric simulations, local scale dispersion simulations and

observations from both a surface meso-network and SODAR cluster to evaluate the simulations were presented and discussed.

A boundary layer observational analysis of detailed SODAR and three level 10 m micrometeorological tower measurements was presented in Chapter 2. The main emphasis of this chapter was to compare and contrast boundary layer observations from the instrument cluster during two typical meteorological conditions. The presented observational analysis showed a significant difference between the two cases.

The near-neutral case showed that the boundary layer properties remained relatively constant during the 24-hour period. The SODAR reflectivity indicated that the height of the surface layer, as indicated by strong echoes, remained around 100 m during this 24 hr period. The static stability, implied by the 10 m - 2 m temperature difference, was near-neutral. The SODAR derived horizontal velocity profile up to 200 m also showed a relatively regular pattern where the wind speed increased with height in a logarithmic manner. The wind speed profile indicated time dependent fluctuations in magnitude, associated with shear induced boundary layer eddies. On the same line, the tower wind speed measurements had comparable variations in velocity. Vertical velocity estimates from the Model 4000 miniSODAR showed similar fluctuations in vertical motion. A correlation existed between the vertical and horizontal motion derived from this instrument. During brief periods of strong ascent, the horizontal wind speed profile showed relatively light wind, while periods of strong decent were connected to stronger horizontal velocities. This relationship directly corresponds to a down gradient transfer of momentum in the boundary layer.

Conversely, the convective case showed a rapidly increasing boundary layer during the early morning, just after sunrise. Strong fluctuating periods of high reflectivity during the day allude to convective boundary layer thermals. At the same time, 10-2 m temperature gradient showed strong buoyant instability. The overall convective patterns and associated boundary layer momentum are much different than those of the neutral case. Horizontal velocity profiles from the Model 4000 miniSODAR indicated constant light winds up to 200 m while the vertical motion showed fluctuations from thermal convection. A well-defined nocturnal boundary layer was seen in this case and not in the neutral case. The nocturnal boundary layer height is well determined by the SODAR as approximately 150 m. Wind speed profile at night showed an increase in momentum at the top of the boundary layer where a nocturnal jet existed. Overall, the combination of tower based and remote sensing instruments provided good information on the boundary layer structure and detailed information on the wind field.

A tropical seabreeze simulation was presented in Chapter 5. The numerical atmospheric simulation showed that the boundary layer properties are distinctly different across a region that is affected by seabreeze circulations. The marine boundary layer well offshore changes very little over the diurnal period while closer to shore the boundary layer structure is influenced by the seabreeze. The MBL height decreases within the offshore zone of the seabreeze circulation, due to both subsidence and warmed land air advected in the return flow. Although the dispersion pattern well offshore did not change, closer to shore the concentrations are higher over a greater area due to the lower MBL. The plume was also advected towards shore because of the onshore component of the seabreeze.

Close to shore, the model simulated a seabreeze, which developed around mid-day at the land-sea interface. In the afternoon the seabreeze strengthened and slowly moved inland in the afternoon and then accelerated to a position 50 km inland just before sunset. The dispersion experiment from a point source near the coastline indicated that the seabreeze has a very noticeable effect on atmospheric dispersion overland. Higher surface concentrations were modeled during both the seabreeze episode and during the post seabreeze period later in the evening. Pollutants were transported inland as a result of the seabreeze, and remained concentrated as the stable boundary layer formed.

Overland, the simulations depicted the evolution of the boundary layer as expected. At the well inland location (100 km), the boundary layer was shown to quickly grow during the morning, from stable to convective. In the evening the convective boundary layer quickly stabilizes, then the stable boundary layer slowly deepens through the night. Certain properties like TKE, potential temperature, momentum and boundary layer height were consistent with each other and with observational studies. Hence, the dispersion pattern of a well inland point source exhibited an expected distribution; well dispersed during the daytime with low concentrations, and higher concentrations at night.

The regional numerical simulation over eastern North Carolina, presented in Chapter 6, combines several interesting boundary layer scenarios, central to air quality considerations. On the first day the boundary layer was characterized as convective, during the day, where buoyancy driven turbulence was a main factor in TKE generation. In these situations the wind speed is typically light, cloud cover nonexistent and ozone production maximized. Supporting this, the North Carolina Department of Natural Resource/Division of Air Quality reported a peak in observed ozone on this day.

Surface temperature patterns from the model during the day were consistent with AVHRR satellite images in terms of the warmer and cooler areas over the region. The typically warmer Sandhills region and some of the larger urban centers were simulated as warmer surfaces. Turbulence was also higher over these warmer locations. Landuse has a definite impact on the degree of simulated turbulence as well as the boundary layer height. The boundary layer height over the open, more convective areas is greater than the less convective forest areas.

During the first day of this event, the model consistently underestimated the daytime temperature by several degrees while simulating the nighttime temperature better. The wind speed variation was well simulated during the day for most stations, but the wind direction was off by as much as 180° . Additionally, the model had a bias in predicting strong surface wind speeds with the average absolute error being less than $1 \text{ m}\cdot\text{s}^{-1}$. Once the boundary layer became stable at night the wind direction better compared to the model results, although the wind speed was still consistently stronger than realized. It is thought that during light wind conditions when the boundary layer is highly convective, the variation in wind direction is greater and more difficult to model.

On the second day of the simulation, 0800 LT July 11th – 0800 LT July 12th, the synoptic flow was more pronounced. Wind speed in the boundary layer was much stronger than the first day. This was the main difference between the two days as the cloud cover remains low and surface heating similar. This led to an unstable boundary layer in which both buoyant convection and wind shear contribute to the generation of turbulence. Again, this type of situation is typically realized in North Carolina during the summer ahead of cold fronts. The model simulated TKE showed stronger turbulent

energy on the second day as well as a deeper boundary layer. The boundary layer height directly correlated to the surface heating and associated turbulence distribution.

A comparison of simulated 2 m temperatures with the observations was better than the first day, during both the day and night, even though the model still contained an overall cool bias. The wind speed and variation was also better simulated on the second day, as was the wind direction. The model did well on both the strength and timing of a meso cool front that passed through the region towards the end of the simulation.

A high-resolution atmospheric simulation was conducted over Raleigh, North Carolina for the same case presented by the regional simulation (Chapter 7). The high-resolution meteorological data was used for a dispersion simulation over the same area. The 1 km model forecast showed large distinctions within the microscale boundary layer structure over the city scale domain. The boundary layer variations were directly related to the landuse parameterization. Surface heating between open areas and vegetated areas was noted as the main driver behind differences in the boundary layer structure during the day. Resulting heat flux gradients induced discrete convective patterns on the first day when the large-scale influence was weak. The turbulence and boundary layer height was elevated within the core of these convective structures. In the surrounding areas, downward motion reduced the amount of turbulence and significantly suppressed the boundary layer height.

On both nights, the high-resolution simulation was sensitive to terrain variations. Over the more elevated areas the wind speed was overall higher, while noticeably weaker over low-lying areas. A down slope flow was detected and associated temperatures were less in the low-lying areas. The simulated vertical west to east cross-

section revealed an extremely strong inversion from the surface to 100 m with a nocturnal jet feature at this level on both nights. The data from both the Model 4000 and Model 2000 SODARs compared well with the simulated profiles at night. A strong inversion was simulated which compared to an observed layer of high SODAR reflectivity. The observed vertical wind distribution was also well simulated by ARPS. Even an observed cool front was well depicted in the model simulation.

On the second day, the simulation increases the boundary layer momentum. The boundary layer structure was noticeably different as compared to the first day. Rather than cellular type thermal convection, elongated horizontal rolls features were simulated. Wind direction was less modified but definite convergence zones were noticed and were consistent with horizontal roll type convection. The higher boundary layer momentum was shown to increase the TKE within the boundary layer.

SODAR reflectivity profiles on both days showed a highly convective boundary layer and were consistent with the simulated super-adiabatic, surface layer potential temperature profile. Observed wind speed profiles were strikingly similar between the simulation and SODAR observations. Changes in wind direction seen in the observed profile were well simulated.

The dispersion analysis of $PM_{2.5}$ from roadway emission over the Raleigh area included an examination of concentration patterns. The main contributor to the surface concentration in this case is the traffic density or source strength. As a result, it was shown that the early evening rush hours are associated with the highest concentrations along and downwind from the roadways. Mid-morning was another time when the air pollution was more concentrated, but to a lesser degree than in the evening. A possible

reason for this is the loading of the atmosphere with local emissions is much greater throughout the day. So as the boundary layer collapse in the evening, more particulate matter is present near the surface. At night, material from the previous day has time to be either advected out of the region or deposited on the surface, without more particulates being introduced. In the early morning, when traffic increases, there is little residual material from the previous night. The increase in concentrations at this time is mostly due to the peak in emissions over a few hours.

The relationship of concentration patterns to the local meteorology showed that several weather related factors influenced the $PM_{2.5}$ variation. The wind direction relative to the roadway is one of the most apparent factors. When air travels along the direction of major roadways, parcels are continually loaded with pollutants. A straight road such as I-40 running northwest to southeast between Raleigh and RTP, will have higher concentrations when the wind is from the northwest or southeast. This may imply that roadways that are aligned perpendicular to the climatological flow direction are likely to result in higher concentrations than otherwise, especially areas downwind of the roadways.

The 1 km ARPS simulation almost explicitly represented microscale convergence zones resulting in convective thermals. In the dispersion simulation these convergence zones are directly related to higher surface concentrations. The convergence is not only wind convergence but also pollution convergence. Areas of light wind are also associated with higher concentrations. The lighter wind in this case is a result of convective micro-downdrafts and lowered boundary layer depth during the day and more nocturnally stable

conditions at night. The meteorological variations can be directly attributed to landuse influences.

The terrain heights were also shown to influence the wind field at night and therefore, modified the concentrations field. More elevated areas, specifically the higher north-south ridge in the western part of the domain is associated with slightly stronger wind at night and therefore lower concentrations. The lower lying areas, just to the east of this ridge are shown to be more stable as a cooler slope flow is established at night. This drainage flow allows pollutants to collect over highly populated suburbs around Raleigh. Although the emission rate and concentrations were much lower at night, these areas have a tendency to collect pollutants when compared to elevated areas.

Observations are a key component of any study. SODAR observations were used in this research to give some confidence of the ARPS forecasts, as were surface based observations (NC ECO Net stations). Statistics of these comparisons showed the inevitable imperfections of ARPS. Apparently, the surface parameterization for both the regional and city scale domains are not refined enough to provide non-biased predictions. The 2 m temperatures were under predicted in all cases and the 10 m wind speed was over predicted. On the better side, the average absolute wind speed error was shown to be less than $1 \text{ m}\cdot\text{s}^{-1}$ over the entire period, for all the stations. Although statistics were not compiled for the comparison between simulated and observed wind profiles, the model predicted profiles appear to compare better in both speed and direction than the surface wind. This supports the suggestion that the near surface errors are due to imperfect surface parameterizations. Efforts are underway to examine this in the future with more detail. It will likely help if the surface classifications are less discrete. This can be

addressed, for example, by adding more vegetation, surface roughness and even urban categories. Detailed landuse data is being acquired for the Raleigh area through aerial photography, so that highly commercialized, residential, forest, fields and other dominate surface features can be more explicitly represented. With further study, the surface characterization of the domain can be adjusted so that more exact local scale predictions can be accomplished.

The dispersion simulations need much more attention in terms of validation. One of the most difficult predictions, from an atmospheric modeling perspective, is that of pollution concentrations. In this study, the seabreeze dispersion simulations showed believable dispersion patterns as a result of the seabreeze but the actual concentrations are not easily validated. The roadway dispersion simulation also showed plausible patterns and indicated areas, related to surface properties, where higher concentrations may exist. Again, these results need to be further studied and validated with observations from air pollution samplers in the region.

LIST OF REFERENCES

- Allwine, Dabberdt, and Simmons, 1998: Peer Review of the Calmet/Calpuff Modeling System. U.S. Environmental Protection Agency, Research Triangle Park, NC.
- Arritt, R. W., 1993: Effects of large scale flow on characteristic features of the seabreeze. *J. Appl. Meteor.*, **32**, 116-125.
- Arya, S.P.,1984: Parametric relations for the atmospheric boundary layer. *Boundary Layer Meteorology.*, **30**, 57-73.
- Arya, S.P.,1999: *Air pollution meteorology and dispersion*, Oxford Univ. Press.
- Arya, S. P., 2001: *Introduction to Micrometeorology, Second Edition*, Academic Press, New York.
- Atkins, N. T. and Wakimoto: 1997: Influences of the synoptic-scale flow on sea breezes observed during CAPE. *Mon. Wea. Rev.*, **125**, 2112-2130.
- Bechtold, P., J.P. Pinty, and P. Mascart, 1991: A numerical investigation of the influence of large-scale winds on sea-breeze and inland-breeze type circulations. *J. Appl. Meteor.*, **30**, 1268-1279.
- Bougeault, P., B. Bret, P. Lacarrère, and J. Noilhan, 1991: An experiment with an advanced surface parameterization in a mesobeta-scale model. Part II: the 16 June 1986 simulation. *Mon. Wea. Rev.*, **119**, 2374-2392.
- Businger, J.A., J.C. Wyngaard, Y. Izumi and E.F. Bradley, 1971: Flux-profile relationships in the atmospheric surface layer. *J. Atmos. Sci.*, **28**, 181-189.

- Byun, D. W., 1990: On the analytical solutions of flux-profile relationships for the atmospheric surface layer. *J. Appl. Meteorol.*, **29**, 651-657.
- Chou, M.D., 1990: Parameterization for the absorption of solar radiation by O₂ and CO₂ with application to climate studies. *J. Climate.*, **3**, 209-217.
- Chou, M.D., 1992: A solar radiation model for climate studies. *J. Atmos. Sci.*, **49**, 762-772.
- Chou, M.D., and M.J. Suarez, 1994: An efficient thermal infrared radiation parameterization for use in general circulation models. NASA Tech Memo 104606, 85 pp.
- Crescenti, G. H., 1998: The degradation of Doppler sodar performance due to noise: A review. *Atmos. Environ.*, **32**, 1499-1509.
- Crescenti, G. H., 1999: A study to characterize performance of various ground-based remote sensors. NOAA Technical Memorandum ERL ARL-229, 286p.
- Deardorff, J.W., 1972b: Parameterization of the planetary boundary layer for use in general circulation models. *Mon. Wea. Rev.*, **100**, 93-106.
- Draxler, R.R., 1976: Determination of atmospheric diffusion parameters. *Atmospheric Environment.*, **10**, 99-105.
- Gera, B.S. and N. Saxena, 1996: SODAR data-A useful input for dispersion modeling. *Atmos. Environ.*, **30**, 3623-3631.
- Gilliam, R.C., S. Raman and D. Niyogi, 2001: Observational and numerical study on the influence of large-scale flow direction and coastline shape on the seabreeze evolution. *Bound.-Layer Meteor.*, Draft.

- Hanna, S.R., G.A. Briggs, J. Deardorff, B.A. Egan, F.A. Gifford and F. Pasquill, 1977: AMS workshop on stability classification schemes and sigma curves – summary of recommendations. *Bull. Am. Meteor. Soc.*, **58**, 1305-1309.
- Hicks, B.B., 1985: Behavior of turbulence statistics in the convective boundary layer. *J. Clim. And Appl. Meteor.*, **24**, 607-614.
- Hogrefe, C., S.T. Rao, P. Kasibhatla, G. Kallos, C.J. Tremback, W. Hao, D. Olerud, A. Xiu, J. McHenry and K. Alapaty, 2001: Evaluating the performance of regional-scale photochemical modeling systems: Part I-meteorological predictions. *Atmos. Environ.*, **35**, 4159-4174.
- Kain, J.S. and J.M. Fritsch, 1993: Convective parameterization for mesoscale models: The Kain-Fritsch scheme. The representation of cumulus convection in numerical models. Meteor Monogr, Amer Meteor Soc. 165-170.
- Kitada, T. and H. Ueda, 1989: *Pollutant dispersion and land/sea breeze circulations*. In Encyclopedia of Environ. Control Technol., pp. 583-630. Gulf Publishing Comp.
- Kidwell, K.B., 1990: Global Vegetation Index User's Guide. USDOC/NOAA National Climate Data Center, Satellite Data Services Division, Washington DC.
- Kineman, J.J. and M.A. Ohrenschall, 1992: Global Ecosystem Database (CD-ROM) Version 1.0 Documentation Manual. EPA/600/R-96/194b, NGDC Key to Geophysical Records Documentation No. 27, National Geophysical Data Center, NOAA, Boulder, CO.
- Li, B. and R. Avissar, 1994: The impact of spatial variability of land-surface characteristics on land-surface heat fluxes. *J. Climate.*, **7**, 527-537.

- Lyons, W. A., 1975: Turbulent diffusion and pollutant transport in shoreline environments. *Lectures on Air Pollution and Environmental Impact Analysis*, pp. 135-208. *Amer. Meteor. Soc.* Boston, MA.
- Lyons, T.J., P. Schwerdtfeger, J.M. Hacker, I.J. Foster, R.C.G. Smith, and H. Xinmei, 1993: Land-atmosphere interaction in a semiarid region: The bunny fence experiment. *Bull. Amer. Meteor. Soc.*, **74**, 1327-1334.
- Nieuwstadt, F.T.M., 1984: Some aspect of the turbulent stable boundary layer. *Bound.-Layer Meteor.*, **30**, 31-55.
- Niyogi D., Raman S. and Perry K., 1998: NC ECO Net: Towards an integrated climate and environmental observation network for North Carolina. in preprint, *23rd Conf. on Agricultural and Forest Meteorology*, Albuquerque, New Mexico, November 2—5, 1998,.
- Noilhan, J. and S. Planton, 1989: A simple parameterization of land surface processes for meteorological models. *Mon. Wea. Rev.*, **117**, 536-549.
- NSSC, 1994: State Soil Geographic (STATSGO) Data Base. Miscellaneous Publication Number 1492, National Soil Survey Center, United States Department of Agriculture.
- Oke, T. R., 1978: *Boundary Layer Climates*, London, Methuen and Sons, 372pp.
- Oke, T.R.: 1987: The surface energy budget of urban areas. *Modeling the Urban Boundary Layer*, Amer. Meteor. Soc., Boston. 1-52.

- Panofsky H.A., H. Tennekes, D.H. Lenschow and J.C. Wyngaard, 1977: The characteristics of turbulent velocity components in the surface layer under convective conditions. *Bound.-Layer Meteor.*, **11**, 355-361.
- Raynor, G. S., S. SethuRaman and R. M. Brown, 1979: Formation and characteristics of coastal internal boundary layers during onshore flows. BNL Report 21668. *Bound.-Layer Meteor.*, **16**, 487-514.
- Rhome, J., D. Niyogi and S. Raman, 2001: Transport and deposition from agriculture emissions from eastern North Carolina, USA. *Pure and Appl. Geophys.* In press.
- Scire, J.S., D.G. Strimaitis and R.J. Yamartino, 2000: A user's guide for the CALPUFF dispersion model, Version 5. Earth Tech, Inc., Concord.
- Simpson, J.E., Mansfield, D.A., and Milford, J.R.: 1977: Inland penetration of sea-breeze fronts. *Quart. J. Roy. Meteor. Soc.*, **103**, 47-76.
- Simpson, J. E., D.D. Reible, and P.F. Linden, 1993: The Sea Breeze and Gravity Current Frontogenesis. *Quart. J. Roy. Meteor. Soc.*, **119**, 1-16.
- Simpson, J.E., 1995: *Sea-Breeze and Local Winds*, Cambridge University Press, Cambridge, 234 pp.
- Singh, R.B., A.H. Huber and J.N. Braddock, 2001: Development of a Microscale Emission Factor Model for Particulate Matter (MicroFacPM) for Predicting Real-Time Motor Vehicle Emissions. *J. Air Waste Man. Ass.*, Draft

- Stull, R.B., 1988: *An Introduction to Boundary Layer Meteorology*, Kluwer Academic Publishers, The Netherlands, 670pp.
- Stunder, M. and S. SethuRaman, 1985: A comparative evaluation of the coastal internal boundary layer height equations. *Bound.-Layer Meteor.*, **32**, 177-204.
- Sun, W.Y., and C.Z. Chang, 1986: Diffusion model for a convective layer. Part I: Numerical simulation of convective boundary layer. *J. Climate Appl. Meteor.* **25**, 1445-1453.
- Weil, J.C., 1985: Updating applied diffusion models. *J. Clim. Appl. Meteor.*, **24**, 1111-1130.
- Xue, M., 1995: *Advanced Regional Prediction System (ARPS) Users Guide, Version 4.0*, Center for Analysis and Prediction of Storms, pp. 380.
- Xue, M., Q. Xu and K. Droegemeier, 1998: A theoretical and numerical study of density currents in nonconstant shear flows. *J Atmos Sci*, **54**, 1998-2019.
- Xue, M., K.K. Droegemeier and V. Wong, 2000: The advanced regional prediction system (ARPS)- A multi-scale nonhydrostatic atmospheric simulation and prediction tool. Part I: Model dynamics and verification. *Meteor. Atmos. Phy.*, **75**, 161-193.
- Xue, M., K.K. Droegemeier, V. Wong, A. Shapiro, K. Brewster, F. Carr, D. Weber, Y. Liu and D. Wang, 2001: The advanced regional prediction system (ARPS) - A multi-scale nonhydrostatic atmospheric simulation and prediction tool. Part II: Model physics and applications. *Meteor. Atmos. Phy.*, **76**, 143-165.